

THÈSE

Pour obtenir le grade de

DOCTEUR DE L'UNIVERSITÉ GRENOBLE ALPES

Spécialité : **Informatique**

Arrêtée ministériel : 25 mai 2016

Présentée par

David PAGNON

Thèse dirigée par **Lionel REVERET**
et codirigée par **Mathieu DOMALAIN**

préparée au sein du **Laboratoire Jean Kuntzmann**
dans **l'École Doctorale l'École Doctorale Mathématiques, Sciences et**
technologies de l'Information, Informatique

"Design, evaluation, and application of a workflow for biomechanically consistent markerless kinematics in sports"

"Conception, évaluation, et application d'une méthode biomécaniquement cohérente de cinématique sans marqueurs en sport"

Thèse soutenue publiquement le "**Date de soutenance**",
devant le jury composé de :

Président

Laboratoire, Président

Rapporteur

Laboratoire, Rapporteur

Examinateur

Laboratoire, Examinateur

Lionel REVERET

INRIA Grenoble, Directeur de thèse

Mathieu DOMALAIN

Institut Pprime, Co-Encadrant de thèse

Invité

Laboratoire, Invité



"To all of you who care about more important stuff than what follows."

Acknowledgements

*S*hould I start this by declaring that these PhD years have been alternatively depressing and engaging, exhausting and stimulating, infuriating and enthralling? This is trite, and true for everyone, PhD student or not. Covid pandemic or not. Child birth or not. Struggles in close friends' and relatives' lives or not. But there it is. Now that it is stated, let me go straight to my acknowledgements.

Above anyone else, I want to thank my mother. She not only had to deal with the difficult task of raising me and putting up with my constant flow of questions, but also with welcoming the four smaller sisters that came after me. As a widow. With debts to pay off, and very little money coming in. Moving every two years, until we settled in for a small apartment in a neighborhood that some would call a ghetto, although we preferred calling it home. And yet, there was always food on the table. Even better, we had no idea how poor we were, because she literally sacrificed her life for ours, and her passions for our interests. This is quintessential Christlike love. We all had the incredible opportunity of doing at least one physical, and one artistic activity, on top of pursuing university level studies. We also learned how to live happily with very little, which I'm starting to realize is a sort of superpower. Most importantly, she made children that all love each other. Now that I'm a father too, I can measure how high she set the bar, and I can only hope to be half as good as her. I can't award her the Legion of Honor she deserves, but at least here is a little bit of recognition! Thank you from all of us, maman.

I also have a deep thought for my father, who tragically passed away when I was still a little child. He did have to struggle with some issues that would eventually cause his death, but I believe he fought until the very end. He is actually the one who taught me a nice lesson of persistence, surely without even trying. A friend and I were racing up a hill, while my father timed us. I lost. We raced again, I lost again. I tried more, and sure enough, I lost every single race. I went to my dad and complained: "I'm tired papa, can we stop?" "Are you tired, really? Very good, it means that you're on your way to make progress!" I paused, and let it sink in for a few moments. And without a word, I went back running. That's how I learned that getting better goes with accepting to suffer a little. Later on, I also realized that out of any bad experience, be it death, you can take away something positive, something that will help you grow. Against all odds, I even made a first professional carrier in sports. I am very grateful for both my parents: I am who I am, with all my quirks and all that's to be loved or to be hated, thanks to them.

So many more people to thank! I'm just getting started, sorry to inflict you this. But let's start with the sisters. Esther comes just after me, she married an awesome guy from Congo, and is currently raising two wonderful little girls. She is the closest to what my mom was with us (and still is), making anyone feel home at any time, always on the move, taking care of her family during the day and working at nights, juggling countless tasks and thinking it is all just natural. Then comes Déborah, although she didn't come alone since Joëlla followed 10 minutes later. But believe it or not, she is slightly more than a twin. She has a high sense of justice and a desire to be helpful, which made her switch from the arts history field to the mentally challenging health one, so as to be more true to herself. Joëlla also is incredible. She fights every day her own health issues, could not finish high school but still managed to get a bachelor degree a few years later, and she now is a professional violinist, whose empathy perspires through all her plays. I'm on a roll now, and I don't think you'll be surprised if I tell you that my last sister, Noémie, is decent enough. She also became a professional violinist, she runs every day, and she is currently studying psychology. She also spends a lot of energy mediating arguments between people she loves. A family I'm proud of, not only because of their obvious skills, but because of their virtues.

I want to thank my grandparents, whose house was the ground base for all of my aunts, uncles, and cousins, who met there during each and every vacation. They made us discover the delightful joy of being cold, wet and exhausted during rainy hikes, to finally end up above a splendid sea of

cloud from which protruded just a few sharp peaks, over which Alpine choughs maneuvered with their vigorous flight. They are the true pillars of our extended family. The cycle of life being what it is, they became older and can't hike anymore. I am now very happy to see the whole family striving to take care of them, as much as we have been taken care of. I can sadly not name every single other member of my family, humans or animals, but they are all a crucial part of myself.

I do need to spend some time for the love of my life, Mikaela. We met in Lebanon, she is American, she cares about France as little as I care about the USA, and yet she accepted to come here for me, in the armpit of the stinky old world. She had the courage to take over my mother's difficult job to bear with my incessant questions. She actually has a lot of answers, since the extent of her knowledge is so wide and well-rounded. Mikaela is also an awesome writer who regularly wins writing contests, and a qualified editor who plays a large role in making my productions publishable. She is much more than she believes of herself: exceedingly faithful, remarkably generous, paradoxically very introverted but willing to home all the persons in need we come across, and unfortunately suffering from how little her power is to make the world a better place. She also comes with a very nice family in law, and of course, she is the mother of my child Cédric! A stunning baby who spends an excessive amount of energy smiling at every one, all day long (aside from sometimes, when he screams his head off.) He might give me a hard time whenever I get started writing my thesis, but he does it in a very cute way. And he always embodies a very good way for us to get away with our shared legendary absent-mindedness. I'm looking forward to the time I'll be old enough for him to change my own diapers.

Life wouldn't be life without friends, old and new ones, whether I see them several times a week or once every two or three blue moons. Friends of the family, friends from church, friends from parkour, friends from the performing world, friends I have no idea how I got to know them. Not to brag, but they are too numerous to name them all.

Finally, let's remember that this is a PhD thesis that I'm writing, and that there is no thesis without a lab, without supervisors, without fellow PhD students, post-docs, interns, researchers, administrative workers, cleaning operatives, and all who are involved in making work enjoyable (sic.) I want to thank them all. Lionel, my director, who saved me from the happy hell of starving performing arts to give me the chance to throw myself in another highly precariously fun situation. The subject of my thesis could not be better suited to my aspirations: both tightly related to sports, and highly technical. Mathieu, my co-supervisor, who always made himself available, ready to give me quick and valuable feedback, despite he lived in the other end of the country. One expert in computer vision, the other in biomechanics: the perfect fit for the objectives of my doctorate. Thibault, my faithful and multitasker office colleague, that I often left alone with the sole presence of cold-blooded computer hardware while I worked remotely. Other colleagues from other places such as the INSEP, the LBMC, the Pprime institute, etc. Thank you all!

To sum it up, I owe this work to my family, my friends, my colleagues, and I'm gullible enough to believe I owe it to God above all. I am happy I have overcome it, not only alone but with all the forenamed people!

On these words, I suppose I can now start with what I'm here for.

Abstract

*A*bstract.

Titre, Abstract, Mots clés

Potentiellement une seule section pour Abstract / Résumé, potentiellement en 2 colonnes (cf template Rennes)

Résumé

Résumé.

Contents

Acknowledgements	i
Abstract	iv
Résumé (en français)	v
Table of contents	vii
General introduction	1
1 State of the art	3
1.1 Overall context of kinematics in sports	4
1.1.1 General context	4
1.1.2 Marker-based systems	4
1.1.3 IMU and RGB-D systems	5
1.1.4 Markerless systems	6
1.2 2D markerless analysis	7
1.2.1 2D pose estimation	7
1.2.2 2D kinematics from 2D pose estimation	8
1.3 3D markerless analysis	8
1.3.1 3D pose estimation	8
1.3.2 3D kinematics from 3D pose estimation	10
1.4 Statement of need	11
2 Theoretical framework	14
2.1 2D pose detection	15
2.1.1 Why machine learning?	15
2.1.2 Machine learning timeline and principles	16
2.1.3 Machine learning for 2D pose detection	21
2.2 3D reconstruction	24
2.2.1 Pinhole camera model	24
2.2.2 Calibration	24
2.2.3 Triangulation	24
2.3 3D joint kinematics	24
2.3.1 Physically consistent model	24
2.3.2 Scaling	24
2.3.3 Inverse kinematics	24
3 Proposed solution: Pose2Sim Python package	27
3.1 Introduction to the workflow	29
3.2 Installation and demonstration	30
3.2.1 Installation	30
3.2.2 Demonstration Part-1: Build 3D TRC file on Python	31
3.2.3 Demonstration Part-2: Obtain 3D joint angles with OpenSim	33

Table of contents

3.3	Method details	34
3.3.1	Project	34
3.3.2	2D keypoint detection	34
3.3.3	Camera calibration	35
3.3.4	Tracking the person of interest	36
3.3.5	Triangulating	36
3.3.6	Filtering and other operations	37
3.3.7	OpenSim scaling and inverse kinematics	37
3.4	Limitations and perspectives	39
3.4.1	Issues related to OpenPose	39
3.4.2	Multi-person analysis	40
3.4.3	User-friendly calibration	41
3.4.4	Visualization tools	41
3.4.5	Real-time analysis	43
3.4.6	Other perspectives	43
4	Robustness assessment	45
4.1	Introduction	47
4.1.1	Robustness definition	47
4.1.2	Assessing robustness	48
4.2	Methods	48
4.2.1	Experimental setup	48
4.2.2	Participant and protocol	50
4.2.3	Challenging robustness	51
4.2.4	Markerless kinematics	51
4.2.5	Statistical analysis	53
4.3	Results	54
4.3.1	Data collection and 2D pose estimation	54
4.3.2	Pose2Sim tracking, triangulation, and filtering	54
4.3.3	OpenSim scaling and inverse kinematics	55
4.3.4	Relevance, repeatability and robustness of angles Results	56
4.4	Discussion	60
4.4.1	Pose2Sim	60
4.4.2	Relevance, repeatability and robustness	61
4.4.3	Limits and perspectives	62
5	Accuracy assessment	65
5.1	Introduction	67
5.2	Methods	68
5.2.1	Data collection	68
5.2.2	Markerless analysis	68
5.2.3	Marker-based analysis	69
5.2.4	Statistical analysis	69
5.3	Results	70
5.3.1	Concurrent validation	70
5.3.2	Comparison with other systems	74
5.4	Discussion	74
5.4.1	Strengths of Pose2Sim and of markerless kinematic	74
5.4.2	Limits and perspectives	74
5.5	Conclusions	75

6 Application to boxing, using action cameras	77
6.1 Objectives	78
6.1.1 Key Performance Indicators in boxing	78
6.1.2 Limits of research-grade systems in competitions	78
6.1.3 Objectives	78
6.2 Methods	79
6.2.1 4 conditions	79
6.2.2 Pose-calibration on ring dimensions	79
6.2.3 Post-synchronization on 2D movement speeds	79
6.2.4 GoPro spatio-temporal base into Qualysis'	79
6.2.5 Statistical analysis	79
6.3 Results	80
6.4 Discussion	80
6.4.1 Equipment and protocol vs. pose estimation model	80
6.4.2 Pros and cons of different systems	80
7 Application to BMX racing, jointly capturing pilot and bike	82
7.1 Introduction	83
7.1.1 The start in BMX racing	83
7.2 Methods	83
7.2.1 Material and protocol	83
7.2.2 Pilot inverse kinematics	83
7.2.3 Bike inverse kinematics	83
7.2.4 Joined pilot and bike inverse kinematics	83
7.3 Results	84
7.4 Discussion	84
7.4.1 On these data	84
7.4.2 Limits and perspectives	84
General conclusion	86
Bibliography	I
List of figures	XIX
List of tables	XXIV
A Appendix A on Robustness assessment	XXVII
A.1 Robustness: Running task results	XXVIII
A.2 Robustness: Cycling task results	XXIX
B Appendix B on Accuracy assessment	XXX
B.1 Lower-body results for the running and cycling tasks	XXXI
B.1.1 Accuracy: Running task results	XXXI
B.1.2 Accuracy: Cycling task results	XXXIII
B.2 Sacro-lumbar and upper-body results for all tasks	XXXV
B.2.1 Accuracy: Upper-body results for the walking task	XXXVI
B.2.2 Accuracy: Upper-body results for the running task	XXXVIII
B.2.3 Accuracy: Upper-body results for the cycling task	XL

C Appendix C : Protocole	XLII
C.1 Section 1	XLIII
C.1.1 Sous section 1	XLIII
C.1.2 Sous section 2	XLIII

General introduction

*G*eneral introduction.

Intérêt markerless dans le sport

Problèmes de détection de features dans image, calibration et triangulation, scaling et cinématique inverse, et où mon travail s'inscrit (bridge between 2D feature detection in computer vision, and physically consistent 3D biomechanics for sports)

Présentation détaillée de chaque chapitre

Schéma résumé: acquisition, calibration, pose estimation, triangulation&filtrage, scaling, inverse kinematics + applications

Insérer graphical abstracts (pour Pose2Sim, Robustness, Accuracy). Autre pour state of the arts, theoretical framework, et pour Boxe et BMX ?

Liste des articles publiés

CNRS, LJK, Pprime, FFC (start with simple)

Motivation, Objectives, Contributions, Content

1

State of the art

Motion capture (MoCap) in sports is traditionally performed with marker-based (opto-electronic) systems. However, this presents some drawbacks. As a consequence, alternatives are being investigated, among which those offered by Inertial Measurement Units (IMUs) or depth-field (RGB-D) cameras. Markerless analysis from videos sources represents one of the most promising prospects, which has been possible thanks to progress in machine learning. From 2D pose estimation to 3D joint angle determination, this is a new field which opens up new possibilities for motion analysis in a sports context.

This chapter is an up-to-date and more detailed version of the introduction of the previously published paper: "Pose2Sim: An End-to-End Workflow for 3D Markerless Sports Kinematics—Part 1: Robustness" [Pagnon2021].

Contents

1.1	Overall context of kinematics in sports	4
1.1.1	General context	4
1.1.2	Marker-based systems	4
1.1.3	IMU and RGB-D systems	5
1.1.4	Markerless systems	6
1.2	2D markerless analysis	7
1.2.1	2D pose estimation	7
1.2.2	2D kinematics from 2D pose estimation	8
1.3	3D markerless analysis	8
1.3.1	3D pose estimation	8
1.3.2	3D kinematics from 3D pose estimation	10
1.4	Statement of need	11

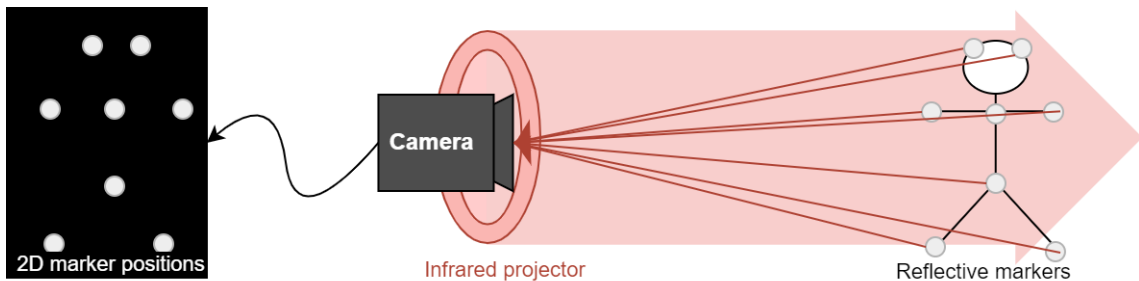
1.1 Overall context of kinematics in sports

1.1.1 General context

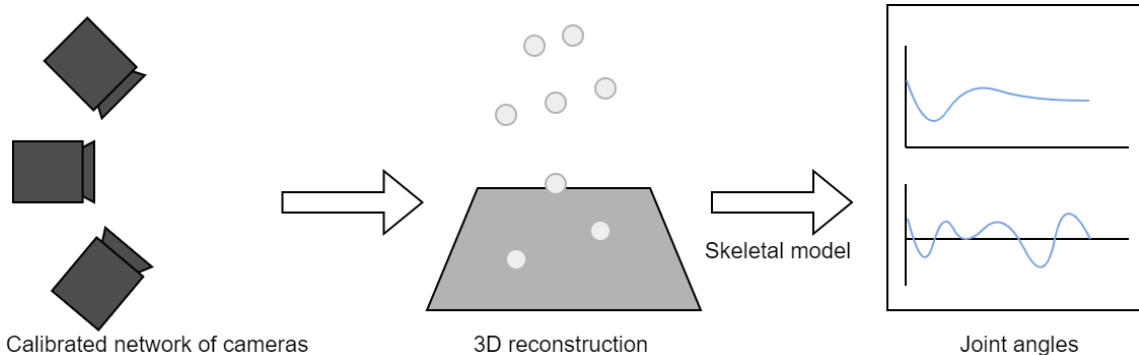
As coaching athletes implies observing and understanding their movements, motion capture (MoCap) is essential in sports. It helps improving movement efficiency, preventing injuries, or predicting performances. For the last few decades, marker-based systems have been considered the best choice for the analysis of human movement, when regarding the trade-off between ease of use and accuracy. However, these methods have proven to be much more challenging in a sports context than in a laboratory setting, and to be generally inappropriate [Mündermann2006, Colyer2018]. As a consequence, other methods have been investigated (see Table 1.1).

1.1.2 Marker-based systems

Marker-based systems use a network of opto-electronic cameras. Each of these cameras are surrounded by a crown of infrared LEDs, which projects light toward the subject, who is equipped with reflective markers. Ideally, only the light reflected from these markers is captured by the cameras. The camera usually pre-processes the image to make it binary, and only outputs the coordinates of the detected marker (Figure 1.1a).



(a) An opto-electronic camera is traditionally surrounded by a crown of infrared LEDs, projecting light toward the subject. The subject wears markers, which reflect light back to the camera. Marker positions are then known in the camera plane.



(b) Once calibrated, a network of these cameras allows for 3D reconstruction of marker positions. Marker coordinates are then used to infer the posture of the subject.

Figure 1.1: Principles of marker-based motion capture. (Figure 1.1a) presents the functioning of an opto-electronic camera. (Figure 1.1b) shows how a network of calibrated motion capture cameras helps obtaining joint angles.

If calibrated, using a network of these cameras allows for triangulating the 2D coordinates. Calibration involves knowing the cameras' intrinsic properties (such as focal length, optical center, distortion) as well as their extrinsic properties (their position and orientation as regards to the global coordinate system.) See Chapter 2.2 on [3D reconstruction](#) for more details. The reconstructed 3D marker positions are then used to optimize the posture of a physically consistent

skeleton, scaled to each individual subject. In particular, this allows for obtaining 3D joint angles at each point in time, commonly referred to as inverse kinematics (IK.)

Yet, reflective marker-based camera systems are complex to set up, are time-consuming, and are very expensive. They also require specific lightning conditions, and involve cumbersome cabling. Moreover, markers may fall off the body of the participant due to sharp accelerations or sweat. They can hinder the natural movement of athletes, which is likely to affect their warm-up, focus, and safety. While the accuracy of landmark location is claimed to be sub-millimetric in marker-based methods [Topley2020], marker placement is tedious, intrusive, prone to positioning variability from the operator [Tsushima2003], and subject to skin movement artifacts, especially on soft tissues. Della Croce et al. found out that inter-operator variations in marker placements range from 13 to 25 mm, which can propagate up to 10° in joint angle prediction [Gorton2009, della Croce1999]. For example, tissue artifacts account for up to a 2.5 cm marker displacement at the thigh, which can cause as much as a 3° error in knee joint angles tissues [Benoit2015, Cappozzo1995]. Joint positions must be calculated explicitly in marker-based methods, which introduces more variability: these errors range up to 5 cm, which can contribute up to 3° of error in lower limb joint angles [Leboeuf2019]. Nevertheless, since marker-based methods benefit from decades of research, they are still considered as the reference method for motion capture.

1.1.3 IMU and RGB-D systems

Consequently, other approaches based on alternative technologies have been investigated over the past years. For instance, wearable Inertial Measurement Units (IMUs) can be placed on an athlete's limbs. IMUs are generally made of an accelerometer, a gyroscope, and a magnetometer. The accelerometer measures the linear acceleration, the gyroscope measures the rotational speed, and the magnetometer measures the orientation of the earth magnetic field. Fusing and integrating these signals allows for the determination of their 3D orientations. The orientation of the athlete's limbs can then be used in combination with a skeletal model to infer their posture (Figure 1.2).

IMUs offer the advantages of getting away from all camera-related issues. They are inexpensive, they do not involve any complex setup and calibration, the field of view is larger, data do not take much storage space, they are not sensitive to self- and gear-occlusions, they can be operated outside of a controlled environment, and they can work in real-time [Johnston2019, Chambers2015]. They still have the drawback of requiring an external equipment to wear, involving high technical skills from the operator, and are sensitive to ferromagnetic disturbances. Above all, they are exposed to drift over time and need to be calibrated every few minutes. Joint angle accuracy is relatively good in the flexion/extension plane, but less so in other rotational planes where errors are greater than 5° for most motions [Zhang2013, Rekant2022]. Moreover, they are not suitable for joint positions assessment, since these are obtained through multiple integrations of the original signal [Ahmad2013].

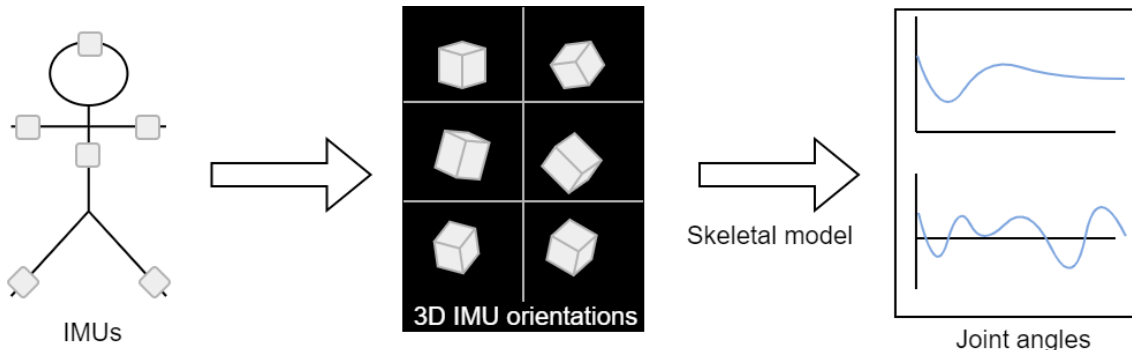


Figure 1.2: IMUs are placed on the subject's limbs. The orientation of the limbs is then used to infer the posture of the subject.

Another approach involves depth-field cameras (RGB-D). Older models projected infrared *structured* light (i.e., a pattern) onto the scene. The relative deformation of the pattern reflected from the scene was then used to estimate depth. Newer models project infrared *modulated* light onto the scene. The time of flight of the light reflected from the scene is then used to estimate depth. Results are commonly considered to be 2.5D, since only the depth of the front facing plane of view is measured. Gait analysis results are natively poor, but after an optimization by a neural network, [Guo2022] manage to get root-mean-square errors under 7° for knee flexion/extension angle at the most challenging part of the gait cycle, although 3D joint angle errors usually stay under 2-3°. However, it may not perform as well on other motions on which the neural network has not been trained. A network of a few RGB-D cameras can give access to full 3D [Carraro2017, Choppin2013, Colombel2020]. Nevertheless, these cameras hardly function in direct sunlight nor at a distance over 5 meters, and they work at lower frame rates (generally under 30 Hz) [Han2013, Pagliari2015].

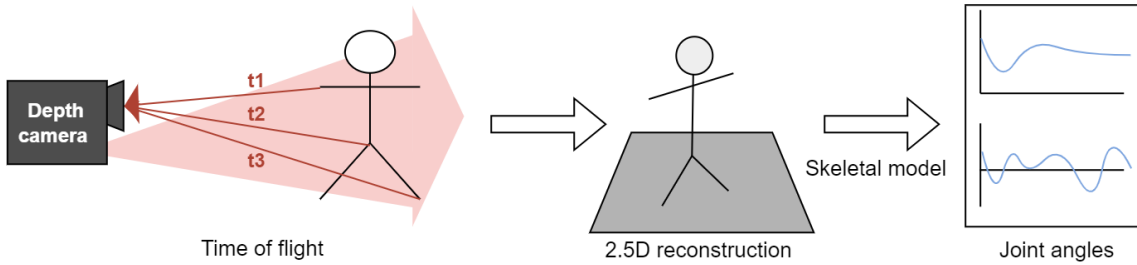


Figure 1.3: A depth-field camera (RGB-D) projects infrared modulated light onto the subject’s body. The time it takes for the light to be reflected to the camera sensor (time of flight) depends on distance, and gives access to the depth of the scene. Older RGB-D cameras use structured light rather than time of flight calculations to infer depth.

1.1.4 Markerless systems

A recent breakthrough has come from computer vision, and the advent of 2D pose estimation from image sources, which quickly became more efficient and accurate. The explosion of deep-learning based methods from camera videos, for which the research has skyrocketed around 2016 [Wang2021b], is related to the increase in storage capacities and huge improvements in GPU computing. A search on the ScienceDirect database for “deep learning 3D human pose estimation” produced fewer than 100 papers per year until 2015, and the number is now reaching over 1,000, fitting an exponential curve (Figure 1.4).

It has rekindled interest from the biomechanics community towards image-based motion analysis, which is where it all started with the invention of chronophotography in the 19th century by Marey in France, and Muybridge in the USA [Baker2007]. Currently, two approaches co-exist in human and animal motion analysis: the first one mostly focuses on joint positions, and is lead by the computer vision and the deep-learning communities; while the second one is interested in joint angles, such as the biomechanics community uses to obtain physically coherent kinematics individualized to each subject. One of the main current challenges is to bridge the gap between these two worlds, and to take advantage of deep-learning technologies for kinematic analysis [Cronin2021, Seethapathi2019].

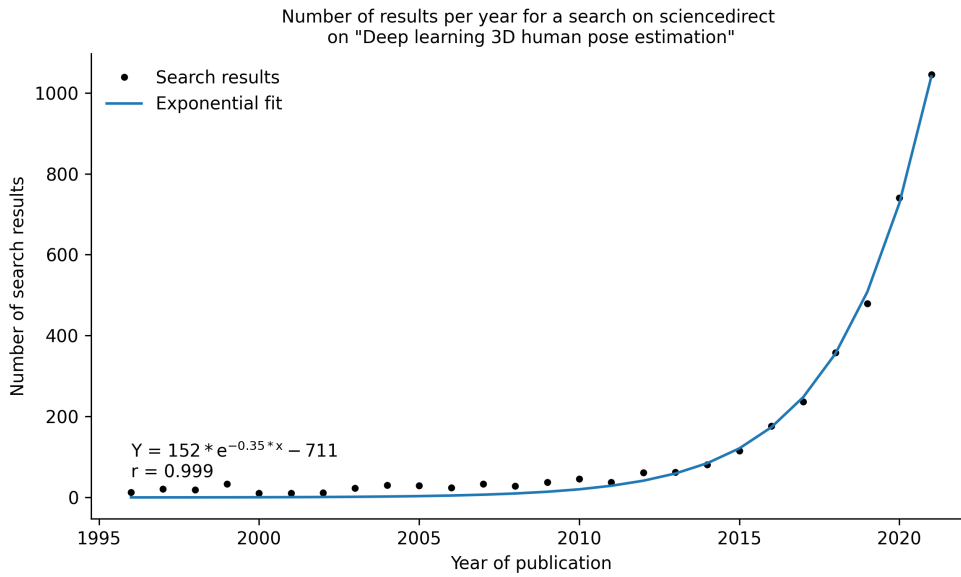


Figure 1.4: The search for “deep learning 3D human pose estimation” (dots) fits an exponential curve (line). The search produced less than 100 results until 2015, and is now well over a 1,000 per year.

1.2 2D markerless analysis

1.2.1 2D pose estimation

The most well-known off-the-shelf 2D human pose estimation solutions are OpenPose [Cao2019] (Figure 1.5), and to a lesser extent AlphaPose [Fang2017]. While both show similar accuracy, AlphaPose is faster when few people are in the scene. However, OpenPose has the advantage of being a bottom-up approach, whose computational cost does not increase with the number of persons detected [Cao2019]. It is also more widespread (25,000 stars on the GitHub repository, vs. 6,000 for AlphaPose). A bottom-up approach first detects all available joint keypoints, and then associates them to the right persons; while a top-bottom approach first detects bounding boxes around each person, and then finds joint keypoints inside of them. OpenPose is the only multi-person 2D pose estimation solution that provides foot keypoints, which are essential for sports motion analysis.

Other approaches have shown even better results on evaluation datasets (see review [Chen2020]), but they are generally slower and not as widespread. The technology, however, is still maturing and some light-weight systems such as BlazePose [Bazarevsky2020], UULPN [Wang2022b], or YOLOv7 [Wang2022a] are being proposed, which can operate in real time on a mobile phone; however, they either support single-person detection only, are not accurate enough for quantitative motion analysis [Mroz2021], or haven’t been embraced by the community yet. Some work has also been done on temporal consistency across frames with OpenPifPaf, which makes the system much faster, and helps it perform better on low-resolution regime or with occlusions such as in crowds [Kreiss2022].

Two other 2D pose estimation toolboxes are DeepLabCut [Mathis2018,Lauer2022] and SLEAP [Pereira2022], which were initially intended for markerless animal pose estimation. They have the advantage that they can be custom trained for the detection of any human or not human keypoint with a relatively small dataset.

All the tools presented in this section are open-source. See Chapter 2.1.3 on [Machine learning for 2D pose detection](#) for more technical details on their architecture.



Figure 1.5: 2D pose estimation by OpenPose. Image courtesy of [Cao2019].

1.2.2 2D kinematics from 2D pose estimation

Some authors bridge 2D pose estimation to more biomechanically inspired variables, such as in gait kinematics analysis. Kidzinski et al. present a toolbox for quantifying gait pathology that runs in a Google Colab [Kidziński2020]. Stenum et al. evaluate gait kinematics calculated from OpenPose input concurrently with a marker-based method. Mean absolute error of hip, knee and ankle sagittal angles were 4.0° , 5.6° and 7.4° [Stenum2021]. Liao et al. have not released their code, but they use OpenPose outputs to train a model invariant to view [Liao2020]. Viswakumar et al. perform direct calculation of the knee angle from an average phone camera processed by OpenPose [Viswakumar2019]. They show that OpenPose is robust to challenging clothing such as large Indian pants, as well as to extreme lightning conditions. Other sports activities have been investigated, such as lower body kinematics of vertical jump [Drazan2021] or underwater running [Cronin2019]. Both works train their own model with DeepLabCut. Serrancoli et al. fuse OpenPose and force sensors to retrieve joint dynamics in a pedaling task [Serrancolí2020]. Although it doesn't specifically use deep-learning approaches, another noteworthy tool for 2D sports movement analysis is Kinovea [Fernández-González2020]. It allows to manually label keypoints on a frame, and track them in time in order to obtain point trajectories or angle data.

1.3 3D markerless analysis

1.3.1 3D pose estimation

There are a lot of different approaches for markerless 3D human pose estimation, and listing them all is beyond our scope (see review [Wang2021b]). Some more ancient ones are not based on deep-learning and require specific lightning and background conditions, such as visual-hull reconstruction [Ceseracciu2014]. Some directly lift 3D from a single 2D camera (see review [Liu2022c]), with different purposes: one estimates the positions of a set of keypoints around the joint instead of determining only the joint center keypoint, so that axial rotation along the limb is solved [Fisch2020]; SMPL and its sequels retrieve not only joint positions and orientations, but also body shape parameters [Loper2015]; while XNect primarily focuses on real time [Mehta2020]. A few approaches even strive to estimate 3D dynamics and contact forces from a 2D video input [Li2019, Rempe2021, Louis2022]. Some incorporate kinematic priors into their neural networks in order to take advantage of human knowledge [Xu2020b]. Surprisingly, this does not seem to be done in multi-view approaches. Rempe et al. solve occlusions from a 2D input [Rempe2020], but this remains a probabilistic guess that may be unsuccessful in case of

unconventional positions of hidden limbs, whereas using more cameras would have given more trustworthy results.

Some research attempts to solve 3D pose estimation from a network of uncalibrated cameras, i.e., cameras whose extrinsic parameters (translation and rotation with respect to the coordinate system), intrinsic parameters (focal length, pixel size, etc.), and distortion coefficients are not known (See Chapter 2.2 on [3D reconstruction](#) for more details.) It either uses 2D pose estimations of each view as visual cues to calibrate on [[Takahashi2018](#), [Xu2021](#), [Liu2022a](#)], or an adversarial network that predicts views of other cameras, compares them to real views, and adjusts its calibration accordingly [[Ershadi-Nasab2021](#)]. Dong et al. recover 3D human motion from unsynchronized and uncalibrated videos of a repeatable movement found on internet videos (such as a tennis serve performed by a celebrity) [[Dong2020](#)]. Using uncalibrated videos is still a very experimental trend, that would require more research before being used in biomechanics.

We choose to focus on the methods that estimate 3D pose by triangulating 2D pose estimations from a network of multiple calibrated cameras. The classical evaluation metric is the MPJPE (Mean Per Joint Position Error), which is the average Euclidian distance between the estimated joint coordinate and its ground truth. Most methods take OpenPose as an input for triangulation, and more specifically the body_25 model. Labuguen et al. evaluate 3D joint positions of a pop dancer with a simple Direct Linear Transform triangulation (DLT [[Hartley1997](#), [Miller1980](#)]) from 4 cameras [[Labuguen2020](#)]. Apart from the upper body for which error goes up to almost 700 mm, the average joint position error is about 100 mm. Nakano et al. examine three motor tasks (walking, countermovement jumping, and ball throwing), captured with 5 cameras and triangulated with the same methods, with a subsequent Butterworth filter [[Nakano2019](#)]. 47% of the errors are under 20 mm, 80% under 30 mm, and 10% are above 40 mm. The largest errors are mostly caused by OpenPose wrongly tracking a joint, for example by swapping the left and the right limb, that causes large errors up to 700 mm. This may be fixed either by using a better 2D pose estimator, or by using more cameras to reduce the impact of an error on a camera, or else by considering the temporal continuity in movement. Needham et al. use 9 cameras and find that ankle MPJPEs are within the margin of error of marker-based technologies (1–15 mm), whereas knee and hip MPJPEs are greater (30–50 mm). These errors are systematic and likely due to "ground-truth" images being mislabeled in the training dataset [[Needham2021b](#)]. They also run the comparison with AlphaPose and with DeepLabCut. While AlphPose's results are similar to OpenPose's; DeepLabCut errors are substantially higher.

Slembrouck at al. go a step further and tackle the issue of limb swapping and of multiple person detection [[Slembrouck2020](#)]. In case of multiple person detection, one needs to make sure they associate the person detected on one camera to the same person detected on other ones. Slembrouck et al. manage to associate persons across cameras by examining all the available triangulations for the neck and mid-hip joints: the persons are the same when the distance between the triangulated point and the line defined by the detected 2D point and the camera center is below a certain threshold. They only focus on lower limb. Their first trial features a person running while being filmed by seven cameras, whereas their second one involves a person doing stationary movements such as squats while filmed by 3 cameras. After filtering, the average positional error in the first case is about 40 mm, and it is roughly 30 mm in the second case (less than 20 mm for the ankle joint). Other authors deal with the multiperson issue in a slightly different way [[Bridgeman2019](#), [Chu2021](#), [Dong2019](#)]. In average, if the detected persons are correctly associated and the limbs don't swap, the average joint position error for an OpenPose triangulation is mostly below 40 mm.

Some triangulation methods not based on OpenPose reach even better results on benchmarks, although it comes at the cost of either requiring heavy computations, or of being out of reach for non-expert in deep-learning and computer vision. The classic approach reduces the joint detection heatmap to its maximum probability, and then to triangulate these scalar 2D positions. Instead of this, the main state-of-the art methods directly perform a volumetric triangulation of the whole

heatmaps, and only then take the maximum probability as a 3D joint center estimate. By working this way, they keep all the information available for as long as possible. They manage to lower their MPJPE to about 20 mm [He2020, Iskakov2019].

1.3.2 3D kinematics from 3D pose estimation

Numerous studies have focused on the accuracy of 3D joint center estimation, but far fewer have examined joint angles [Zheng2022]. Yet, when it comes to the biomechanical analysis of human motion, it is often more useful to obtain joint angles. Joint angles allow for better comparison among trials and individuals, and they represent the first step for other analysis such as inverse dynamics. This issue is starting to be tackled. Zago et al. evaluate gait parameters computed by triangulating 2 videos processed by OpenPose, and notice that straight gait direction, longer distance from subject to camera, and higher resolution make a big difference in accuracy [Zago2020]. D’Antonio et al. perform a simple triangulation of the OpenPose output of two cameras, and compute direct flexion-extension angles for the lower limb [D’Antonio2021]. They compare their results to IMU ones, and point out that errors are higher for running than for walking, and are also rather inconsistent: Range of Motion (ROM) errors can reach up to 14° , although they can get down to 2 to 7° if the two cameras are set laterally rather than in the back of the subject. Wade et al. calculate planar hip and knee angles with OpenPose, AlphaPose, and DeepLabCut with the input of 9 cameras [Wade2021]. They deem the method accurate enough for assessing step length and velocity, but not for joint angle analysis. AniPose, a Python open-source framework, broadens the perspective to the kinematics of any human or animal with a DeepLabCut input, instead of OpenPose. They offer custom temporal filters, as well as spatial constraints on limb lengths [Karashchuk2021]. To our knowledge, it has only been concurrently validated for index finger angles in the sagittal plane, resulting in a root-mean-square error of 7.5° [Geelen2021].

The previous studies calculated simple planar angles between 3 joint centers. However, the human skeleton is complex and not only made of pin joints: aside from the flexion/extension rotation axis, the abduction/adduction axis and the internal/external axis are typically also engaged; and some joints also involves some translation, such as the shoulder. In this case, either several markers per joints or a solid skeletal model are needed. So far, little work has been done towards obtaining 3D angles from multiple views [Zheng2022]. Aside from our solution (see Chapter 3 on [Pose2Sim](#)), two main others are worth mentioning. Theia3D is a commercial software application for human gait markerless kinematics. It estimates the positions of a set of keypoints around the joint, and then uses a multi-body optimization approach to solve inverse kinematics [Kanko2021a, Kanko2021b]. They notice an offset in hip and ankle angles between their markerless system and the reference marker-based one, likely due to different skeletal models. Once this offset is removed, the root-mean-square error (RMSE) in lower limb roughly ranges between 2 and 8° for flexion/extension and abduction/adduction angles, and up to 11.6° for internal/external rotation. Although the GUI is user-friendly, it is neither open-source nor customizable. OpenCap [[Uhlrich2022](#)] has recently been released, and offers a user-friendly web application working with low-cost hardware. It predicts the coordinates of 43 anatomical markers from 20 triangulated keypoints, and imports them in OpenSim, which is an open-source biomechanical 3D analysis software using a multi-body optimization approach to solve inverse kinematics [Delp2007, Seth2018]. OpenCap then performs classic inverse kinematics with numerous inferred markers and a skeletal model. However, the source code has not yet been released.

Other approaches don’t focus so much on keypoint detections, and capture the whole shape of participants. [[Reveret2020](#)] records the 3D shape of a speed climber in a studio equipped with 68 video cameras, and then animates it to follow 2 calibrated drone views by optimizing its manifold parameters. This allows for tracking the center of mass and for detecting hand contacts with holds, without the use of machine learning. Simi shape, a commercial software, jointly learns 2D shape and 2D keypoint coordinates. It claims to be able to obtain accurate kinematics with few cameras,

thanks to the additional information shape detection provides (validation with their newer machine learning based process not yet published.) Pose estimation from videos can also be fused with the information provided by other sensors, such as IMUs [Bao2022, Zhang2020]. This enables solving occlusions in videos, and compensation of the drift consecutive to the integration of accelerations and rotation speeds in IMUs. For example, [Haralabidis2020] fuse OpenPose results from a single monocular video and two IMU outputs, and solve kinematics of the upper body in OpenSim in order to examine the effects of fatigue on boxing. Results are promising, but this cannot be considered as fully markerless. Fusing the depth map of a single RGB-D camera with its image processed by OpenPose has also been investigated [Liu2022b], although 3D coordinate errors were close to 10 cm.

1.4 Statement of need

According to Atha [Atha1984], an ideal motion analysis system involves the collection of accurate information, the elimination of interference with natural movement, and the minimization of capture and analysis times. Yet, even though a marker-based system gives relatively accurate results, it requires placing markers on the body which can hinder natural movement, it is hard to set up outdoors or in context, and it is strenuous to analyze. As a consequence, in the overwhelming majority of cases, coaches solely use subjective visual observation to assess an athlete's movement patterns and to compare performances. As a matter of fact, despite the advantages of technology, investing in it has its pitfalls: the information gathered can be unhelpful, or inaccurate, or not easily interpretable, or simply not implementable in the context of sports [Windt2020].

The emergence of markerless kinematics opens up new possibilities. Indeed, a network of RGB cameras does not assume any particular environment, and it does not hinder the athlete's movement and focus. However, it still requires delicate calibration, complex setup, large storage space, and high computational capacities. Gathering reliable and usable kinematic data in context is an ambitious challenge, but research has been accelerating in the last few years (Figure 1.4), as have better results.

The objective of this thesis is to participate in building a bridge between the communities of computer vision and biomechanics, by providing a simple and open-source pipeline connecting the two aforementioned state-of-the-art tools: OpenPose and OpenSim. Robustness and accuracy will be assessed, and concrete applications in elite sports context will be discussed.

Sensor type	Mono/Multi camera	2D/3D	Pros and Cons
Opto-electronic	Multi	3D	<ul style="list-style-type: none"> + Standard + Good ease-of-use/accuracy trade-off - Not suitable in sports contexts
IMU	N/A	3D	<ul style="list-style-type: none"> + Good angle accuracy - Angle drift & poor position analysis - Can be cumbersome
RGB-D	Mono	2.5D	<ul style="list-style-type: none"> + Markerless - Generally poor accuracy - Frame-rate ≤ 30 Hz - Needs distance ≤ 5 m and no direct sunlight
	Multi	3D	<ul style="list-style-type: none"> + Full 3D markerless + Better accuracy - Same as above re. frame-rate, distance, and light
	Mono	2D	<ul style="list-style-type: none"> + Very robust in all contexts + Cheap and easy to set up - Only 2D - Not very accurate
	Multi uncalibrated	3D	<ul style="list-style-type: none"> + Full 3D with one single RGB camera - Probabilistic guess when occlusions: accuracy \searrow - Slow
RGB video	Multi calibrated	3D	<ul style="list-style-type: none"> + Removes difficult step of calibration - Still experimental
	Multi calibrated with kin. constraints	3D	<ul style="list-style-type: none"> + Solves occlusions + Robust - Systematic offsets due to labelling errors - Calibration can be challenging
Sensor fusion with RGB video	N/A	3D	<ul style="list-style-type: none"> + Compensates offsets + Constrains limb lengths and joint angles - Still inaccurate pelvis angles • With IMUs: More accurate, but not markerless • With one RGB-D camera (Depth + OpenPose on RGB): still inaccurate

Table 1.1: Pros and cons in state-of-the-art approaches for human motion analysis. The multi-person prospect is not addressed, as it can be available with all approaches, but it is not always. IMU: Inertial Measurement Unit. N/A: Not Applicable. kin.: kinematic. RGB-D: red-green-blue-depth.

2

Theoretical framework

Obtaining 3D kinematics from a network of calibrated video cameras involves understanding a certain theoretical framework. First, keypoints must be recognized in images. This is mostly achieved with machine learning models. Then, all the 2D features detected for each cameras need to be reconstructed in the 3D space. Finally, these coordinates must be constrained to a biomechanically consistent model, in order to obtain coherent 3D joint kinematics.

Contents

2.1	2D pose detection	15
2.1.1	Why machine learning?	15
2.1.2	Machine learning timeline and principles	16
2.1.3	Machine learning for 2D pose detection	21
2.2	3D reconstruction	24
2.2.1	Pinhole camera model	24
2.2.2	Calibration	24
2.2.3	Triangulation	24
2.3	3D joint kinematics	24
2.3.1	Physically consistent model	24
2.3.2	Scaling	24
2.3.3	Inverse kinematics	24

2.1 2D pose detection

2.1.1 Why machine learning?

As a first step, achieving motion analysis from a network of cameras involves detecting features in images. These features can be whole human beings, joint centers, body landmarks, sports gear such as tennis balls, climbing holds, or much more.

Two broad approaches can be implemented: the first one consists in using dedicated algorithms for each task. The gist of it is to understand the task well enough to build an appropriate solution: this is a knowledge-driven approach. Among other techniques, corner and contour detection, color thresholding, affine transformation, template matching, watershed segmentation, can be used. For example, if one wants to differentiate two boxers wearing respectively a blue and a red shirt, they can filter them by color. If one needs to identify on which portion of a speed climbing wall an athlete is, they can match the template of each holds on the whole image. OpenCV [Bradski2000] provides convenient tools for this purpose, in C++ and Python languages. This approach is often fast, but also quite complicated to implement, and neither flexible nor robust. If there is other red or blue patches in the boxing scene, if the boxer wears green or if the light is poor, this will not work anymore. Likewise for holds, if the sun casts a large shadow which changes its apparent shape, or if holds are seen from a different perspective.

The second approach takes advantage of machine learning algorithms, which constitute an entirely different paradigm. The idea is to show the machine enough examples for it to "understand" by itself its underlying attributes, so that it manages to detect and label automatically new images: this is a data-driven approach. It can be used for both aforementioned tasks, in a much more flexible way: if one wants the system to recognize boxing gloves or holds in challenging conditions, they simply have to include such examples while training the model. The machine learning approach is also suitable for other tasks, such as whole-image classification (e.g., determining whether this is a boxing or a BMX scene), object detection (e.g., localization of a bike and of a person with a bounding box), background extraction [Bouwmans2019], semantic and instance segmentation (e.g., extracting the shape of the bike and of the person) [Minaee2021], or keypoint detection (e.g., localization of human joint centers and keypoints on a bike [Chen2020]) (Figure 2.1). By 2015, data-driven methods definitely took over knowledge-driven ones in vision analysis problems, and by extension in sports motion analysis from videos (Figure 1.4).

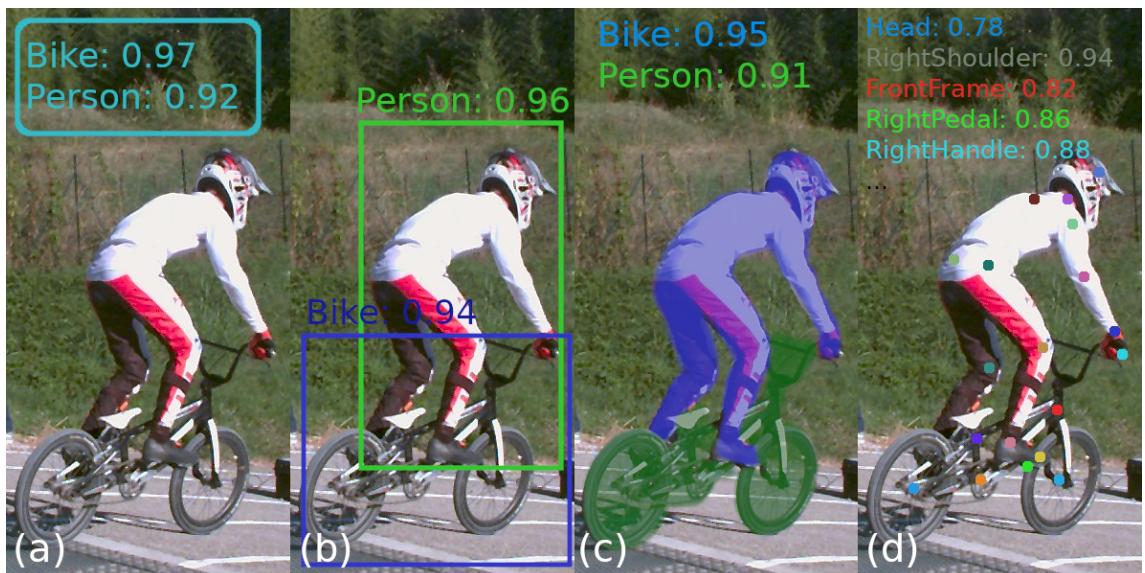


Figure 2.1: Different types of image analysis. (a) Whole image classification, (b) Object detection and localization, (c) Instance segmentation and shape extraction, (d) Keypoint detection.

2.1.2 Machine learning timeline and principles

Machine learning is a subset of artificial intelligence (AI.) As such, one can trace its origin back to the discovery of the natural neuron at the end of the 19th century, by Nobel Prize Ramón y Cajal [[López-Muñoz2006](#)], followed half a century later by the first model of an artificial neuron [[McCulloch1943](#)]. A natural neuron is a simple learning unit, which collects the nervous influx sent by other neurons to its dendrites, and sends an action potential when the total influx weighted and summed in the soma overcomes a threshold value. This potential is then transmitted through the axon to the next neuron as a new influx. Similarly, an artificial neuron receives output vectors from previous neurons, weighs and sums them with a summation function, and transfers the resulting output vector to the next neurons if it reaches a certain threshold determined by an activation function (Figure 2.2a-b).

The perceptron, invented in 1956 [[Rosenblatt1958](#)], represents the first practical application of an artificial neuron. It acts as a binary classifier which predicts class 1 if the neuron is fired, and class 0 otherwise. It automatically adjusts its weights by learning from previously labeled example data (see Algorithm 1 and Figure 2.2b). It could be used, for example, to predict whether an athlete is going to be "good" or not, given his force-velocity results on an ergometer test (see step-by-step [Example 1](#) and Figure 2.3), and given enough example data. Needing previously labeled data makes it a supervised classifier – we will not discuss unsupervised methods here. Of course, this example is oversimplified. Being good or not as a sport is a complex and multifactorial outcome, and two variables can't sum it up. However, the perceptron can take more than two variables as inputs (for example, force, velocity, and endurance), and it can also be generalized to multiclass classification with more than two outputs (for example, to differentiate between strong, explosive, and resistant type of athletes.)

Nevertheless, it often takes a lot of iterations over good quality training data for the perceptron to converge. Moreover, it does converge if and only if the data are linearly separable, i.e., if they can be separated with a straight line [[Novikoff1963](#)] (see Figure 2.4). Some fundamental problems such as the XOR gate can't be solved with a basic single layer Artificial Neural Network (ANN) [[Minsky1969](#)]. This constituted one of the early setbacks for AI. Then, the high computational cost of these approaches, combined with the complexity of common-sense problems, hampered the trust in learning methods. Indeed, vision and language problems require enormous amounts of data, and can't be solved with a simple dictionary (for example, "the spirit is willing but the flesh is weak" becomes "the vodka is good but the meat is rotten" when translated back and forth from English to Russian.) Overinflated promises and expectations, followed by disappointment in academia and industries, led to cuts in funding, and eventually loss of skills in the 1970s: this is referred to as the first AI winter.

The AI field survived by focusing on specific problems, called expert systems. In the early 1980s, a new rise was triggered by massive funding such as the Japanese Fifth Generation Computer project, aiming to build a supercomputer that could solve any problem. Shortly after, multi-layer neural networks were made possible with the (re)discovery of backpropagation [[Rumelhart1986](#)], or more rigorously of weight adjustment thanks to the backpropagation of error gradient, from the last layer to the first one. As it is not the central subject of this thesis, the algorithm and early references will not be detailed here, but the interested reader can refer to [[Goodfellow2016](#)]. This allowed for solving non-linearly separable problems, and for tackling real world issues (Figure 2.2c.). [[Cybenko1989](#)] proved that one single intermediate layer is enough to solve any given classification problem, granted that this layer contains enough neurons (although sometimes too many to make it possible in practice.) On the other hand, kernel tricks were also rediscovered [[Aizerman1964](#), [Hofmann2008](#)], and made non-neural networks such as support vector machines (SVMs) [[Boser1992](#)] able to treat non-linearly separable data with much less training data, more optimally, and on a clearer mathematical ground (Figure 2.4). However, again, unrealistic expectations were confronted with unplanned technical difficulties both on expert systems

and on general intelligence projects. This led to a second AI winter in the 1990s.

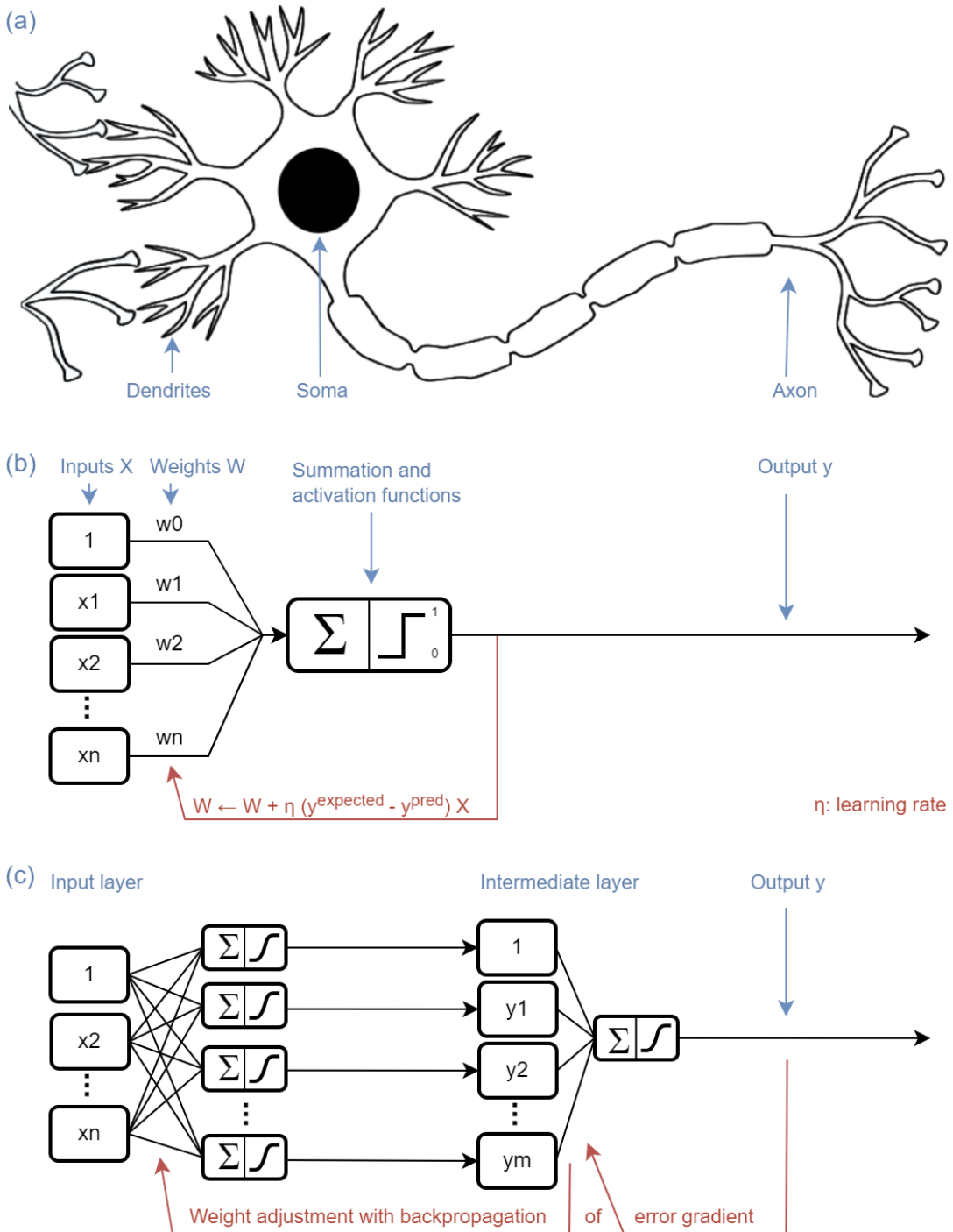


Figure 2.2: The artificial neuron (b) has been modeled after the natural neuron (a). Inputs and weights act as the total nervous influx firing the dendrites. The collected values are summed, and a signal is activated if a threshold is overcome, as the soma does in a natural neuron. The output signal is conveyed the axon in a natural neuron. (b) In the case of a perceptron, the neuron adjusts its weights to minimize the error between the predicted and the expected output. It can be used as a classifier, which outputs class 1 or class 0 depending on the inputs. (c) A dense (fully connected) neural network with one intermediate layer and backpropagation can solve any non-linearly separable classification.

Algorithm 1 Perceptron

Let \vec{X}^0 be the input vector of a first instance of variables $(1, x_1^0, \dots, x_M^0)$, \vec{W}^0 the corresponding weights randomly initialized $(w_0^0, w_1^0, \dots, w_M^0)$ with w_0^0 a bias, and $y^{0,pred}$ the output predicted binary class.

- 1: The summation function is computed:

$$\vec{W}^0 \cdot \vec{X}^0 = \sum_{m \in [0, M]} w_m^0 x_m^0 \quad (2.1)$$

- 2: This result is processed by an activation function, which is a threshold in the case of the perceptron. It determines whether the neuron will be fired or not, i.e., whether one or the other class will be predicted. $y^{0,pred} = 1$ corresponds to one class, and $y^{0,pred} = 0$ to the other.

$$y^{0,pred} = \begin{cases} 1 & \text{if } \vec{W}^0 \cdot \vec{X}^0 > \theta, \\ 0 & \text{otherwise} \end{cases} \quad (2.2)$$

- 3: This prediction $y^{0,pred}$ is compared to the actual class $y^{0,expected}$.

$$\varepsilon^0 = y^{0,expected} - y^{0,pred} \quad (2.3)$$

- 4: Then weights are updated:

$$\vec{W}^1 = \vec{W}^0 + \eta \varepsilon^0 \vec{X}^0 \quad (2.4)$$

with η the learning rate $\in [0,1]$. Note that if the class is correctly predicted, then $\varepsilon^0 = 0$ and weights are not adjusted.

- 5: The algorithm is repeated with another example \vec{X}^1 , and so on until it has gone through the whole batch of the training set. If weights still need to be updated, one can go over it again, for a determined number of epochs or until the average error is under a given value. Then the perceptron is considered trained, and ready to correctly predict a class y with the retained weights.
-

Example 1 Athlete classification with a perceptron

N.B. The code for running this example is available on the thesis repository
https://github.com/davidpagnon/These_David_Pagnon/blob/main/Thesis/Chap2/perceptron.py.

Let's consider force-velocity test results as an input

$$\vec{X} = (1, \text{velocity (m/s)}, \text{force (hN)}),$$

and the classification of an athlete as "good" or "bad" as an output $y = 1$ or 0 .

A batch of training data, i.e., example data the perceptron will learn from, could be:

$$\{(\vec{X}^i, y^{i,expected})\}_{i \in [0,4]} = \{((1, 1, 5), 1), ((1, 2, 3), 0), ((1, 7, 1), 1), ((1, 4, 1), 0), ((1, 5, 4), 1) \}.$$

Let's randomly initialize weights at $\vec{W}^0 = (-9, 1, 3)$, take a threshold $\theta=0.1$, and a learning rate $\eta = 0.3$.

The first instance of the training set gives:

$$\vec{W}^0 \cdot \vec{X}^0 = \sum_{m \in [0,2]} w_m^0 x_m^0 = -9 \times 1 + 1 \times 1 + 3 \times 5 = 7.$$

Now $\vec{W}^0 \cdot \vec{X}^0 = 7 > \theta = 0.1$, so $y^{0,pred} = 1$.

$y^{0,expected} = 1 = y^{0,pred}$, so the prediction is true and weights don't need to be updated.
As a consequence, $\vec{W}^1 = \vec{W}^0 = (-9, 1, 3)$.

The second instance gives $\vec{W}^1 \cdot \vec{X}^1 = (-9, 1, 3) \cdot (1, 2, 3) = 2 > \theta = 0.1$, so $y^{1,pred} = 1$.

But $y^{1,expected} = 0 \neq y^{1,pred} = 1$, so weights need to be updated.

The error is $\epsilon^1 = y^{1,expected} - y^{1,pred} = 0 - 1 = -1$.

As a consequence, $\vec{W}^2 = \vec{W}^1 + \eta \epsilon^1 \vec{X}^1 = (-9, 1, 3) + 0.1 \times (-1) \times (1, 2, 3) = (-9.3, 0.4, 2.1)$.

Third instance: $\vec{W}^2 \cdot \vec{X}^2 = (-9.3, 0.4, 2.1) \cdot (1, 7, 1) = 3 - 4.4 < 0.1$, so $y^{2,pred} = 0$.

$y^{2,expected} = 1 \neq y^{2,pred} = 0$, so weights need to be updated.

$\epsilon^2 = y^{2,expected} - y^{2,pred} = 1$.

$\vec{W}^3 = \vec{W}^2 + \eta \epsilon^2 \vec{X}^2 = (-9.3, 0.4, 2.1) + 0.1 \times 1 \times (1, 7, 1) = (-9, 2.5, 2.4)$.

Fourth instance: $\vec{W}^3 \cdot \vec{X}^3 = (-9, 2.5, 2.4) \cdot (1, 4, 1) = 3.4 > 0.1$, so $y^{3,pred} = 1$.

$y^{3,expected} = 0 \neq y^{3,pred} = 1$, so weights need to be updated.

$\epsilon^3 = y^{3,expected} - y^{3,pred} = -1$.

$\vec{W}^4 = \vec{W}^3 + \eta \epsilon^3 \vec{X}^3 = (-9, 2.5, 2.4) + 0.1 \times (-1) \times (1, 4, 1) = (-9.3, 1.3, 2.1)$.

Fifth instance: $\vec{W}^4 \cdot \vec{X}^4 = (-9.3, 1.3, 2.1) \cdot (1, 5, 4) = 17.6 > 8$, so $y^{4,pred} = 1$.

$y^{4,expected} = 1 = y^{4,pred} = 1$, so weights don't need to be updated.

$\vec{W}^5 = \vec{W}^4 = (-9.3, 1.3, 2.1)$ (Figure 2.3).

Next instances: Once we have gone over the batch of training data, if the average error is below a given value, we can assume that the perceptron is trained. If not, we can use the next batch to pursue training. If it still didn't converge after all batches, we can iterate over all training data again, for a given number of times. If results are still not satisfying, either the data are not linearly separable, or the training sample is not large enough or of good enough quality. In our case, it seems like our example data have allowed us to correctly separate good and bad athletes based on their force and velocity test results (Figure 2.3).

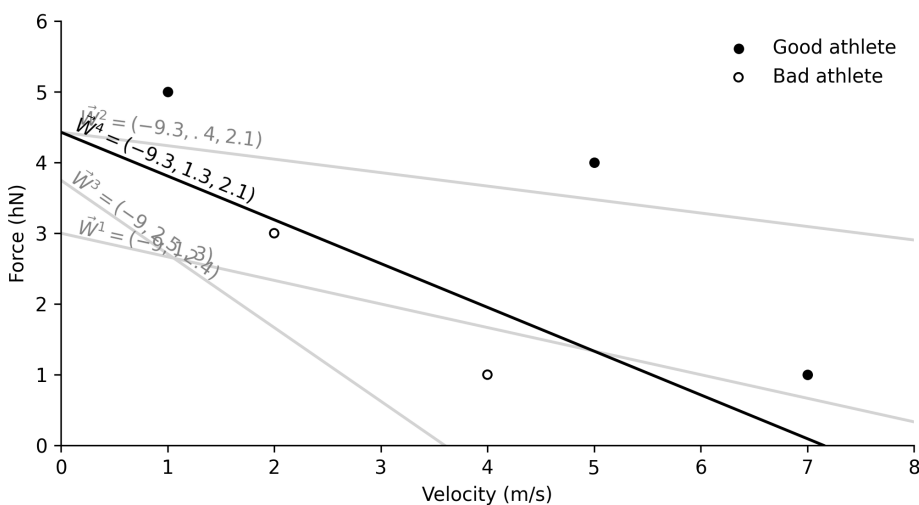


Figure 2.3: Classification of athletes as "good" (black dot) or "bad" (circle) according to their Force-Velocity results. Weights are adjusted (grey lines), until the perceptron classifies athletes correctly (black line.)

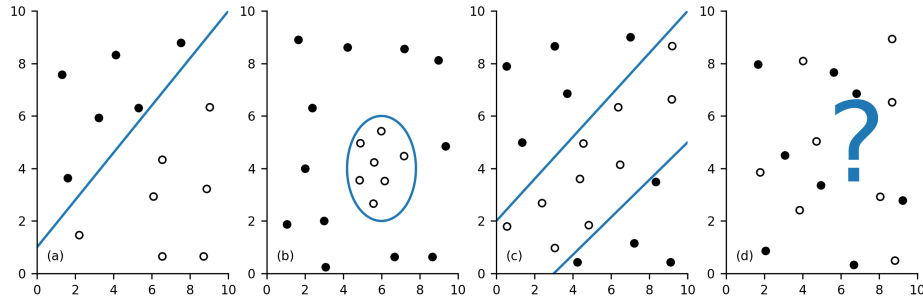


Figure 2.4: Single layer artificial neural networks such as the perceptron can only classify linearly separable data. (a) is linearly separable. (b) is not linearly separable. However, data are contained in an ellipse. The equation of an ellipse is of the form $a \times x^2 + b \times y^2 = 1$, so if we transform the feature variables into $X = x^2$ and $Y = y^2$, the data become linearly separable. (c) is equivalent to a fundamental XOR gate, and is not linearly separable, which was part of the reasons for the first AI winter. It can either be solved by combining several layers of artificial neurons, or by complex kernel tricks which map the data from the original space into a higher dimensional space where they become linearly separable. (d) is possibly not separable at all. AI: Artificial Intelligence. XOR: Exclusive OR.

From the end of the 1990s, there has been no theoretical breakthrough in AI, but larger databases have become available with the advent of the Internet, and greater computational power has become accessible, especially thanks to groundbreaking progress in Graphics Processing Units (GPUs), which made heavy parallel computing available to the wider audience. As a consequence, more layers could be used in neural networks, which progressively set off the onset of deep learning. Finally, complex "common-sense" problems, such as natural language processing or image recognition, could be treated with some success [Baral2018].

One particular type of deep learning algorithms is the convolutional neural network (CNN), which is particularly suited for image recognition. It was first used for classifying handwritten and low-resolution digits [LeCun1998], and then applied to more complex images as greater computing resources became available [Krizhevsky2017]. Nowadays, CNNs have sometimes surpassed humans at image classification [Cireşan2012, Lu2015]. A convolution layer consists in a series of filters that slide across the image, each of them outputting a result close to 0 or to 1, depending on how well it can be overlaid on each image area. In the same way as with a simple artificial neuron, each of these filters can be seen as a weight vector \vec{W} , and each image area as an input vector \vec{X} . The filters of the first convolution layer are simple patterns such as lines, but then they become circles and corners, until the last layers, when they have developed into complex features corresponding to whole object parts. Once a filter has covered the whole image, it forms a feature map, which will then be downsampled by a pooling layer in order to save computing resources. All the feature maps produced by each filter are processed by a determined number of other convolution layers, and then flattened into a 1D vector. This 1D vector is processed by a few dense layers (dense layers are fully connected, i.e., all outputs are produced by a weighted sum of each input), and lastly a softmax layer computes a probability for the image to correspond to each available class. If the CNN is correctly trained, the class with highest probability corresponds to the correct one: for example, if the image displays a BMX start, the probability for the bike class will be the highest (Figure 2.5).

However, results will not be good until a lot of iterations are done on a lot of data. Indeed, filters at each layer are randomly initialized, and then refined with backpropagation in order to predict all classes as best as possible. One of the risks is overfitting, i.e., to excessively adapt to the training data and to fail to generalize to new data. This is dealt with by cross-validation, i.e., the separation between training and test data, by regularization methods such as batch nor-

malization and dropout, and by data augmentation, e.g., image rotations, crops, color distortion, noise addition, etc. [Hawkins2004, Chicco2017]. An enormous amount of data is also needed to correctly train the CNN, which makes it complicated when unusual classes need to be recognized (for example, a climbing hold, a BMX starting gate, a medial malleolus on the ankle, etc.) Fortunately, one can consider that a CNN trained on a massive dataset, such as ImageNet and its 14 million annotated images [Deng2009], has learned to recognize most features that can be found in any image. One can take the learned filters of its convolutional layers as is, use them as a feature extractor (sometimes called backbone), and just fine-tune the last dense layers to recognize new classes. It will be much less computationally expensive to train, and will need much fewer data: about a hundred images, instead of thousands. This is called transfer learning [Pan2009].

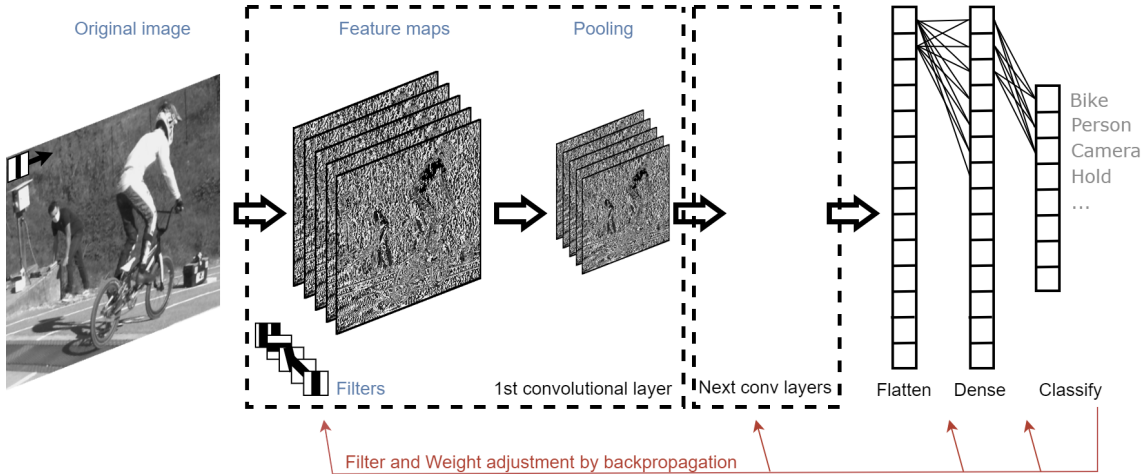


Figure 2.5: A simplified convolutional neural network (CNN.) A convolutional layer consists in a series of filters running across the input image, and producing feature maps, which are then downsampled by pooling. Filters become more and more elaborated along layers, and produce feature maps which look like whole object parts. Filters and weights are randomly initialized at first, and then are adjusted by backpropagation. After the convolutional layers, the feature maps are flattened to produce a 1D vector, which is then processed by dense layers, and finally a softmax layer computes a probability for the image to correspond to each available class.

Now, classification of a whole image is not sufficient in sports motion analysis. One needs to detect where an object or a person is, and ideally to localize more precise features such as joint centers so as to estimate the person's pose.

2.1.3 Machine learning for 2D pose detection

Older methods for object detection used to run a sliding and pyramidal window across the image, and then to apply a non-neural classifier on each window, such as an SVM on carefully handcrafted histogram of oriented gradients descriptors (HOG) [Dalal2005]. They then had to be followed by non-maximum suppression, in order to select one bounding box over many overlapping ones. As the classifier is run on each window iteration like if they were independent images, these methods were very computationally intensive, and in the same time not very robust nor accurate.

More modern approaches are based on CNNs, and as such, they involve a preliminary step: extracting the last layer of a pre-trained neural network such as ImageNet, in order to make it able to classify the objects of interest. One of the precursors, R-CNN (Regions with CNN features) [Girshick2014], first looks for a lesser amount of regions of interest (ROIs) by selective search, instead of with a sliding window. Selective search is an algorithm which segments image based on pixel intensities, without any learning involved [Uijlings2013]. Then three learning models

are used: one CNN for extracting features from each ROI, an SVM for classifying each ROI, and a regression model for adjusting bounding boxes. It takes about 45 seconds to process a single image on benchmarks. Fast R-CNN [Girshick2015] uses one single network for all steps, and switches the first two: it first extracts features from the whole image, and only then uses selective search to find ROIs on the resulting feature map, and finally classifies the ROIs and tightens the bounding boxes. It is much faster and takes about 2 seconds per image. A last incrementation on this basis is Faster R-CNN [Ren2015], which works similarly to the latter, but finds ROIs with a neural network instead of with selective search, which is very time-consuming. This allows for predicting an "objectness" score on each ROI, and for fitting the bounding boxes directly, and thus on avoiding the last regression step. It is even faster, and takes about 0.2 seconds per image. YOLO (standing for You Only Look Once) [Redmon2016] proposes another approach, and does not separate the steps of finding ROIs with classification. It divides the image into regions, and predicts both classes and bounding boxes for each region. For example, if there is a shoulder in a region, it will predict a "person" class, and a larger box in which this person is likely to fit. YOLO takes about 0.02 seconds per image (45 fps), and is thus able to run real time. However, it is not as accurate as the previous methods, especially on smaller objects. This being said, new versions are very frequently released (although not by the same authors), and the current YOLOv7 [Wang2022a] is both faster and more accurate than all previous approaches as it entirely reviews the whole network architecture to deal with all observed bottlenecks.

But again, in order to perform joint kinematics, one cannot just detect whole objects: precise keypoints need to be localized. Mask R-CNN [He2017] still predicts the bounding boxes and their class like Faster R-CNN does, but it also adds a small overhead in parallel, which predicts the shapes of masks overlaying the object in a pixel-to-pixel manner. Keypoints can be seen as a very small mask, and Mask R-CNN can also detect them in order to predict human pose estimation. In the next paragraph, only multi-person pose estimation models will be considered. Datasets, evaluation metrics, and comparison of results won't be detailed: see [Topham2021] for a comprehensive overview.

Two main approaches for multi-person 2D pose estimation coexist. The "top-down" one first detects bounding boxes around persons, and then finds keypoints inside each box. In the area of object detection methods, they are analogous to region-proposed methods such as the R-CNN suite, which propose ROIs and then find and classify objects. Conversely, the "bottom-up" approach first finds keypoints, and then groups them into persons. They are analogous to the single-shot object detection methods such as the YOLO suite, which first find small details, and then predict full-size objects. These approaches are nowadays almost as fast as the top-down ones, however their inference time does not increase with the amount of persons detected.

Mask R-CNN belongs to the first kind, as well as AlphaPose [Fang2017], which mostly differentiates from the latter by using a network predicting higher quality bounding boxes from inaccurate ones, in order to facilitate the task of the joint regressor. On the opposite, DeepCut and DeeperCut [Pishchulin2016, Insafutdinov2016], as well as DeepLabCut [Mathis2018, Lauer2022] upon which it is built, are bottom-up approaches. They find a large number of keypoint candidates, label them as hand, head, etc., and then select the best candidates and separate them into persons. Since they calculate every possible association between keypoints, this is very slow. OpenPose [Cao2019] uses a network which jointly predicts keypoint locations, and the connections between them (i.e., it also predicts limbs, which define a skeleton), and is much faster while still being accurate. OpenPifPaf [Kreiss2022] adds to it both temporal consistency across frames, and an intensity map for each keypoint instead of punctual locations (i.e., a further keypoint will have a lower intensity). This allows for better accuracy in low-resolution regime and in occluded images. YOLOv7 supports keypoint detection by integrating YOLO-Pose [Maji2022], and claims to be faster and more accurate than all other state-of-the-art methods. It brings together top-down and bottom-up approaches, and uses a single network predicting both bounding boxes and their corresponding poses. SLEAP [Pereira2022], which is built for training animal pose estimation

models, implements both top-down and bottom-up approaches. In this context, top-down approaches are slightly more accurate, and considerably faster as long as few animals are in the scene.

Like all previously presented methods, OpenPose has been trained the COCO dataset [Lin2014]. However, OpenPose body_25 standard model provides foot keypoints, which are primordial in sports motion analysis. To do so, 6 more keypoints have been labeled for the feet on the COCO dataset before training. OpenPose also supports the single-network whole-body pose estimation network [Hidalgo2019], which has been trained in the same time on COCO+foot, MPII [Andriluka2014], and on Total Capture [Xiang2019] in order to provide hand, face, feet, and body keypoints in one single network. A submodel of it is body_25b, which provides body and foot keypoints as body_25 does (although in slightly different locations), and in addition decreases the number of false positives without hampering speed (Figure 3.7). In a similar way, AlphaPose provides full-body models, either trained on the Halpe dataset [Li2020], or on the COCO-WholeBody one [Xu2022]. Note that BlazePose [Bazarevsky2020], trained on the GHUM dataset [Xu2020a], also provides hand and feet keypoints, but since it is a single-person pose estimation model, the architecture is different and will not be addressed here. Indeed, this is rarely suitable in sports conditions, where people are usually present in the background.



Figure 2.6: The body_25b OpenPose model is more accurate than the default body_25 one. As an example, the left knee is slightly misplaced on the default model. Keypoint definition and order also differ between both models.

2.2 3D reconstruction

Once the pose of an athlete is correctly detected, the next step is to obtain their 3D pose. While some approaches strive to infer 3D pose from a monocular video source, they are generally not considered sufficiently accurate, especially when body parts are occluded. It is, then, important to use several cameras, and to fuse their 2D pose estimation results to obtain more reliable 3D coordinates.

2.2.1 Pinhole camera model

camera coordinate system

2.2.2 Calibration

test

2.2.3 Triangulation

Algorithm 2 for a proof of the classic direct linear transform (DLT), commonly used to solve the triangulation of 2D coordinates from several cameras with a least square approach.

2.3 3D joint kinematics

2.3.1 Physically consistent model

autre

2.3.2 Scaling

bref

2.3.3 Inverse kinematics

As opposed to forward kinematics

Compare with 2D angles between 3 points

Different methods (model based vs autres) for angles (cf mail starred)

Algorithm 2 Direct Linear Transform (DLT)

Let $\vec{Q} = (X, Y, Z, 1)$ be the homogeneous coordinates of a 3D object point,
 $\vec{q} = (u, v, 1)$ the homogeneous coordinates of a 2D image point on a given camera,
 $\mathbf{P} = (P_1^T, P_2^T, P_3^T, P_4^T)$ the projection matrix of the same camera, with $P_1^T, P_2^T, P_3^T, P_4^T$ the rows
of \mathbf{P} , and λ an unknown scale factor.

1: The equation

$$\lambda \vec{q} = \mathbf{P} \vec{Q} \quad (2.5)$$

may be written as

$$\begin{aligned} \lambda u &= P_1^T \vec{Q}, \\ \lambda v &= P_2^T \vec{Q}, \\ \lambda &= P_3^T \vec{Q}, \end{aligned} \quad (2.6)$$

which gives two equations:

$$\begin{aligned} (P_1^T - uP_3^T) \vec{Q} &= 0, \\ (P_2^T - vP_3^T) \vec{Q} &= 0 \end{aligned} \quad (2.7)$$

2: With N cameras, we obtain a system of 2N equations that can be written in the form:

$$\mathbf{A} \vec{Q} = 0. \quad (2.8)$$

3: A singular value decomposition (SVD) of \mathbf{A} gives

$$A = \mathbf{U} \mathbf{S} \mathbf{V}^T \quad (2.9)$$

with \mathbf{U}, \mathbf{V} orthonormal basis, and \mathbf{S} the diagonal matrix filled with the singular values of \mathbf{A} ,
namely $\sigma_1, \sigma_2, \sigma_3, \sigma_4$. \vec{Q} can be expressed as

$$\vec{Q} = \mathbf{V} \vec{\alpha}, \quad (2.10)$$

with $\vec{\alpha} = \begin{pmatrix} \alpha_1 \\ \alpha_2 \\ \alpha_3 \\ \alpha_4 \end{pmatrix}$. The Python function `numpy.linalg.svd()` can swiftly compute SVDs.

-
- 4: Unless all projection matrices and all image points are perfectly determined, $\mathbf{A}\vec{Q} \neq 0$. However, it is possible to find a least square solution for our 3D object point \vec{Q} . Indeed, minimizing $(\mathbf{A}\vec{Q})^2$ also minimizes $\mathbf{A}\vec{Q}$.

$$\begin{aligned}
 (\mathbf{A}\vec{Q})^2 &= (\mathbf{A}\vec{Q})^T(\mathbf{A}\vec{Q}) \\
 &= (\vec{\alpha}^T \mathbf{V}^T \mathbf{V} \mathbf{S} \mathbf{U}^T)(\mathbf{U} \mathbf{S} \mathbf{V}^T \mathbf{V} \vec{\alpha}) \\
 &= \vec{\alpha}^T \mathbf{S} \vec{\alpha} \\
 &= \sum_{i \in [1,4]} \alpha_i^2 \sigma_i^2
 \end{aligned} \tag{2.11}$$

which is minimum when all α factors are set to zero, except the factor of the smallest singular value σ .

- 5: Assuming that $\sigma_{min} = \sigma_4$, then $(\mathbf{A}\vec{Q})^2$ is minimum when $\alpha_1, \alpha_2, \alpha_3$ are null.

$$(\mathbf{A}\vec{Q})_{min} = \alpha_4 \sigma_4 \tag{2.12}$$

and

$$\vec{Q} = \mathbf{V}\vec{\alpha} = \begin{pmatrix} V_{11} & V_{12} & V_{13} & V_{14} \\ V_{21} & V_{22} & V_{23} & V_{24} \\ V_{31} & V_{32} & V_{33} & V_{13} \\ V_{41} & V_{42} & V_{43} & V_{44} \end{pmatrix} \begin{pmatrix} 0 \\ 0 \\ 0 \\ \alpha_4 \end{pmatrix} = \alpha_4 \begin{pmatrix} V_{14} \\ V_{24} \\ V_{34} \\ V_{44} \end{pmatrix} = \begin{pmatrix} X \\ Y \\ Z \\ 1 \end{pmatrix} \tag{2.13}$$

- 6: As a consequence, the triangulated point is equal to

$$\vec{Q} = \begin{pmatrix} X \\ Y \\ Z \\ 1 \end{pmatrix} = \begin{pmatrix} V_{14}/V_{44} \\ V_{24}/V_{44} \\ V_{34}/V_{44} \\ 1 \end{pmatrix} \tag{2.14}$$

3

Proposed solution: Pose2Sim Python package

We propose the Pose2Sim python package, as an alternative to the more usual marker-based motion capture methods. Pose2Sim stands for "OpenPose to OpenSim", as it uses OpenPose inputs (2D keypoints coordinates obtained from multiple videos) and leads to an OpenSim result (physically consistent full-body 3D joint angles). Code is available at <https://github.com/perfanalytics/pose2sim>.

This chapter is adapted from the article published in the Journal of Open Source Software: "Pose2Sim: An Open-source Python Package for multiview markerless kinematics" [Pagnon2022b].

Contents

3.1	Introduction to the workflow	29
3.2	Installation and demonstration	30
3.2.1	Installation	30
3.2.2	Demonstration Part-1: Build 3D TRC file on Python	31
3.2.3	Demonstration Part-2: Obtain 3D joint angles with OpenSim	33
3.3	Method details	34
3.3.1	Project	34
3.3.2	2D keypoint detection	34
3.3.3	Camera calibration	35
3.3.4	Tracking the person of interest	36
3.3.5	Triangulating	36
3.3.6	Filtering and other operations	37
3.3.7	OpenSim scaling and inverse kinematics	37
3.4	Limitations and perspectives	39
3.4.1	Issues related to OpenPose	39
3.4.2	Multi-person analysis	40
3.4.3	User-friendly calibration	41
3.4.4	Visualization tools	41
3.4.5	Real-time analysis	43
3.4.6	Other perspectives	43

3.1 Introduction to the workflow

Although some developments are relevant to both, specifics differ between medicine and the sports field. In this regard and as stated in the [Statement of need](#), marker-based methods are not well suited for sports motion analysis [Colyer2018]. In sports, capture should not hinder the movement. Placing markers on the naked body takes time and is cumbersome, therefore markerless approaches are favored. Sports environments are usually much more challenging than lab settings: frequent occlusions, fast and unusual movements, and complex background make it important to resort to using multiple view points, from RGB rather than RGB-D cameras, processed with machine learning methods. Competition conditions are often fast-paced and congested, so a light-weight, fast, and easy to set up system is relevant. However, as coaches and athletes usually need a mere feedback rather than a definitive diagnosis, they don't need as thorough of an accuracy as physicians. Ideally, results should be given in real time, and they should be more visual than graphs of time series. Moreover, 3D kinematics are more relevant than 2D sagittal plane kinematics; and full-body analysis (including upper-limb) is desired.

We propose the Python package Pose2Sim [[Pagnon2022b](#)], which aims to deal with these constraints. It provides a framework for 3D markerless kinematics, as an alternative to the more usual marker-based motion capture methods. Pose2Sim stands for "OpenPose to OpenSim", as it uses OpenPose inputs (2D coordinates obtained from multiple videos) [[Cao2019](#)] and leads to an OpenSim result (full-body 3D joint angles) [[Delp2007](#), [Seth2018](#)]. Pose2Sim is accessible at <https://github.com/perfanalytics/pose2sim>.

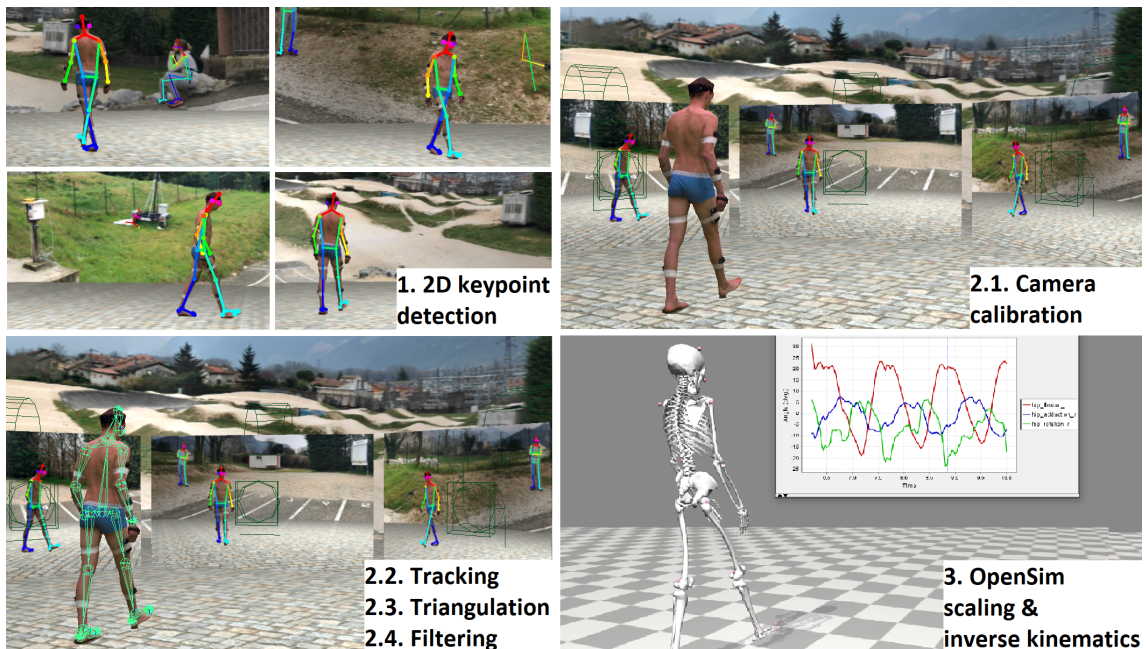


Figure 3.1: Pose2Sim full pipeline: (1) 2D keypoint detection; (2.1) Camera calibration; (2.1-2.4) Tracking of the person of interest, Triangulating of keypoint coordinates; and Filtering; (3) Constraining the 3D coordinates to an individually scaled, physically consistent OpenSim skeletal model.

The repository presents a framework which consists in (Figures 3.1):

1. Preliminary 2D joint coordinate detections from multiple videos, e.g. with OpenPose.
2. Pose2Sim core, including 4 customizable steps:
 - 2.1. Camera calibration.
 - 2.2. 2D tracking of the person of interest.
 - 2.3. 3D keypoint triangulation.
 - 2.4. 3D coordinate filtering.
3. Scaling a full-body skeleton to each individual subject, and computing inverse kinematics via OpenSim so as to obtain 3D joint angles.

Each task is easily customizable, and requires only moderate Python skills. The whole workflow runs from any video cameras, on any computer, equipped with any operating system (although OpenSim has to be compiled from source on Linux.) It requires no marker placement, and the scaling and inverse kinematic steps are simpler than they are with markers-based methods. Overall, human intervention is scarce, which makes it more robust to human error. Pose2Sim has already been used and tested in a number of situations (walking, running, cycling, dancing, balancing, swimming, boxing), and published in peer-reviewed scientific publications assessing the quality of its code [Pagnon2022c], its robustness (see Chapter 4 on [Robustness assessment](#)) [Pagnon2021] and its accuracy (see Chapter 5 on [Accuracy assessment](#)) [Pagnon2022a]. Its results for inverse kinematics were deemed good when compared to marker-based ones, with errors generally below 4.0° across several activities, on both lower and on upper limbs. The combination of its ease of use, customizable parameters, and high robustness and accuracy makes it promising, especially for "in-the-wild" sports movement analysis.

3.2 Installation and demonstration

3.2.1 Installation

1. Install **OpenPose** ([instructions here](#)).

Windows portable demo is enough.

2. Install **OpenSim 4.x** from [there](#).

Tested up to v4.4-beta on Windows. Has to be compiled from source on Linux (see [there](#)).

3. *Optional:* Install **Anaconda** or **Miniconda**.

Open an Anaconda terminal and create a virtual environment by typing:

```
conda create -n Pose2Sim python=3.8.8
conda activate Pose2Sim
```

4. Install **Pose2Sim**

If you don't use Anaconda, type `python -V` in terminal to make sure `python>=3.6` is installed.

- OPTION 1: *Quick install.* Type in terminal:

```
pip install pose2sim
```

- OPTION 2: *Build from source.* Open a terminal in the directory of your choice and clone the Pose2Sim repository:

```
git clone https://gitlab.inria.fr/perfanalytics/pose2sim.git
cd pose2sim
pip install .
```

3.2.2 Demonstration Part-1: Build 3D TRC file on Python

This demonstration provides an example experiment of a person balancing on a beam, filmed with 4 calibrated cameras processed with OpenPose.

Open a terminal and check package location with `pip show pose2sim | grep Location`. Copy this path and go to the Demo folder with `cd <path>\pose2sim\Demo``.

Type `python`, and test the following code (Figures 3.4):

```
from Pose2Sim import Pose2Sim
Pose2Sim.calibrateCams()
Pose2Sim.track2D()
Pose2Sim.triangulate3D()
Pose2Sim.filter3D()
```

You should obtain a plot of all the 3D coordinates trajectories (Figures 3.2). You can check the logs in `Demo\Users\logs.txt`. Results are stored as `.trc` files in the `Demo\pose-3d` directory (Figures 3.3). Note that when the functions are called without any argument, the Config file is searched in the default `Users\Config.toml` location. These parameters can be edited by the user.

RHip RKnee RAnkle RBigToe RSmallToe RHeel LHip LKnee LAnkle LBigToe LSmallToe LHeel Neck Head Nose RShoulder RElbow RWrist

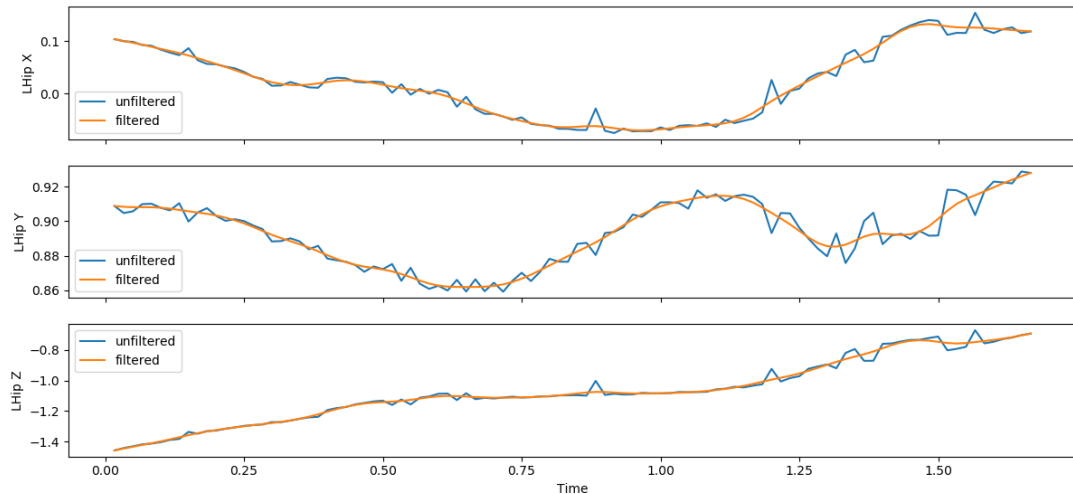


Figure 3.2: Filtered results. Each keypoint trajectory is displayed in a different tab.

Path	FileType	4 (X/Y/Z)	NumFrames	Demo_0-100.trc	NumMarkers	Units	OrigDataRate	OrigDataStartFrame	OrigNumFrames	RKnee	RAnkle	RBigToe		
Frame#	DataRate	CameraRate	Time	RHip	X1	Y1	Z1	X2	Y2	Z2	X3	Y3	Z3	X4
1	0.01666666667	-0.064972148	0.9015045551	-1.4005886926	-0.0396263662	0.4930973651	-1.4485228257	0.0437901401	0.1438754982	-1.5950846772	-0.0169084827			
2	0.0333333333	-0.0740068294	0.9044249595	-1.3887505524	-0.0396716745	0.4930610544	-1.4481465416	0.039886297	0.1434935164	-1.5931576221	-0.0169371875			
3	0.05	-0.0799400351	0.9088363315	-1.3905580361	-0.0372341964	0.4955765014	-1.4425663246	0.0424186998	0.1500265582	-1.5949272593	-0.0157499669			
4	0.06666666667	-0.0834212999	0.9118448511	-1.3790501541	-0.0378442483	0.4986109124	-1.4352189865	0.041841984	0.1505211073	-1.5951903296	-0.0159322546			
5	0.0833333333	-0.0821238866	0.910708592	-1.3705528594	-0.0415058215	0.4929167908	-1.4391550118	0.0368223321	0.1492766387	-1.5900002244	-0.0214821932			
6	0.1	-0.0870228272	0.9113842484	-1.356897099	-0.0434174115	0.4981952646	-1.4247995005	0.0306840105	0.1528813191	-1.5954295987	-0.0237343535			
7	0.1166666667	-0.0920100974	0.9116316951	-1.3447088632	-0.0445856424	0.5002300425	-1.4213497807	0.0290451125	0.1540803887	-1.5892342384	-0.0245350272			
8	0.1333333333	-0.0906673188	0.9161769285	-1.3309245886	-0.046053813	0.5073858348	-1.4072542077	0.0334937714	0.1591193395	-1.5866813244	-0.0225906144			

Figure 3.3: An example .trc file of triangulated keypoint coordinates, directly usable in OpenSim.

In [6]: `Pose2Sim.calibrateCams('User/Config.toml')`

```
Calibrating cameras...
--> Residual (RMS) calibration errors for each camera are respectively [0.221, 0.235, 0.171, 0.191] px,
    which corresponds to [0.402, 0.445, 0.45, 0.505] mm.
Calibration file is stored at [REDACTED]
```

(a) Calibration can either be done from a checkerboard, or by simply converting a Qualisys calibration file. Calibration errors are computed and provided.

In [11]: `Pose2Sim.track2D('User/Config.toml')`

```
Tracking the person of interest for Demo, for frames 0 to 100.
100% | [REDACTED] | 100/100 [00:00<00:00, 383.53it/s]
--> Mean reprojection error for Neck point on all frames is 12.3 px, which roughly corresponds to 22.4 mm.
--> In average, 0.01 cameras had to be excluded to reach the demanded 20 px error threshold.
Tracked json files are stored in [REDACTED]
```

(b) If several persons are detected in the scene, a tracking step can be carried out in order to make sure that the right person from each camera will be triangulated.

In [12]: `Pose2Sim.triangulate3D('User/Config.toml')`

```
Triangulation of 2D points for Demo, for frames 0 to 100.
D:\softs\github_david\Pose2Sim\Demo\calib-2d\Calib_qca.toml
100% | [REDACTED] | 100/100 [00:02<00:00, 33.71it/s]
Mean reprojection error for RHip is 8.0 px (~ 0.015 m), reached with 0.99 excluded cameras.
Mean reprojection error for RKnee is 9.4 px (~ 0.017 m), reached with 0.61 excluded cameras.
Mean reprojection error for RAnkle is 10.8 px (~ 0.02 m), reached with 0.1 excluded cameras.
Mean reprojection error for RBigToe is 10.9 px (~ 0.02 m), reached with 0.57 excluded cameras.
Mean reprojection error for RSmallToe is 10.6 px (~ 0.019 m), reached with 0.44 excluded cameras.
Mean reprojection error for RHeel is 11.1 px (~ 0.02 m), reached with 0.31 excluded cameras.
Mean reprojection error for LHip is 8.8 px (~ 0.016 m), reached with 0.83 excluded cameras.
Mean reprojection error for LKnee is 10.6 px (~ 0.019 m), reached with 0.8 excluded cameras.
Mean reprojection error for LAnkle is 12.3 px (~ 0.022 m), reached with 0.15 excluded cameras.
Mean reprojection error for LBIGToe is 10.2 px (~ 0.019 m), reached with 0.33 excluded cameras.
Mean reprojection error for LSmallToe is 11.2 px (~ 0.02 m), reached with 0.46 excluded cameras.
Mean reprojection error for LHeel is 10.6 px (~ 0.019 m), reached with 0.38 excluded cameras.
Mean reprojection error for Neck is 11.1 px (~ 0.02 m), reached with 0.17 excluded cameras.
Mean reprojection error for Head is 9.8 px (~ 0.018 m), reached with 0.56 excluded cameras.
Mean reprojection error for Nose is 8.4 px (~ 0.015 m), reached with 1.95 excluded cameras.
Mean reprojection error for RShoulder is 9.4 px (~ 0.017 m), reached with 0.61 excluded cameras.
Mean reprojection error for RElbow is 9.0 px (~ 0.016 m), reached with 0.63 excluded cameras.
Mean reprojection error for RWrist is 9.7 px (~ 0.018 m), reached with 0.49 excluded cameras.
Mean reprojection error for LShoulder is 10.2 px (~ 0.019 m), reached with 0.5 excluded cameras.
Mean reprojection error for LElbow is 12.1 px (~ 0.022 m), reached with 0.39 excluded cameras.
Mean reprojection error for LWrist is 11.6 px (~ 0.021 m), reached with 0.38 excluded cameras.
--> Mean reprojection error for all points on all frames is 10.3 px, which roughly corresponds to 18.8 mm.
--> Cameras were excluded if likelihood was below 0.3 and if the reprojection error was above 15 px.
In average, 0.55 cameras had to be excluded to reach these thresholds.
3D coordinates are stored at [REDACTED]
```

(c) The triangulation is weighted by the OpenPose likelihood, and constrained by some thresholds defined in the Config.toml file. If these constraints are not met, e.g., if the reprojection error is too large or if the likelihood of a keypoint is too low, one or several cameras are excluded. The mean reprojection error and the number of cameras that have been excluded to meet the constraints is printed, for each keypoints.

In [13]: `Pose2Sim.filter3D('User/Config.toml')`

```
Filtering 3D coordinates for Demo, for frames 0 to 100.
--> Filter type: Butterworth low-pass. Order 4, Cut-off frequency 6 Hz.
Filtered 3D coordinates are stored at [REDACTED]
```

(d) Triangulated data can be filtered, either with a low-pass Butterworth filter or with other types, and parameters can be adjusted.

Figure 3.4: First steps of Pose2Sim pipeline in Python. Calibration can either be done from a checkerboard, or by simply converting a Qualisys calibration file. Note that the functions can be used without any arguments if the Config.toml file is left in the default location.

3.2.3 Demonstration Part-2: Obtain 3D joint angles with OpenSim

In the same vein as we would do with marker-based kinematics, the model first needs to be scaled to each individual, and then inverse kinematics can be performed (Figures 3.5).

Scaling:

1. Open OpenSim.
2. Open the provided `Model_Pose2Sim_Body25b.osim` model from `pose2sim/Demo/opensim`. (File \mapsto Open Model)
3. Load the provided `Scaling_Setup_Pose2Sim_Body25b.xml` scaling file from `pose2sim/Demo/opensim`. (Tools \mapsto Scale model \mapsto Load)
4. Run. You should see your skeletal model take the static pose.

Inverse kinematics

1. Load the provided `IK_Setup_Pose2Sim_Body25b.xml` scaling file from `pose2sim/Demo/opensim`. (Tools \mapsto Inverse kinematics \mapsto Load)
2. Run. You should see your skeletal model move in the Vizualizer window.

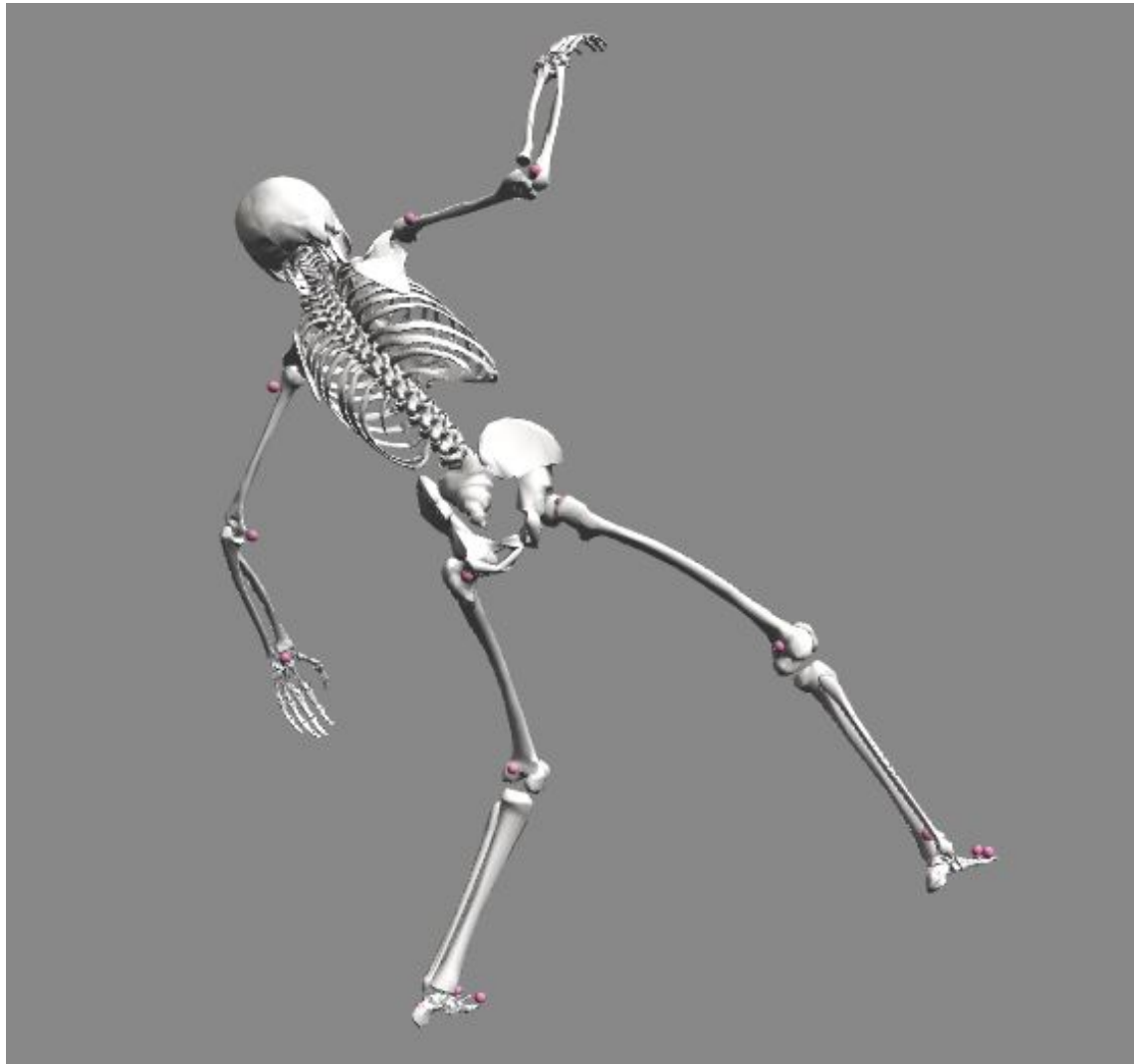


Figure 3.5: At the end of the demonstration, you should have a skeleton balancing on a beam in OpenSim.

3.3 Method details

3.3.1 Project

Pose2Sim is meant to be as fully and easily configurable as possible, by editing the `User/Config.toml` file. First of all, the user can specify the project path and folder names, the video frame rate, and the range of analyzed frames.

Optional tools are also provided for extending its usage (Figures 3.6). Among others, DeepLabCut 2D files can be converted to the OpenPose formalism, and calibration files from other platforms can also be converted to the AniPose [Karashchuk2021] formalism we use. 2D keypoint files can be displayed and stored as a video. Gait events can be detected from kinematic data thanks to [Zeni2008] algorithm. Some other scripts allow for further processing of 3D coordinates. More practical information can be found on the GitHub repository.

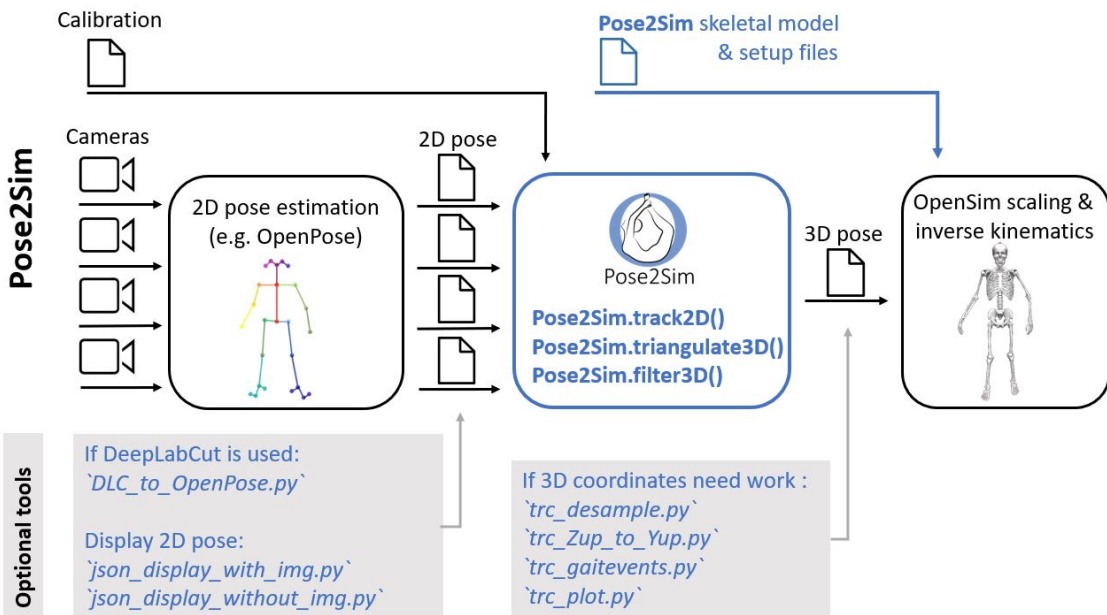


Figure 3.6: The Pose2Sim workflow, along with some optional utilities provided in the package.

3.3.2 2D keypoint detection

The interest in deep-learning pose estimation neural networks has been growing fast since 2015 [Zheng2022], which makes it now possible to collect accurate and reliable 2D landmark positions without the use of physical markers. OpenPose, for example, is a widespread open-source software which provides 2D joint coordinate estimates from videos. As it is the software we have extensively tested, we recommend choosing it.

Feet are usually needed in sports kinematic analysis, and OpenPose is one of the few programs which can detect them. Indeed, it comes with {body + feet} models such as body_25 or body_25B, as well as with a {body + feet + hands + face} one called body_135 [Hidalgo2019]. The latter two are more accurate than the standard body_25 one. However, body_135 requires high computational resources, unlike body_25B which is as fast as body_25, and which we have extensively tested [Pagnon2022a]. Its keypoint definition differs slightly to the default model's (Figure 3.7): it adds the MPII head and neck keypoints, and removes the artificially created neck and middle hip points of the body_25 model (which are simply the middle point of the shoulders and the hips). Hence, we recommend using it. Note that only 21 of the 25 detected keypoints are tracked, since eye and ear keypoints would be redundant in the determination of the head orientation.



Figure 3.7: The experimental body_25b OpenPose model is more accurate than the default body_25 one. See how the left knee is slightly misplaced on the default model. The keypoint definition differs between both models.

This being said, the user can choose any deep-learning pose estimation network. This choice will affect how keypoint indices will be mapped to model markers in OpenSim, corresponding to anatomical landmarks or joint centers. The OpenPose body_25, body_25B, body_135, COCO, and MPII models are fully supported. The AlphaPose COCO, COCO-WholeBody, and full-body HALPE models are also supported, as well as the full-body but single-person detection BlazePose model. COCO and MPII model are the ones generally used by other networks such as OpenPifPaf [Kreiss2022], YOLO-pose [Maji2022, Wang2022a], and others, which means that they are also supported. It is also possible to build custom skeletons in the `skeleton.py` file, trained for example with DeepLabCut [Mathis2018, Lauer2022] or SLEAP [Pereira2022]. They will be triangulated, but the user will need to build an OpenSim model and set the keypoints in the right place before being able to perform inverse kinematics.

Two optional standalone scripts are also provided if the user desires a visual display of the 2D pose estimation, as well as a tool for converting DeepLabCut data to OpenPose formalism (Figure 3.6).

3.3.3 Camera calibration

The user can indicate whether cameras are going to be calibrated with a checkerboard, or if a preexisting calibration file (such as one provided by a Qualisys system) will simply be converted.

If checkerboard calibration is chosen, the number of corners and the size of the squares have to be specified. In this case, the operator needs to take at least 10 pictures or one video per camera of the checkerboard, covering as much as the field of view as possible, with different orientations. Corners are then detected and refined with OpenCV [Bradski2000]. Detected corners can optionally be displayed for verification. Each camera is finally calibrated using OpenCV with an algorithm based on [Zhang2000]. The user can choose the index of the image which they want to be used as a reference for calculating extrinsic parameters. Residual calibration errors are given, and stored in a log file.

3.3.4 Tracking the person of interest

One needs to differentiate the people in the background from the actual subject. The tracking step examines all possible triangulations of a chosen keypoint among all detected persons, and reprojects them on the image planes. The triangulation with the smallest reprojection error is considered to be the one associated with the right person on all cameras. If the reprojection error is above a predefined threshold, the process is repeated after taking off one, or several cameras. This happens, for example, if the person of interest has exited the field of a camera, while another person is still in the background.

We recommend choosing the neck point or one of the hip points. In most cases they are the least likely to move out of the camera views.

3.3.5 Triangulating

Aside from ours, a number of tools have been made available for triangulating OpenPose data: the experimental OpenPose 3D reconstruction module [Hidalgo2021], the FreeMoCap Python and Blender toolbox [Matthis2022], or the pose3d Matlab toolbox [Sheshadri2020], and the EasyMoCap pipeline [EasyMocap2021].

Pose2Sim triangulation is robust, largely because instead of using classic Direct Linear Transformation (DLT) [Hartley1997], we propose a weighted DLT, i.e., a triangulation procedure where each OpenPose keypoint coordinate is weighted with its confidence score [Pagnon2021]. This is a good compromise between losing all confidence information, and triangulating the whole heatmap in a volumetric way [Iskakov2019], which is very slow. The weighted DLT has been independently introduced by [Barone2020], in the context of camera calibration. See Algorithm 3 for the proposed solution. For more details on the classic DLT, see Algorithm 2 in Chapter 2, section [Triangulation](#).

Algorithm 3 Weighted DLT

Our weighted DLT simply consists of weighing Equation 2.7 with the confidence c given by OpenPose for each camera. The rest of the procedure remains unchanged.

$$\begin{aligned} c \times (P_1^T - uP_3^T) \vec{Q} &= 0, \\ c \times (P_2^T - vP_3^T) \vec{Q} &= 0 \end{aligned} \tag{3.1}$$

Other parameters can be specified, such as:

- The minimum likelihood (given by OpenPose for each detected keypoint) below which a 2D point will not be taken into account for triangulation.
- The maximum in reprojection error above which triangulation results will not be accepted. This can happen if OpenPose provides a bad 2D keypoint estimate, or if the person of interest leaves the camera field. Triangulation will then be tried again on all subsets of all cameras minus one. If the best of the resulting reprojection errors is below the threshold, it is retained. If it is still above the threshold, one more camera is excluded.
- The minimum number of "good" cameras (i.e., cameras remaining after the last two steps) required for triangulating a keypoint. If there are not enough cameras left, the 3D keypoint is dropped for this frame.

Once all frames are triangulated, the ones with missing keypoint coordinates are interpolated. The interpolation method can also be chosen from among linear, slinear, quadratic, and cubic. The mean reprojection error over all frames is given for each point and saved to a log file, as well as the number of cameras excluded to reach the demanded thresholds. The resulting 3D coordinates are formatted as a .trc file, which can be read by OpenSim.

3.3.6 Filtering and other operations

Different filters can be chosen, and their parameters can be adjusted. The user can choose a zero-phase low-pass Butterworth filter [Butterworth1930] that they can apply either on keypoint positions or on their speeds, a LOESS filter [Cleveland1981], a Gaussian filter, or a median filter. Waveforms before and after filtering can be displayed and compared.

If needed, other standalone tools are provided to further work on the .trc 3D coordinate files (Figure 3.6). Among others, it is possible to undersample a file from a higher to a lower framerate, or to convert a file from Z-up to Y-up axis convention. The resulting 3D coordinates can be plotted for verification. Additionally, a tool is provided to detect gait events from point coordinates, according to the equations given by [Zeni2008].

3.3.7 OpenSim scaling and inverse kinematics

When it comes to the biomechanical analysis of human motion, it is often more useful to obtain joint angles than joint center locations. Joint angles allow for better comparison among trials and individuals, and they represent the first step for other analyses such as inverse dynamics.

OpenSim [Delp2007, Seth2018] is a widespread open-source software which helps compute consistent 3D joint angles, usually from marker coordinates. It lets scientists define a detailed musculoskeletal model, scale it to individual subjects, and perform inverse kinematics. Results are accurate and robust since biomechanical constraints can be adjusted and weighted, bones are set to a constant length, and joints limited to coherent angle limits. OpenSim provides other features such as net calculation of joint moments or resolution of individual muscle forces, although this is beyond the scope of our contribution.

The main contribution of Pose2Sim is to build a bridge between OpenPose and OpenSim. The OpenSim model needs to be carefully crafted. Indeed, inverse kinematics is an under-constrained problem, that can be guided with carefully chosen joint constraints. Pose2Sim provides a full-body model, adapted from the human gait full-body model [Rajagopal2016] and the lifting full-body model [Beaucage-Gauvreau2019]. The first one has a better definition of the knee joint, with a coupling relationship between knee flexion and abduction/adduction and internal/external rotation. This allows for 3D knee kinematics with only one degree of freedom. The latter model has a better definition of the spine: each lumbar vertebra is constrained to the next one, which makes it possible for the spine to bend in a coherent way with only a few tracked keypoints, without having to make it a rigid single bone. Combining those two models allows for ours to be as versatile as possible. Hand movements are locked, because the standard OpenPose models don't provide any hand detection. A ball joint was added between head and torso so that the rotation of the head could be roughly rendered.

The placement of markers on the model is also of paramount importance, especially with so little of them. OpenPose keypoints do not necessarily coincide with joint centers, probably because of systematic labelling errors in the training dataset [Needham2021b]. Moreover, they may be located in a different anatomical position when limbs are fully extended in comparison to when they are fully flexed. However, once the markers are positioned in accordance with those of the 2D pose estimations, the scaling step is very fast and straightforward since the marker placement will not change from one session, subject, or operator to another. Our model takes these labelling errors into account, and offsets model markers as regards true joint centers accordingly (Figure 3.8).

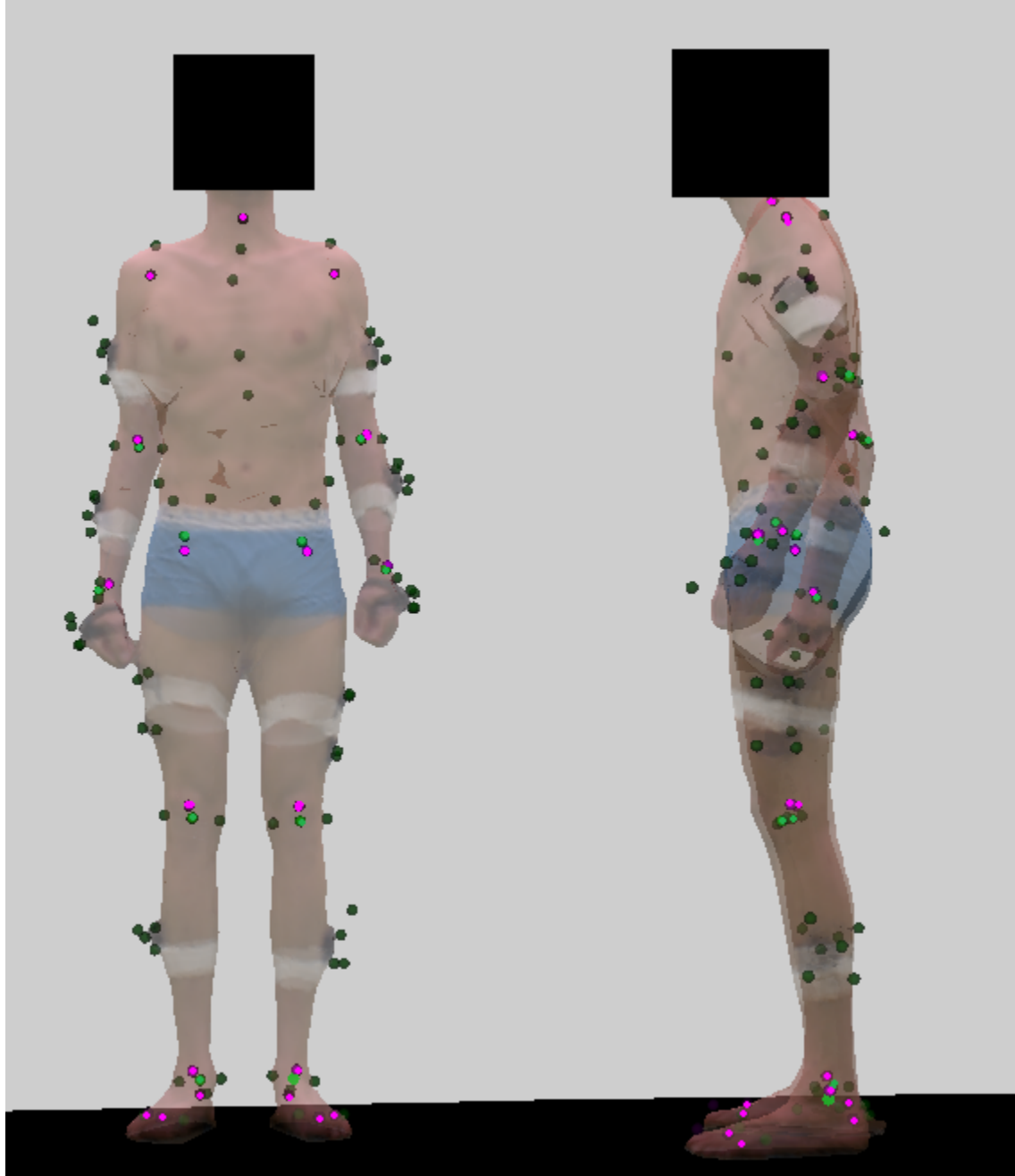


Figure 3.8: Triangulated anatomical markers and clusters (dark green), calculated joint centers (light green), and OpenPose body_25b keypoints (pink) on a textured mesh. OpenPose's eyes and ears keypoints were excluded. Mesh opacity was set to 0.5 in order to make all points visible. This view made it possible to precisely place OpenPose triangulated keypoints on the OpenSim model.

Scaling in OpenSim can be broken down into two parts: first, the proper scaling of the model, which adjusts bone dimensions and inertial properties according to the positions of the joint markers; second, the adjustment of the other markers on the model, especially anatomical and cluster markers. If the model is defined properly, there is no need for further marker adjustment on the model, since markers will not be subject to placement variation due to human error or to skin movement artifact. Each body is scaled according to a factor computed as a ratio of distances, defined by the distance between pairs of model markers over distance between corresponding pairs of experimental markers. The markers used for scaling are chosen as follows:

- Arm: distance between shoulder and elbow markers;
- Forearm: distance between elbow and wrist;
- Thigh: distance between hip and knee;
- Shank: distance between knee and ankle;
- Foot: distance between heel and big toe;
- Pelvis: distance between left and right hip;
- Torso: distance between neck and hip;
- Head: distance between head and nose;

All weights of joint coordinates are set to 1, apart from those of the nose and the head, which are set to 0.2, and from those of the other head markers, which are set to 0. Since we process scaling during a T-pose, we add as a condition that ankle flexion should be fixed at a neutral 0° angle.

The inverse kinematic tool is used with the same marker weights as in the scaling step.

Unlike in marker-based capture, keypoints detection hardly depends on the operator, the subject, nor the context. For this reason, the scaling and the inverse kinematic steps are straightforward, and the provided setup files require little to no adjusting.

3.4 Limitations and perspectives

3.4.1 Issues related to OpenPose

Pose2Sim is currently primarily used with OpenPose as a 2D pose detection network. Despite it is very robust, it suffers from issues when used for full-body kinematic analysis. First, keypoint localization suffers from systematic offsets when compared to actual joint center positions [Needham2021b]. Constraining these coordinates to a skeletal model largely reduces the detrimental impact of low-quality 2D joint center estimations. Nevertheless, these offsets have been taken into account in the provided OpenSim model, by shifting OpenPose keypoint placements with regard to marker-based calculated joint centers. This was done manually, but precisely, thanks to our overlayed view (see [Methods Chapter 5.2.](#)) However, OpenPose’s offset may not be the same when a limb is extended as when it is bent, which may influence kinematic results on extreme poses, such as seen in some sports. Hence, using a 2D pose estimation model free from systematic biases on all ranges of motion would certainly improve kinematic accuracy. The body_25b model is more accurate than the default body_25 one, but it is still biased.

Furthermore, both models only detect 25 keypoints. This makes inverse kinematics an under-constrained problem, which has to be guided with carefully chosen joint constraints, and with precise placement of markers on the model. But ultimately, OpenSim global optimization cannot solve some internal/external rotations around limbs, nor angles at the shoulder, spine, and pelvis joints. Additionally, there is no marker for the hand, which does not allow for capture of any pronation/supination movement. Using the experimental body_135 OpenPose model would solve the hand issue, but it would also greatly increase the computational cost and would leave the shoulder and spine problem unaddressed. As a consequence, and provided that they are reliably labeled, OpenPose needs more keypoints to solve these indeterminations, and potentially several per joints, in the same way as markersets are designed in marker-based methods. Pose2Sim could operate with such a model, although new keypoints should then be placed afresh on the unscaled OpenSim model.

Moreover, OpenPose struggles to accurately detect pose when the person is upside-down, or taking an unusual pose. One way to solve this is enhancing the OpenPose dataset, by augmenting it with larger rotations so that upside-down poses are recognized, or by training it on specific sports

poses. One risk of this approach is that the model may perform better on specific extreme poses, but worse on standard ones [Kitamura2022].

Another approach, which could solve altogether the offsets in labeling, the dearth of keypoints, and the lack of accuracy on sports poses, could be to train on a whole new dataset. Note that this dataset should not base its labeling on marker positions, which could be interpreted as visual cues, that are not available in real sports situations. However, this condition is not sufficient: the dataset should also be large and diverse enough, represent a wide variety of body types and of sports movements [Seethapathi2019], and include images with motion blur such as found in sports videos. One way to do it is to build a synthetic dataset. For example, a mass of c3D motion files could be gathered from various sports, and be used to fit an SMPL+H mesh [Pavlakos2019] with AMASS [Mahmood2019]. These data could be augmented with already existing datasets for daily life activities, such as Agora [Patel2021]. Then, it would be possible to take advantage of the fact that the topology of an SMPL mesh is constant, and assume that only labelling the first frame of any given sequence should be sufficient: label positions should be consistently propagated to the next frames. At this stage, one could place as many virtual markers as needed, for a precise evaluation of any movement and pose. However, only an expert should perform this task, and make sure that markers are correctly positioned: crowd-sourcing this task, like it is done for more basic image classification and segmentation with ImageNet [Deng2009], has been proved to lead to systematic offset errors [Needham2021b]. Finally, random clothing, background, and light could be added (see [Wood2021, Bolaños2021] for a detailed workflow), as well as variations in SMPL shape parameters. The scene would be filmed with numerous virtual cameras, in order to gather a large amount of diverse perspectives, and virtual markers would be automatically projected on the camera planes. This would result in an extensive sports dataset, created with minimal labelling work, on a potentially infinite amount of views. Nevertheless, before training the network, one should make sure that the generated data is as diverse as the real world, by using one of the metrics proposed by [Borji2019, Borji2022]. Additionally, keypoint positions need to be precise enough: SMPL shape vertices can sometimes be more than 5 cm apart, which could cause imprecision errors similar to skin artifacts. Besides, instead of constraining pose estimation results with a physically consistent skeletal model, it would be interesting to develop a physics-informed pose estimation model [Raissi2019], which would offer the opportunity of embedding the kinematics priors as early as possible in the learning process.

On a different note, in a sports context, not only the human pose is of interest: sports gear can also be considerably important to detect, such as a ball [Ghasemzadeh2021], skis [Ludwig2020], or bike parts in the context of cycling (see Chapter 7 on [Joint OpenPose and DeepLabCut detection](#)). This can help to analyze game dynamics, and to quantify posture cues related to a specific sports discipline. This can be done, for example, by separately process the video with OpenPose, as well as with a custom-trained DeepLabCut model. Resulting .trc coordinate files can be merged, and used in OpenSim. However, the DeepLabCut keypoints must be referenced on an OpenSim model, which may need to be crafted from scratch, such as a ball, skis, or bike, depending on the detected object.

3.4.2 Multi-person analysis

Pose2Sim has several limitations. First, despite it is not altered by people entering the field of view, it can currently only analyze the movement of one single person. For races, team sports, and combat sports, it would be useful to be able to analyze the movement of several athletes at the same time. This could be achieved in two steps: first, by triangulating all the persons whose reprojection error is below a certain threshold, instead of taking only the one with minimum error, in a similar way as carried out by [Slembrouck2020]; then, by tracking the triangulated persons in

time, e.g., by limiting the displacement speed of each person's neck keypoint from one frame to the next one. Another way would be to use a spatio-temporal neural network, which would take advantage of the information gathered in previous frames instead of working frame-by-frame [?]

3.4.3 User-friendly calibration

Calibration remains a challenging task in daylight, at a distance, and with non research-grade cameras. It could be useful to make it more robust, either by implementing the Aniposelib library [Karashchuk2020], by importing calibration files from an Argus wand calibration [Argus2020], or by automatically calibrating on people's limb length [Liu2022a]. Along with synchronization of light-weight cameras, this topic will be detailed in Chapter 6 on [Application to boxing, using action cameras](#) [Pagnon2022c].

3.4.4 Visualization tools

Pose2Sim does not provide a GUI yet. This can make it complicated for coaches to adopt the tool. However, the code has been adopted by other entities. A 3D animation add-on engineer built a Blender [Blender1998] extension using Pose2Sim for realistic 3D markerless animation. However, it is not free nor open-source [Barreto2022] (Figure 3.9). In addition, the CAMERA laboratory of the University of Bath is currently developing a GUI around Pose2Sim, which would make the tool more accessible.

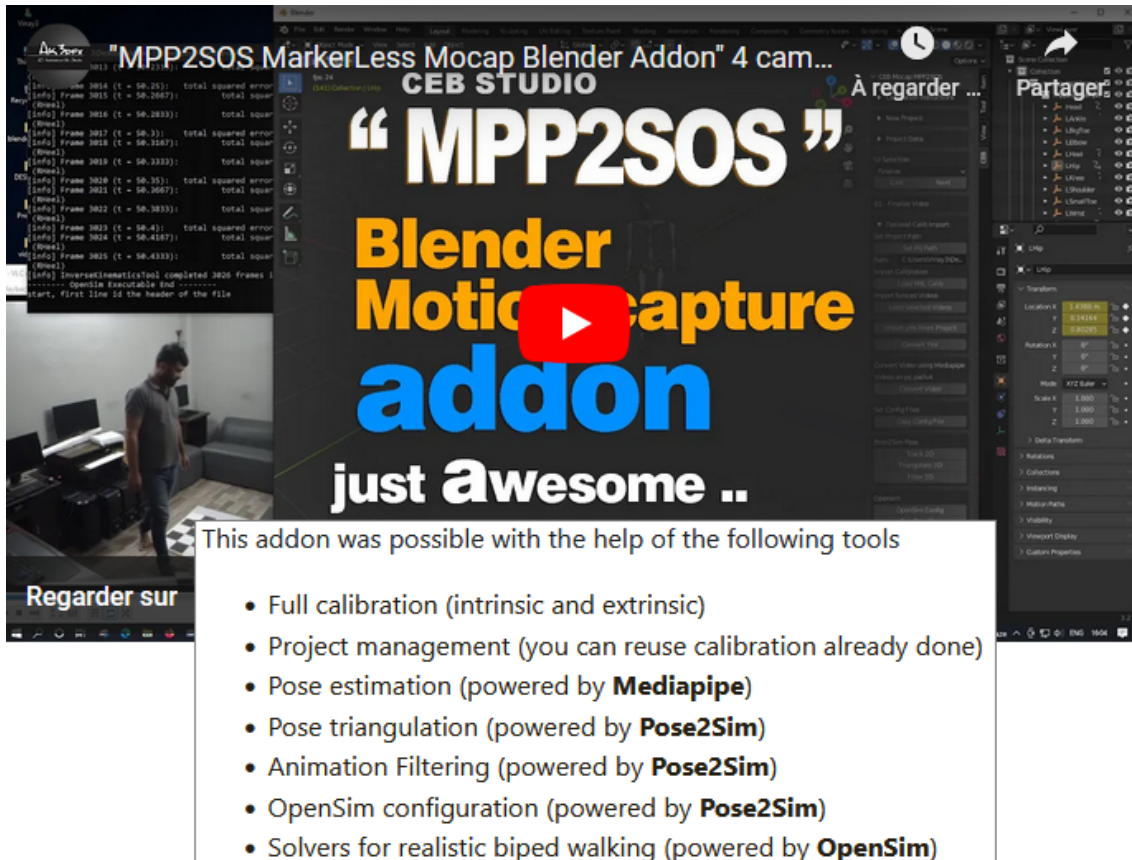
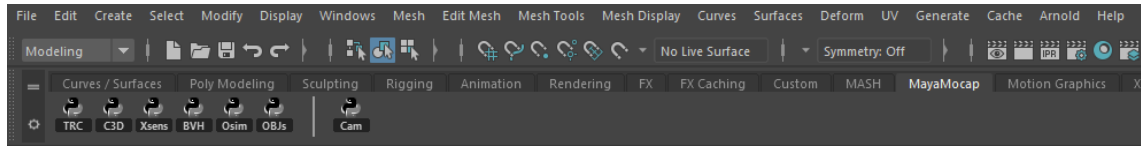
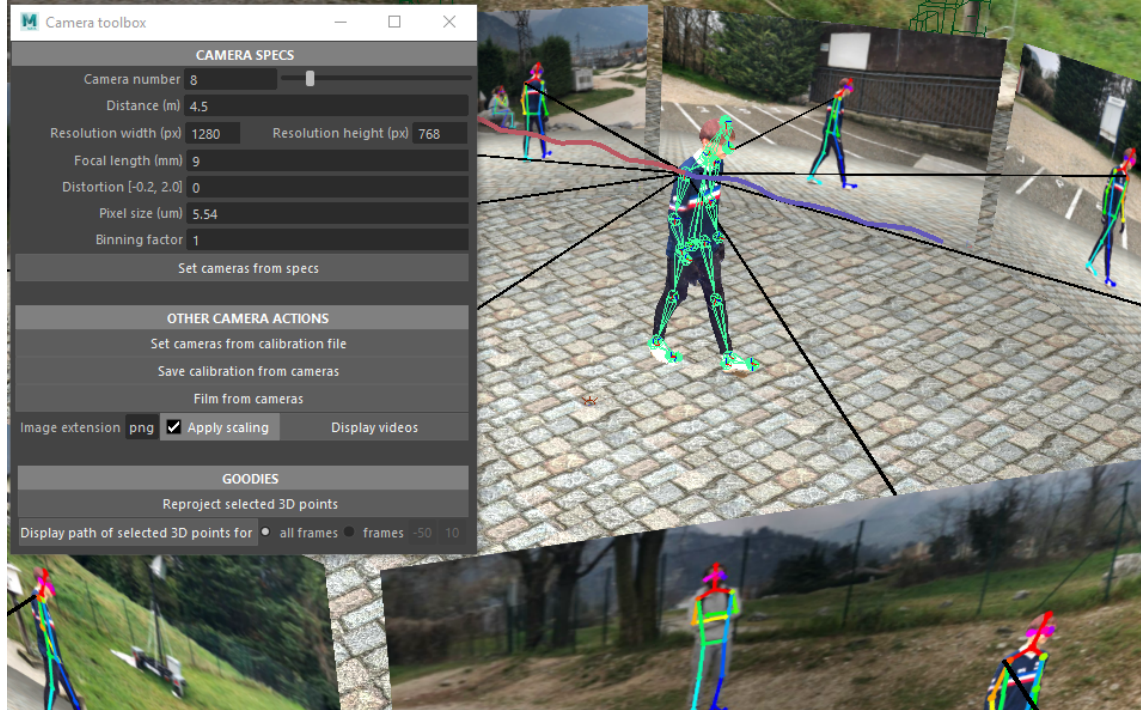


Figure 3.9: The MPP2SOS Blender add-on uses Pose2Sim for realistic 3D markerless animation

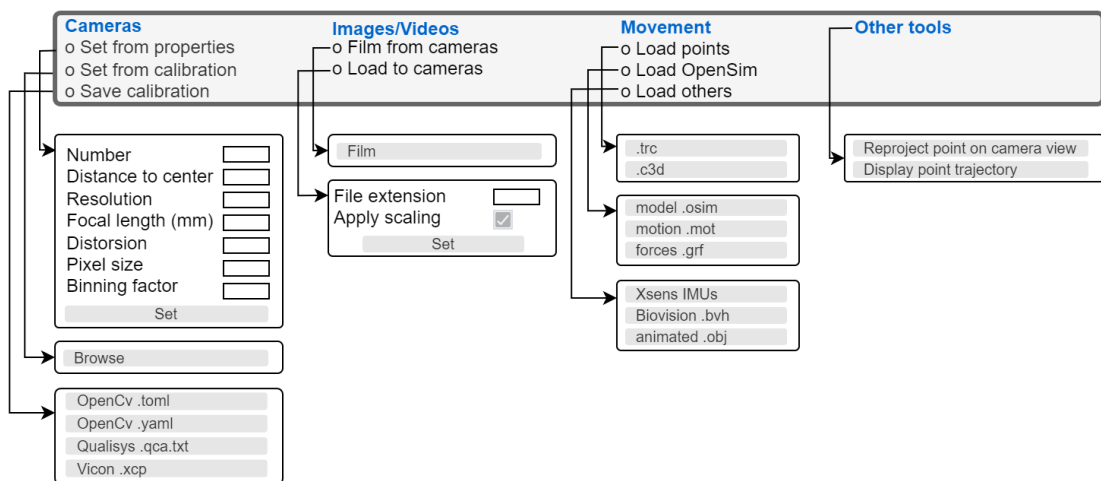
I also developed a toolbox for Maya [Maya1998] called Maya Mocap [Pagnon2020]. First, it can import and display various types of motion files. Then, it can load cameras from a calibration file, film with them, and import the filmed image sequences. It can also help to make sure that



(a) The Maya-Mocap add-on is displayed as an additional toolbar in Maya.



(b) Maya-Mocap can import several file types, e.g., a .trc motion file (bright green) or a textured animated 3D mesh. It can also load cameras from a calibration file, film with them, and display the filmed image sequences. In addition, it can reproject a selected point onto the camera plane (black lines), to make sure that it has been correctly triangulated. The 3D trajectory of a point can also be highlighted (red and blue lines).



(c) The organigram of Maya-Mocap planned abilities.

Figure 3.10: The Maya-Mocap add-on (a-b), and the tool set that it should eventually provide (c).

triangulated points are well reprojected on the camera plane, by tracing a line from the point to the camera center. In addition, it can display the 3D trajectory of a point (see Figure 3.10). Next objectives would be to make it able to import an OpenSim model and its motion files, and to present it as a cleaner package, ready to be released. Since all the tools used in Pose2Sim are open-source, it would also be more consistent to translate it into Blender instead of Maya, in order to offer an entirely operational and open-source tool.

3.4.5 Real-time analysis

Currently, Pose2Sim does not work in real time. This is a drawback for coaches and athletes, who need feedback in a timely manner. However, a timely analysis of athletes' movements directly on the sports field appears to be achievable. Indeed, OpenPose is faster than most of its competitors [Chen2020], and the rest of the process is not computationally costly. Moreover, the pose detection, the triangulation, and the OpenSim inverse kinematic optimization work frame by frame. As a consequence, it is conceivable to calibrate and scale the model first, and then to feed the GUI frame by frame. This would allow the system to work only with a few seconds of delay.

3.4.6 Other perspectives

Other minor adjustments could be made in order to improve the triangulation and the filtering steps. Implementing Random Simple Consensus (RANSAC) triangulation [Fischler1981] as an alternative to our weighted Direct Linear Transform (DLT) [Pagnon2021], and opting for optimal fixed-interval Kalman smoothing instead of low-pass filtering [Rauch1965, Needham2021a], may reduce errors, especially in large outliers.

4

Robustness assessment

A markerless motion capture method is satisfying if it is accurate, fast, and robust. Robustness is deemed good when results are unchanged while adding constraints on the subject or on the environment. We challenge our workflow on walking, running, and cycling tasks, by adding people in the background, and by simulating challenging conditions: (Im) alters image quality (11-pixel Gaussian blur and 0.5 gamma compression); (4c) uses fewer cameras (4 vs. 8) which leads to unsolved occlusions; and (Cal) introduces calibration errors (1 cm vs. perfect calibration).

When averaged over all joint angles, stride-to-stride standard deviations lay between 1.7° and 3.2° for all conditions and tasks, and mean absolute errors (compared to the reference condition—Ref) ranged between 0.35° and 1.6° . For walking, errors in the sagittal plane were: 1.5° , 0.90° , 0.19° for (Im), (4c), and (Cal), respectively. As a consequence, Pose2Sim is robust enough for the 3D joint angle analysis of walking, running, and cycling, under challenging conditions.

This chapter is adapted from the article published in the Sensors: "Pose2Sim: An End-to-End Workflow for 3D Markerless Sports Kinematics—Part 1: Robustness" [Pagnon2021].

Contents

4.1	Introduction	47
4.1.1	Robustness definition	47
4.1.2	Assessing robustness	48
4.2	Methods	48
4.2.1	Experimental setup	48
4.2.2	Participant and protocol	50
4.2.3	Challenging robustness	51
4.2.4	Markerless kinematics	51
4.2.5	Statistical analysis	53
4.3	Results	54
4.3.1	Data collection and 2D pose estimation	54
4.3.2	Pose2Sim tracking, triangulation, and filtering	54
4.3.3	OpenSim scaling and inverse kinematics	55
4.3.4	Relevance, repeatability and robustness of angles Results	56
4.4	Discussion	60
4.4.1	Pose2Sim	60
4.4.2	Relevance, repeatability and robustness	61
4.4.3	Limits and perspectives	62

4.1 Introduction

4.1.1 Robustness definition

According to the review of [Desmarais2021], the performance of a method can be ranked regarding its accuracy, speed, or robustness. Accuracy is mostly assessed with MPJPE (Mean Per Joint Position Error); speed is evaluated either regarding computing complexity, or framerate when possible; and robustness is gauged through differences in the results while changing the system parameters only. [Desmarais2021] points out that authors usually only consider accuracy, sometimes speed, but rarely robustness. However, robustness is of paramount importance in the context of sports, especially "in the wild". This chapter will focus on robustness, the next one on [Accuracy assessment](#), and we will not focus on speed in this thesis (although chapter 3.4.5 broaches [Real time considerations](#)).

[Moeslund2001] proposed to express robustness as the number of constraints on the subject or on the environment required for a motion capture system to be operational. Some of the assumptions they proposed have already been universally overcome by deep-learning-based methods. For example, no markers are involved anymore, the subject can wear their usual clothes (including loose pants or dresses [Viswakumar2019]), and the background does not need to be static or uniform. Some other items remain an open problem.

For instance, most 3D methods assume that only one person lies in the camera field of view. This is a strong assumption, especially outdoors where people and athletes pass by and an operator is often present. Although it is starting to be addressed, standard solutions are yet to be determined [Slembrouck2020, Bridgeman2019, Chu2021, Dong2019].

Other open questions lie in the environment, much less controlled in a sports context than in a lab, which can result in bad image qualities. [Viswakumar2019] experienced that OpenPose is very robust to extreme lightning conditions. However, research has shown that pose estimations models are more robust to noise or brightness changes, while less robust to motion or to defocus blur [Wang2021a]. And yet, in sports, the movement is not usually slow, continuous, nor limited to the sagittal plane.

Occlusions are, for the most part, solved by using a network of calibrated cameras. Since triangulation is computed using a least square method, a large amount of cameras will also blunt imprecision on the 2D joint estimations. [Bala2020] showed that once correctly trained for 3D macaque pose estimation, eight cameras were enough to correctly infer 80% of the 13 considered keypoints, while four cameras decreased the performance to about 50%. However, a correct estimation of extremities such as feet and hands required more than eight cameras.

Camera calibration can be challenging outside, due to large volume spaces, bright light, and contrasting shades. As a consequence, it is close to impossible with the classic approach based on predefined objects with markers. Moreover, simple calibration with a checkerboard may cause errors on intrinsic and extrinsic camera parameters estimation [Sun2005]. A calibration is generally considered acceptable if the average residuals of each camera (i.e., the root mean square error of the reprojection of the 3D reconstructed coordinates on the 2D image plane) is below 1 pixel. In metric terms, the markers-based Qualisys Track Manager software recommends redoing a calibration when the average residuals exceed 3 millimeters [Qualisys2018]. The pinhole camera model gives an equivalence between pixel values on the image plane, and metric values on the object plane at the center of the scene, as demonstrated by Figure 4.1 and Equation 4.1. See Chapter 2.2.1 on [Pinhole camera model](#) or [Dawson-Howe1994] for in-depth explanations.

$$Err^{Img} = \frac{f \times Err^{Obj}}{D} \quad (4.1)$$

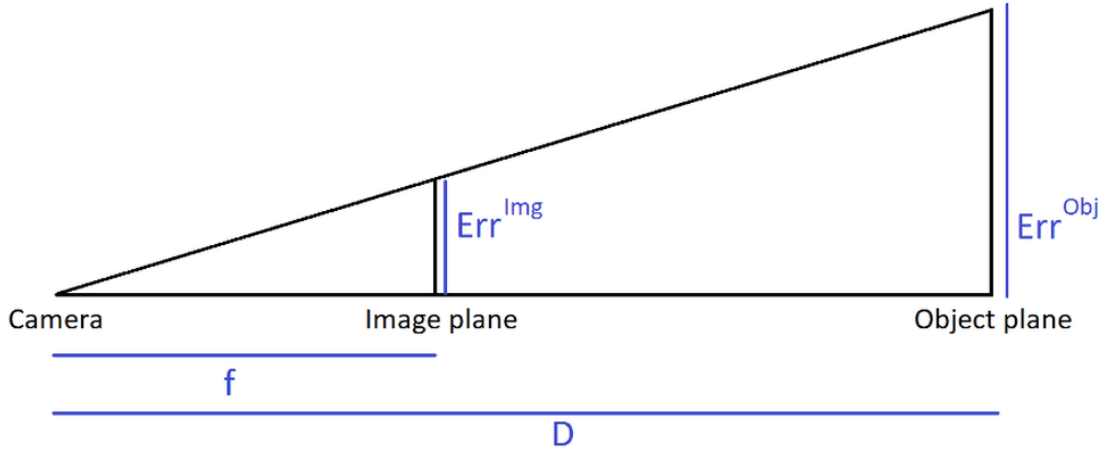


Figure 4.1: The pinhole camera model permits a correspondence between image coordinates and object coordinates. f : focal distance, D : object to camera distance, Err^{Img} : error on image plane, Err^{Obj} : error on object plane. f and Err^{Img} are usually expressed in pixels, while D and Err^{Obj} are expressed in meters.

4.1.2 Assessing robustness

Because [Needham2021a] showed that the quality of markerless results were task specific, we will examine walking, running, and cycling. Before assessing the robustness of the workflow, the relevance of the computed 3D full-body angles needs to be estimated. This will be done by comparing our angle results to those of a normative walking database. Further concurrent validation of the accuracy will be determined in the next chapter on [Accuracy assessment](#). Repeatability will be evaluated by comparing movement cycles to each other, within each task and each capture condition.

Robustness itself will be assessed through all three types of movements, in accordance with the open problems previously described:

1. In addition to the person of interest, some people will be present in the background.
2. Image quality will be altered, by simulating a dark scene captured with defocused cameras objectives.
3. Occlusions will become more challenging as we decrease the number of cameras. Moreover, cycling sequences will lead to more occlusions than walking or running ones.
4. Calibration errors will be introduced by corrupting the calibration files.

The underlying idea presented in this article is to verify whether modifying external environment parameters significantly impacts variability in joint angle estimation.

4.2 Methods

See [video here](#) for a visual description of the protocol.

4.2.1 Experimental setup

To guarantee a tight control of the environment parameters, we captured our data in a dedicated studio platform called Kinovis [Tsiminaki2014], from which we were able to create realistic virtual views similar to outdoor video. This platform is a $10m \times 10m \times 5.6m$ green room equipped with 68 video cameras recording at 30 fps in 4 Mpixels resolution, for a practical acquisition

space of about $5m \times 5m \times 3m$. The system computes 3D textured meshes by convex visual hull reconstruction [Laurentini1994]. The meshes were inserted in a virtual environment composed of an environment texture map captured from a BMX racetrack, and a custom-made virtual floor. It should be noted that three people were present in the background, which introduced a realistic artifact of multiple subjects.

We developed a script for Autodesk Maya [Maya1998] (see [Visualization tools](#)) that allows us to render the textured mesh files, as well as to virtually set any cameras with specific properties (position, orientation, resolution, focal length, distortion, pixel size, binning factor). Views seen through virtual cameras can be saved as video files and visualized into a global 3D environment (Figure 4.2). The generated video files were used as input to the 3D kinematics pipeline.



Figure 4.2: The Kinovis room allows for the capture of 3D textured meshes. These meshes are placed in a virtual environment, and then filmed from virtual cameras.

For the purpose of this study, we created 8 virtual video cameras. Resolution was set to 1280×768 pixels, focal length to 9 mm, pixel size to $5.54 \mu\text{m}$, and no distortion nor binning was introduced. Binning refers to the process of grouping pixels in order to increase sensitivity to light, at the expense of decreasing resolution. Cameras were regularly distributed 8 m away from the center of the captured volume, at a height of 1 m, so that the whole body could be detected for a maximum of movement cycles. We then rendered the scene as video files from our virtual cameras

and saved the exact calibration parameters. We applied a 3×3 pixel Gaussian blur afterwards to reduce sharp edges of the virtual scene compositing (Figure 4.3). This resulting image quality was considered as “standard”.



Figure 4.3: To smooth out sharp edges due to compositing, we applied a 3×3 pixel Gaussian blur to the videos filmed from our virtual scene.

4.2.2 Participant and protocol

One healthy adult male subject (1.89 m, 69 kg) participated in the study. He provided his informed written consent prior to participating. The study was conducted in accordance with the Declaration of Helsinki [Holm2013]. No requirement was given to him regarding his outfit. He was asked to perform three basic sports tasks: walking, running, and cycling. For all three tasks, the subject was given a moment beforehand to warm up and find a comfortable and regular pace, which he could then follow owing to the sound of a metronome:

- **Walking:** The subject walked in a straight line back and forth over the 10 m diagonal of the room. His body mesh could be fully reconstructed only in the central 5 m of the acquisition space, i.e., only roughly 2 gait cycles were acquired per walking line. His comfortable stride pace was 100 BPM (Beats per Minute). The stride length was not monitored.
- **Running:** The subject jogged in a straight line back and forth along the 10m diagonal of the

room. His comfortable stride pace was 150 BPM (Beats per Minute). The stride length was not monitored.

- *Cycling*: The subject cycled on a road bike placed on a home trainer. He himself adjusted the resistance and the height of the saddle prior to the capture. His comfortable cadence was 60 BPM.

As obtaining the textured meshes of the subject in the green Kinovis room involved filming simultaneously with 68 4 Mpixels cameras that generated a flow of over 8 gigabytes per second, the capture design limited the acquisition time to 45 s.

4.2.3 Challenging robustness

We challenged robustness with 3 challenging conditions, compared to a reference one.

- *Reference Condition (Ref)*: The reference condition under which our 3D markerless kinematic system had to operate took advantage of the standard image quality, 8 available virtual cameras, and a perfect calibration. The standard quality corresponded to the unaltered images of the 3D scene filmed from our virtual cameras. The reference condition involved 8 virtual cameras, as a good compromise of what is feasible in real outdoor conditions. Moreover, a study on macaques showed that 8 cameras were enough to correctly infer 80% of the 13 considered keypoints [Bala2020]. The calibration could be considered perfect, since the virtual cameras were explicitly specified in the virtual environment.
- *Poor Image Quality (Im)*: Video quality was made blurrier and darker: a Gaussian blur (11 × 11px) was applied, as well as a 0.5 gamma compression (Figure 4.4). This simulated a dark scene captured with defocused camera objectives.
- *Less Cameras (4c)*: The 2D joint coordinates were triangulated with only 4 cameras, instead of 8 in the reference condition: one on each side, one in the front, and one in the back, set 90° apart from each other.
- *Calibration Errors (Cal)*: Calibration residuals are classically supposed to be under 1 px on the image plane or under 3 mm on the object plane. Using Equation 4.1 demonstrates that in our case 3 mm corresponds to 0.61 px. We chose to simulate a calibration error of 2 px, which corresponds to about 1 cm (Equation 4.2).

$$Err_{Obj} = \frac{Err^{Img} \times D}{f} = \frac{2 \times 8}{\frac{9 \times 10^{-3}}{5.54 \times 10^{-6}}} = 9.8 \times 10^{-3} m \quad (4.2)$$

The calibration error was simulated by translating the extrinsic parameters of each camera in a random direction. The norm was randomly picked in a normal distribution of mean 2 px and a standard deviation of 1 px. The mean of these 8 translations was ensured to be equal to 210^{-3} px.

4.2.4 Markerless kinematics

Then, we used Pose2Sim to robustly triangulate OpenPose outputs and feed the resulting 3D joint coordinates to OpenSim. The exact same parameters were used for all 4 conditions and all 3 movement tasks, in order to make sure the process did not induce any supplementary deviation to the compared results.

2D pose estimation

We applied OpenPose (version 1.6) on all the captured videos. We used the experimental body_25b model (see Figure 3.7) with highest accuracy parameters, which is more accurate than the default body_25 one and reduces the number of false positives [Hidalgo2019].



Figure 4.4: The image under poor image quality (Im) conditions. A Gaussian blur ($11 \times 11px$) was applied, and a 0.5 gamma compression made the image darker.

Tracking, triangulation, and filtering

We used the Tracking function of Pose2Sim to try out every possible triangulation of the neck keypoint of all detected persons. The person with the smallest reprojection error was deemed to be the one to be tracked. If the reprojection error was above 10 pixels, one camera was removed and the process was repeated. See [Tracking the person of interest](#) Chapter 3 for more details.

The weighted DLT provided by the Triangulation function of Pose2Sim was employed. Some keypoints were sometimes occluded to some cameras, either by the subject himself, by his cycling gear, or simply because the subject left the camera field of view. In such a case, OpenPose usually gave a low (or zero) confidence to the estimated point, which was dealt with by setting a confidence threshold above which the camera in question was not used for the triangulation. However, OpenPose occasionally wrongly detected the occluded keypoint with a relatively high confidence. Under such circumstances, the point was erroneously triangulated. This issue was spotted and solved by reprojecting the 3D point on the camera planes. If the reprojection error between the reprojected points and the OpenPose detection was higher than a predefined threshold, the process was repeated after removing one, or several, cameras. If less than 3 cameras remained, the frame was dropped for this point, and missing frames were later interpolated with a cubic spline. 3D joints positions were then exported as an OpenSim compatible .trc file. We chose a confidence threshold of 0.3 and a reprojection error threshold of 10 px.

3D coordinates were finally filtered with a Butterworth filter [[Butterworth1930](#)]. We chose a zero-lag fourth order low-pass Butterworth filter, with a 6 Hz cutoff frequency.

Gait events determination

Cycles were determined using one of the methods given by [[Zeni2008](#)] for the determination of gait events using kinematic data. Zeni et al. suggested defining heel strike as the time of

maximum distance between the heel and the sacrum. Here, the sacrum marker was assimilated to the ipsilateral hip joint coordinate. Although there is no heel strike in cycling, we used the same definition as a reference for the start of a cycle. An implementation of the algorithm is provided in the Pose2Sim repository. A cycle was defined as starting from heel strike, with a duration t_{cycle} :

$$t_{cycle} = \frac{2}{cadence/60} \text{seconds} \quad (4.3)$$

The duration of a cycle t_{cycle} was 1.2 s for walking, 0.8 s for running, and 1.0 s for cycling. The reduced area of acquisition and the limit of 45 s of capture restricted the analysis to 8, 9, and 15 cycles for walking, running, and cycling, respectively.

Kinematic analysis

The full-body musculo-skeletal model proposed by [Rajagopal2016] was adjusted to our needs. OpenPose model markers were carefully placed on the body, as closely as possible to their average triangulated 3D coordinates. Muscles were removed since they were not considered at that stage. A ball joint was added between head and torso so that the rotation of the head could be roughly rendered. Pelvis translation and subtalar angle rotation were unlocked. Lumbar extension and lumbar bending were clamped between -15° and 15° , and constraints on hip flexion/extension ranges of motion were released since they were too strict for our cycling task. This model uses a coupling relationship between knee flexion and the other planes of movement, which allows for 3D knee kinematics with only one degree of freedom. *Note that the model was later improved when assessing the accuracy of the workflow.*

See previous chapter on [Proposed solution: Pose2Sim Python package](#) for more details on the scaling and inverse kinematics procedures. We visually verified at the end of the inverse kinematic step that model markers approximately overlaid experimental markers (Figure 4.5), and we batched inverse kinematics for all gait cycles with the command line utilities. We then concatenated all results in a .csv file analyzed them using python.

4.2.5 Statistical analysis

As similar results were expected for both sides, as more strides were captured on the left one, and for the sake of clarity, the analysis was performed on the left side only. Descriptive statistics were calculated at the triangulation stage, for each (Ref), (Im), (4c), and (Cal) condition. We calculated mean, standard deviation (std), and maximum (max) number of cameras excluded for performing triangulation. Triangulation was deemed acceptable in Pose2Sim when OpenPose confidence was above 0.3, and when reprojection error was below 10 pixels. We also calculated mean, std, and max reprojection errors. Descriptive statistics of the OpenSim scaling and inverse kinematics steps were also rendered: we retrieved mean, std, and max root-mean-square error (RMSE) of the experimental and model markers.

Next, we investigated the relevance of our results. The angles of the Ref condition on the walking task were compared to those of a normative walking gait database [Fukuchi2018], from which we took a subset of 14 young and healthy males walking at a "comfortable" speed (Norm). Pearson's correlations (r) and mean absolute error (MAE) were calculated. As the angle definition was different from that in the OpenSim model [Trinler2019], only the flexion/extension angles were compared.

Repeatability was estimated by computing stride-to-stride standard deviations within (Ref), (Im), (4c), and (Cal) conditions. These stride-to-stride variability results were then compared to [Kang2008], obtained with a marker-based approach and averaged over 18 young adults. The robustness of the workflow was assessed by calculating the standard deviation ratio between each

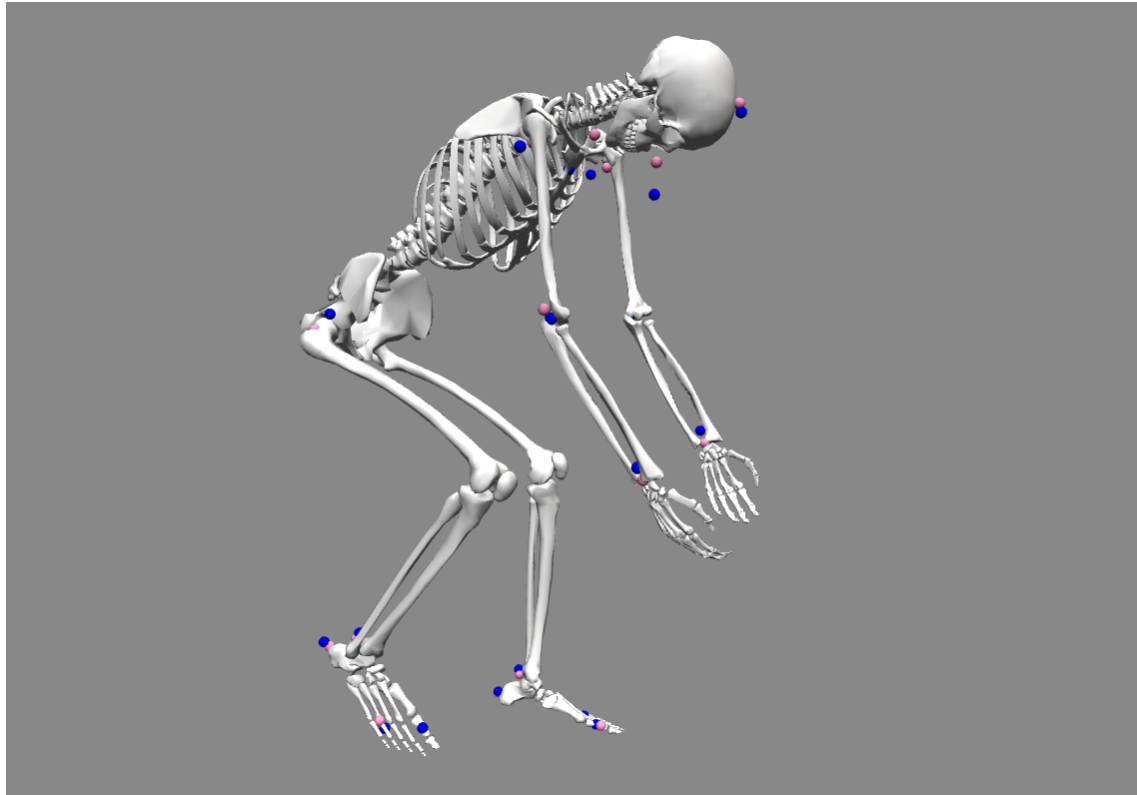


Figure 4.5: OpenSim inverse kinematics on cycling (C). Model markers are pink; experimental markers are blue.

degraded condition and the Ref one, as well as the r coefficient and the MAE. Statistical parametric analysis (SPM-1D) was lastly performed between Ref and degraded conditions to convey statistical differences along time (See [[Warmenhoven2018](#)]).

4.3 Results

4.3.1 Data collection and 2D pose estimation

Each trial took several hours to process on a cluster of high-end computation units. Then, filming the resulting 3D meshes in a virtual scene with virtual cameras also took a few hours per sequence, as well as about 50 Go of storage space. Although all of this allowed us to perfectly control the parameters of the capture, this step would not be carried out in the wild, where capture would simply be carried out by filming with calibrated cameras.

Apart from the capture design, which is very particular to this study, the OpenPose 2D pose estimation was the most computationally costly step. On a standard computer with an Nvidia GeForce GTX 1080 graphic card (8 Go memory), the detection for each camera ran at a little over 0.5 fps (i.e., 0.07 fps for 8 cameras).

4.3.2 Pose2Sim tracking, triangulation, and filtering

On our standard computer, tracking was performed at an average of 5 fps depending on the number of undesired persons present in the background; triangulation was at about 10 fps; and filtering was almost instantaneous in comparison.

Depending on the considered frame, the reprojection error of a joint coordinate sometimes

exceeded the prescribed threshold. In this case, the triangulation process was executed another time after excluding the 2D joint coordinates estimated from one, or several, cameras. Over all frames, an average of approximately 0.5 cameras were excluded in walking and in running and 1.6 in cycling (Table 4.1). The mean of the reprojection error was about 3.5 px (≈ 1.6 cm) in walking and running and 6 px (≈ 3 cm) in cycling. More cameras had to be excluded for the nose and for the extremities such as wrists and toes, and the reprojection error was mostly large on hips, head, and extremities.

Task	Conditions	Mean number of excluded cameras			Mean absolute reprojection error		
		mean	std	max	mean	std	max
Walking	Ref	0.47	0.57	2.0 (Nose)	3.3 px (1.6 cm)	1.1 px (0.54 cm)	5.3 px (2.6 cm, LHip)
	Im	0.91	0.8	2.4 (LWrist)	3.7 px (1.8 cm)	1.0 px (0.52 cm)	5.2 px (2.6 cm, LSmallToe)
	4c	0.27	0.34	1.0 (Nose)	2.9 px (1.4 cm)	0.93 px (0.47 cm)	4.5 px (2.2 cm, LSmallToe)
	Cal	0.47	0.57	2.0 (Nose)	5.1 px (2.5 cm)	0.91 px (0.45 cm)	6.9 px (3.4 cm, LHip)
Running	Ref	0.48	0.64	2.2 (LWrist)	3.5 px (1.7 cm)	1.2 px (0.57 cm)	5.6 px (2.8 cm, LWrist)
	Im	0.94	1.2	4.5 (LWrist)	4.0 px (2.0 cm)	1.4 px (0.69 cm)	7.2 px (3.6 cm, RWrist)
	4c	0.22	0.31	1.0 (LWrist)	3.3 px (1.6 cm)	0.97 px (0.48 cm)	4.7 px (2.3 cm, LWrist)
	Cal	0.47	0.65	2.2 (LWrist)	5.4 px (2.7 cm)	1.0 px (0.52 cm)	7.2 px (3.6 cm, LWrist)
Cycling	Ref	1.62	1.4	4.2 (RBigToe)	6.1 px (3.0 cm)	1.2 px (0.58 cm)	8.5 px (4.2 cm, Head)
	Im	2.41	1.9	5.7 (RBigToe)	6.3 px (3.1 cm)	1.3 px (0.60 cm)	8.5 px (4.2 cm, Head)
	4c	0.76	0.67	2.1 (RBigToe)	5.3 px (2.6 cm)	1.6 px (0.82 cm)	8.4 px (4.2 cm, LElbow)
	Cal	1.68	1.4	4.24 (RBigToe)	6.9 px (3.4 cm)	1.0 px (0.51 cm)	8.9 px (4.4 cm, Head)

Table 4.1: Descriptive statistics on the triangulation step performed by Pose2Sim from OpenPose body_25b model. Mean absolute reprojection error and mean number of excluded cameras were calculated over time. Mean (mean), standard deviation (std), and maximum (max) in each of these variables are displayed. Walking, running, and cycling tasks were investigated in each four conditions: reference (Ref), poor image quality (Im), four cameras instead of eight (4c), and calibration errors (Cal).

Within each task, almost twice as many cameras had to be excluded in the (Im) condition as in the (Ref) condition, with nearly one camera excluded in walking and running, and nearly 2.5 in cycling. However, the reprojection error was increased by only about 10%. About twice as few cameras had to be excluded in the (4c) condition as in (Ref) condition, and the reprojection error was decreased by about 10%. The (Cal) condition did not involve more excluded cameras; indeed, calibration errors had no effect on the OpenPose confidence, and reprojection error stayed within the threshold of 10 px. However, a 2 px average error in calibration logically resulted in about a 2 px (≈ 1 cm) larger reprojection error than in the Ref condition.

4.3.3 OpenSim scaling and inverse kinematics

Scaling took a few hours, which is in line with the usual expectations in marker-based methods. However, markers would be positioned in the same place by the pose estimation algorithm regardless of the subject and of the operator: as a consequence, in the future, only bones would have to be scaled, and markers will not have to be further adjusted. Due to the small number of markers whose positions had to be optimized, Opensim's inverse kinematics ran at more than 0.5 fps.

OpenSim recommends the RMS of experimental vs. model marker errors to be below 1 cm for scaling. Our best average RMS error was 1.9 cm. During inverse kinematics, it is recommended

for it to stay below 2–4 cm. The average RMS error was typically below 4 cm, but it could reach much more for some markers at certain phases of the cycle, especially in the cycling task. Within each task, changing conditions made very little difference in RMS marker errors, including in mean, standard deviation (std), or maximum error (Table 4.2).

Task	Condition	RMS marker error		
		mean	std	max
Walking	Ref	2.8 cm	0.13 cm	3.2 cm (Mid stance)
	Im	2.8 cm	0.11 cm	3.1 cm (Mid stance)
	4c	2.8 cm	0.12 cm	3.2 cm (Mid stance)
	Cal	2.9 cm	0.13 cm	3.2 cm (Mid stance)
Running	Ref	2.2 cm	0.22 cm	2.6 cm (Mid stance)
	Im	2.4 cm	0.21 cm	2.8 cm (Mid stance)
	4c	2.5 cm	0.30 cm	2.4 cm (Mid stance)
	Cal	2.2 cm	0.21 cm	2.6 cm (Mid stance)
Cycling	Ref	3.4 cm	0.11 cm	3.6 cm (Dead center)
	Im	3.8 cm	0.18 cm	4.2 cm (Dead center)
	4c	3.9 cm	0.60 cm	5.9 cm (Dead center)
	Cal	3.4 cm	0.11 cm	3.6 cm (Dead center)

Table 4.2: Descriptive statistics on the inverse kinematics step performed by OpenSim with a full body model adapted from Rajagopal’s. Root mean square (RMS) errors between experimental and model markers were calculated over all markers. Mean, standard deviation (std), and maximum (max) are displayed. Dead center refers to the phase where the crank is near the vertical position.

Note that one should not compare the values of the reprojection errors in the triangulation step, and of the marker errors in the inverse kinematics one. Primarily, the first one is calculated over time, while the second one is calculated over markers. Additionally, the first one is a mean absolute error (MAE), while the second one is a root mean square error (RMSE). RMSE squares the errors, which always makes it larger than the MAE. It penalizes large errors more, which has some implications that are not addressed here but are documented in [Chai2014]. These errors should only be used to compare conditions within each step.

4.3.4 Relevance, repeatability and robustness of angles Results

Flexion/extension lower-limb angles were compared to a normative walking gait database [Trinler2019] (Figure 4.6). Ankle movement differed noticeably ($r = 0.35$, $MAE = 5.4^\circ$), especially between 40% and 70% of the gait cycle. There was a good agreement for the knee ($r = 0.93$, $MAE = 5.7^\circ$) and hip angles ($r = 0.97$, $MAE = 9.0^\circ$) despite some notable offset in hip angle. A similar shift occurred in the pelvis ante/retroversion angle (not further analyzed).

When averaged over all joint angles, the stride-to-stride standard deviations lay between 1.7° and 3.2° for all conditions and tasks (Table 3). The walking task was the most variable, while the cycling one was the least variable; however, in the latter the upper body was static and artificially drew the mean down, which was revealed after removing it from the statistics (Table 4.3). In the walking task, the stride-to-stride standard deviation of our individual lower body angles was higher than [Kang2008], who used a marker-based approach (Table 4.4).

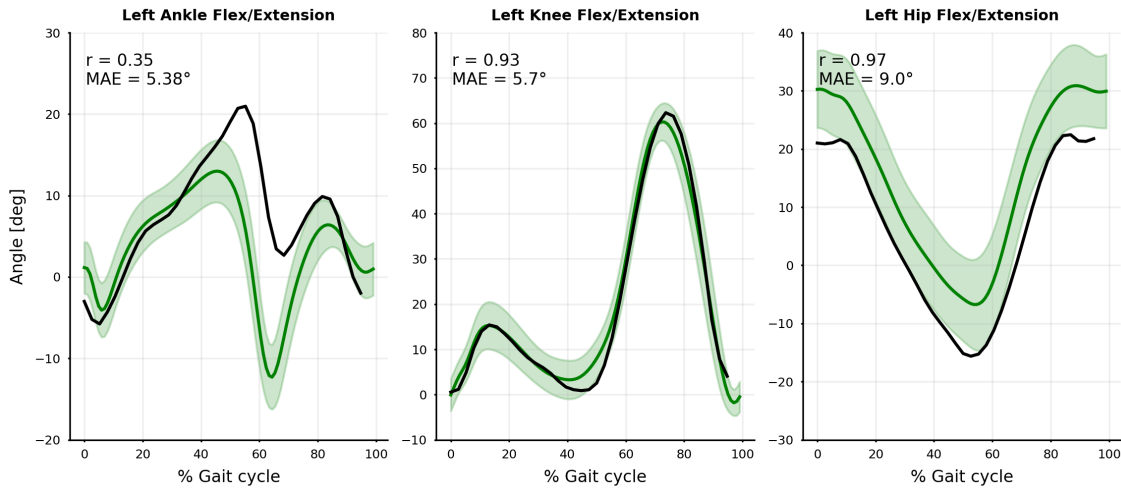


Figure 4.6: Comparison between our markerless results (black line: mean stride-to-stride results for our subject) and the normative marker-based database (green line and area: mean and standard deviation across 14 young, healthy, male subjects). Mean absolute error (MAE) and Pearson correlation coefficient (r) are represented.

Task	Condition	std (°)	std/stdref	r	MAE (°)
Walking	Ref	2.56	-	-	-
	Im	3.03	1.19	0.97	1.55
	4c	3.24	1.27	0.97	1.50
	Cal	2.60	1.02	1.00	0.35
Running	Ref	2.59	-	-	-
	Im	2.76	1.07	0.99	0.92
	4c	2.79	1.10	0.97	1.60
	Cal	2.54	0.98	1.00	0.47
Cycling	Ref	1.78	-	-	-
	Im	1.89	1.08	0.88	1.72
	4c	3.04	1.93	0.81	1.54
	Cal	1.80	1.02	0.99	0.50
Cycling (lower-body only)	Ref	2.09	-	-	-
	Im	2.41	1.22	0.94	1.69
	4c	3.82	2.31	0.90	1.84
	Cal	2.13	1.03	0.99	0.51

Table 4.3: Summary of angles statistics, averaged for all joints. Each condition is represented: reference condition (Ref), degraded image quality (Im), four cameras instead of eight (4c), degraded calibration (Cal). Comparisons between each Im, 4c, Cal conditions, and Ref are accounted for with standard deviation (std), the standard deviation ratio (std/stdref), the Pearson's correlation coefficient (r), and the mean absolute error (MAE).

Joint	Method	Flexion/Extension	Abduction/Adduction*	Internal/External rotation
Ankle	[Kang2008]	2	2.5	-
	Ours	2.07	4.84	-
Knee	[Kang2008]	0.7	-	-
	Ours	4.85	-	-
Hip	[Kang2008]	1.2	1.8	1.1
	Ours	2.61	1.5	3.72

Table 4.4: Stride-to-stride standard deviations of lower-body angles. Comparison between our markerless approach, and a marker-based one (averaged over 18 young subjects). * Ankle subtalar angle is assimilated to an abduction/adduction angle.

There was a good agreement between the Ref condition and the degraded ones, at the same time across all tasks, movement planes, and joints. Mean absolute errors (MAE) averaged over all joint angles (compared to the reference condition—Ref) ranged between 0.35° and 1.7° for all conditions and tasks (Table 4.3). Individual angle MAE lay between 0.07° and 5.2° (Figure 4.7 for the walking task, and Figure A.1 and Figure A.2 in the Appendix for the running and cycling tasks). However, the cycling task was more challenging: ankle joint angles were especially less robust regarding all considered dependent variables.

Angle results were particularly little affected by the 1 cm calibration error (Cal condition). The standard deviation between cycles (std) virtually did not increase, the average Pearson's r correlation coefficient was 1.00 in all tasks but the cycling one ($r = 0.98$), and the mean absolute angle error stayed below 0.5° (Table 4.3).

The standard deviation in Im and 4c conditions increased by about 10 to 30% as compared to Ref condition, apart from the cycling 4c condition where it increased by 100%. The Pearson's r correlation coefficient was about 0.98 in all tasks but the cycling one. Mean absolute angle errors across all joints lay between 0.9 and 1.8° (Table 4.3).

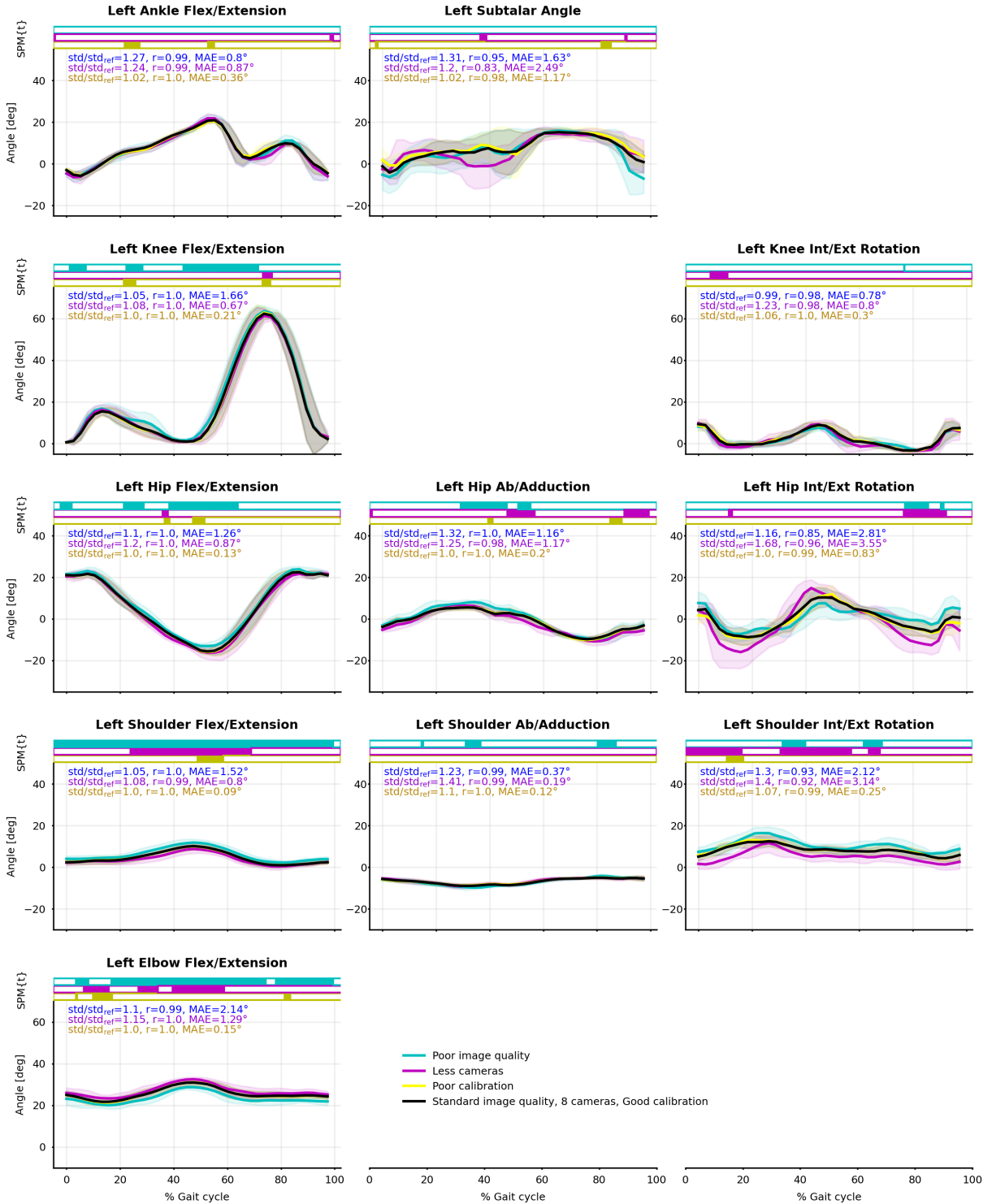


Figure 4.7: Joint angle means (solid line) and standard deviations (shaded area) from the eight captured cycles of walking. Reference condition (Ref) is black; degraded image quality (Im) is blue; four cameras instead of eight (4c) is purple; degraded calibration (Cal) is yellow. Pearson's correlation coefficient (r) and mean absolute error (MAE) between Ref and Im, 4c, Cal are reported. Paired t-tests along time were computed by SPM-1D and are represented as bar plots above the curves: a color rectangle means that there was a cluster of statistically significant differences ($\alpha = 0.05$) at that moment. Running and cycling figures can be found in the Supplementary Material.

Kinematics were more robust in the flexion/extension plane (Table 4.5), where std generally did not increase by more than 10% as compared to the Ref condition, and r was mostly equal to 1.00. The difference in robustness was not as obvious in the MAE variable since the range of motion was much smaller in other planes.

Task	Cond.	Flex./Ext.			Abd./Add.*			Int./Ext. rot.		
		std/std _{ref}	r	MAE (°)	std/std _{ref}	r	MAE (°)	std/std _{ref}	r	MAE (°)
Walking	Im	1.11	1.00	1.48	1.28	0.98	1.05	1.23	0.89	2.47
	4c	1.15	1.00	0.90	1.29	0.93	1.28	1.54	0.94	3.35
	Cal	1.01	1.00	0.19	1.04	0.99	0.50	1.04	0.99	0.54
Running	Im	1.03	1.00	0.98	1.08	0.98	0.48	1.13	0.98	1.41
	4c	1.03	1.00	0.98	1.18	0.93	1.00	1.14	0.97	4.06
	Cal	1.00	1.00	0.30	0.99	0.99	0.53	0.92	1.00	0.80
Cycling	Im	0.99	0.97	1.89	1.27	0.66	1.45	0.99	0.97	1.71
	4c	1.31	0.96	1.43	3.10	0.46	1.76	1.71	0.97	1.47
	Cal	1.00	1.00	0.39	1.06	0.96	0.36	1.02	1.00	1.00

*Table 4.5: Summary of angles statistics in the three rotation planes, averaged over all joints ($n = 5, 3, 2$ for Flexion/Extension, Abduction/Adduction, and Internal/External Rotation, respectively.). All conditions are represented: degraded image quality (Im), four cameras instead of eight (4c), and degraded calibration (Cal). These conditions were compared to the reference one (Ref) by calculating the ratio of standard deviation (std/std_{ref}), the Pearson's correlation coefficient (r), and the mean absolute error (MAE). *Ankle subtalar angle is assimilated to an abduction/adduction angle.*

The SPM showed some statistical differences along time between the reference condition and the degraded ones; however, they did not happen at any particular moment during the gait or pedaling cycle (Figure 4.7 for the walking task, and Figure A.1 and Figure A.2 in the Appendix for the running and cycling tasks).

4.4 Discussion

4.4.1 Pose2Sim

Pose2Sim allows for seamless markerless kinematics from a network of calibrated and synchronized cameras by connecting two widespread, renowned, and open-source tools: the OpenPose 2D pose estimator and the OpenSim movement analysis software. Overall, human intervention is scarce, which makes it more robust to human error. Pose2Sim automatically tracks the person of interest when people are in the background, considers the confidence given by the OpenPose estimation, and is robust to missing frames and to the person exiting the field of view of one or several cameras. To the best of our knowledge, it is also the first one taking advantage of a solid anatomical 3D model in order to solve some rotations around the limb and to account for physical consistency. It is very customizable, in the sense that the user can adjust most parameters and even use a different 2D pose estimator if needed, including for non-human subjects (such as DeepLabCut [Mathis2018] for example.)

4.4.2 Relevance, repeatability and robustness

The walking angle results seemed to be relevant when compared to the normative database. The noticeable discrepancies may be due to a difference between the angle definition of both models, especially in the ankle: the normative database calculated direct Euler angles between limb segments, while our OpenSim model took bone geometries into consideration. The shift in the hip angle was related to an excessive pelvis anteversion, which may have been induced by the model being underconstrained due to our dearth of keypoints. This lack of marker constraints could be partly compensated by adding joint constraints, especially around the spine (See next chapter on [Accuracy assessment](#), combining the [[Rajagopal2016](#)] and the [[Beaucage-Gauvreau2019](#)] models). In any case, the angle results seem to be relevant, but accuracy needs to be further investigated by comparing Pose2Sim markerless method to a reference marker-based one exploiting a similar model definition.

Repeatability was simply assessed by the standard deviation of angle time series across gait cycles, although it also includes the participant's intrinsic variability. However, the subject being young and healthy, his gait and cycling patterns were thought to be consistent. Hence, the results were repeatable as the standard deviation of angles across all strides within all tasks and conditions mostly stayed below 3°. Nevertheless, this standard deviation was still higher than the one previously reported by [[Kang2008](#)] for a young and healthy participant using a marker-based approach. It may be partly caused by our lack of a force plate and our low sampling rate, which did not let us measure a very accurate heel strike event, and thus could have induced some additional variability. In addition, our videos were sampled at 30 Hz instead of hundreds of Hertz as is usual in motion analysis. It is to be noted that high-speed video cameras can sample at a such speed and solve at least a part of this issue. Depending on the sports task investigated, a 3° standard deviation can be more or less of an issue.

Robustness was investigated based on the criteria exposed by [[Moeslund2001](#)]. First, people could be in the background. Then, several movement tasks have been investigated. Last, the workflow was confronted to three degraded conditions regarding image quality, camera number, and calibration. The results were also robust, since degraded conditions still gave consistent joint angles. A further SPM study showed occasional statistical differences along time, but did not reveal any part of the movement cycle to be more problematic than another. There was no apparent outlier in the 3D angle results, even in the degraded conditions. This was in spite of the presence of other people in the field of view and in spite of the subject walking out of it.

All stages of the workflow contributed to its robustness. First, we never had to deal with limb swapping, unlike other studies [[Nakano2019](#), [Slembrouck2020](#)]. This may be due to our use of the experimental Body_25b OpenPose model, which is claimed to decrease the number of false positives [[Hidalgo2019](#)]. Then, we used Pose2Sim to robustly sort the detected people and to triangulate 2D coordinates. These coordinates were the least precise in the Im condition where the image was strongly blurred and darkened, but Pose2Sim partly solved it by taking the OpenPose likelihood into account and by excluding the most inaccurate cameras: twice as many cameras were excluded as compared to the reference condition, which resulted in a reprojection error only 10% higher.

Finally, we used OpenSim to take advantage of a physically consistent full-body model and of an inverse kinematics optimization algorithm, which allowed us to refine our 3D data coordinates and to obtain 3D joint angles. The Cal condition simulated calibration errors, which bypassed the Pose2Sim safeguards since the OpenPose likelihood was unaffected, and the reprojection error stayed below the threshold. Despite it producing the largest reprojection error, virtually no difference with the reference condition was observed after the OpenSim pass. A 2 px calibration error (≈ 1 cm) is much worse than the maximum 1 px, or 3 mm usually recommended, but the mean absolute error it induced for us stayed below 0.5°.

Using four cameras rather than eight still gave relevant angle results, but the individual errors

of each camera cannot be blunted by the multiplicity of views, especially when faced with occlusion issues such as in the cycling task. The ankle joint angles were especially less robust regarding all considered dependent variables because the feet were more easily occluded by the cycling gear.

Ultimately, all conditions challenged the workflow at different stages, but the results remained stable and very close to those of the reference condition, with an average mean absolute error mostly lower than 1.5° , a correlation coefficient largely above 0.95, and a standard deviation usually increased by less than 20%. This demonstrates the robustness of the presented method in conditions that would have probably caused marker-based approaches to fail. Moreover, our reported angle deviations seem quite reasonable compared to errors in marker-based approaches, which can propagate up to 10° because of inter-operator differences [[della Croce1999](#), [Gorton2009](#)], to 3° because of tissue artifacts [[Benoit2015](#), [Cappozzo1995](#)], or to 3° depending on the joint center calculation method [[Leboeuf2019](#)]. Essentially, the findings presented here seem to indicate that the slight decline in repeatability is an acceptable compromise when put into perspective with the increase in robustness, in ease of use, and in new opportunities for analysis of sports performed "in-the-wild".

Nonetheless, it would be interesting to check for even more challenging conditions. We have investigated global Gaussian blur, but not movement blur, such as when the camera shutter speed is not high enough. It would also be interesting to investigate the effect of even larger calibration errors, even less cameras used, different camera placements, different camera types (such as GoPros with strong fisheye distortions), or different framerates or image definitions.

4.4.3 Limits and perspectives

Our use of a virtual scene helped us perfectly control all parameters of the capture. Although this scene is synthetically crafted, it looks similar to a real one. This is not thought to hinder the performance of 2D pose detection since deep-learning models are occasionally trained on synthetic datasets that look empirically less real and are still successful at augmenting ground-truth datasets (see [[Patel2021](#), [Wood2021](#), [Bolaños2021](#), [Varol2017](#)]). However, an image with a better definition and with a framerate over 30 fps may improve results. Furthermore, this capture design limited us to a low level of data, with only one subject and about 10 cycles analyzed per task.

We noticed that the cycling task was particularly challenging, probably because of self-occlusions and gear occlusions. With marker-based methods, setting some cameras closer to the ankles and in a lower position would have slightly improved this issue. However, it was not an option here since OpenPose only works very well if the whole body is visible. Unlike [[D'Antonio2021](#)], we did not find running to be more challenging for our system than walking. In the context of sports sciences, it would be useful to test other tasks, such as boxing (a typical 3D movement, explored in chapter 6 on [Application to boxing, using action cameras](#) [[Pagnon2022c](#)]), flipping (the 2D pose estimator may have trouble with upside-down people), swimming (in an environment with a different refractive index, with splashes around limb extremities), or a sport discipline with unusual outfits and large occlusions (such as motorbiking or fencing.)

Moreover, the [[Rajagopal2016](#)] model used as a basis does not appear to be well suited for road cycling since the spine is designed as a single rigid bone that cannot bend. This results in sharp shifts in hip abduction/adduction and internal/external rotation angles, which are not biomechanically coherent (see Figure A.2). However, the same issue would prevail even with marker-based methods and would only be solved by changing the spine definition in the OpenSim model. The full-body model with a fully articulated spine and ribcage developed by [[Bruno2015](#)] has far too many degrees of freedom for our small amount of detected keypoints; however, the lifting full-body (LFB) model validated by [[Beaucage-Gauvreau2019](#)] solved the spine challenge by constraining vertebra movements to each other, without adding any degrees of freedom. Pose2Sim

now provides a combination of these two models (see [Pose2Sim package](#)) in order to benefit from best accuracies both in the knee and in the spine. This is the one used in the next section on [Accuracy assessment](#).

It would also be useful to support multi-person analysis, to have a more accurate and extensive 2D pose estimator, to work in real time, and to provide a GUI. All these considerations are discussed in the Limitations and perspectives section of the previous chapter on the [Pose2Sim package](#).

[Desmarais2021] proposed a taxonomy of 3D pose estimation algorithms based on accuracy, speed, and robustness. Although more modalities could be tested, our workflow was robust in the range of our tested conditions. Speed was unaddressed, but although real-time analysis seems out of reach, a timely analysis of athletes' movements directly on the sports field appears to be achievable. Yet, ultimately, the accuracy of the workflow must be concurrently validated with a reference marker-based method. This is the topic of the next chapter.

5

Accuracy assessment

After robustness, accuracy needs to be addressed. Two-dimensional deep-learning pose estimation algorithms can suffer from biases in joint pose localizations, which are reflected in triangulated coordinates, and then in 3D joint angle estimation. Pose2Sim, our robust markerless kinematics workflow, comes with a physically consistent OpenSim skeletal model, meant to mitigate these errors.

Its accuracy was concurrently validated against a reference marker-based method. Lower-limb joint angles were estimated over three tasks (walking, running, and cycling) performed multiple times by one participant. When averaged over all joint angles, the coefficient of multiple correlation (CMC) remained above 0.9 in the sagittal plane, except for the hip in running, which suffered from a systematic 15° offset (CMC = 0.65), and for the ankle in cycling, which was partially occluded (CMC = 0.75). When averaged over all joint angles and all degrees of freedom, mean errors were 3.0°, 4.1°, and 4.0°, in walking, running, and cycling, respectively; and range of motion errors were 2.7°, 2.3°, and 4.3°, respectively. Given the magnitude of error traditionally reported in joint angles computed from a marker-based optoelectronic system, Pose2Sim is deemed accurate enough for the analysis of lower-body kinematics in walking, cycling, and running.

This chapter is adapted from the article published in the Sensors: "Pose2Sim: An End-to-End Workflow for 3D Markerless Sports Kinematics—Part 2: Accuracy" [Pagnon2022a].

Contents

5.1	Introduction	67
5.2	Methods	68
5.2.1	Data collection	68
5.2.2	Markerless analysis	68
5.2.3	Marker-based analysis	69
5.2.4	Statistical analysis	69
5.3	Results	70
5.3.1	Concurrent validation	70
5.3.2	Comparison with other systems	74
5.4	Discussion	74
5.4.1	Strengths of Pose2Sim and of markerless kinematic	74
5.4.2	Limits and perspectives	74
5.5	Conclusions	75

5.1 Introduction

Marker-based methods are often considered as the gold standard in motion analysis. Despite their accuracy, they bear several issues. Among others, marker placement hinders natural movement, and it is time-consuming. Therefore, markerless technologies are being examined to solve these issues. Among others, deep-learning based methods based on a network of calibrated RGB cameras are promising. They do not assume any particular environment, nor hinder the athlete's movement and focus, and they are particularly robust (see previous chapter on [Robustness assessment](#) [Pagnon2021]). However, they require delicate calibration, large storage space, and high computational capacities. The technology, nevertheless, is still maturing and some light-weight systems such as BlazePose [Bazarevsky2020] are being proposed, which can operate in real time on a mobile phone; however, they are still not quite as accurate as required for quantitative motion analysis [Mroz2021].

The most common evaluation metric for accuracy is the Mean Per Joint Position Error (MPJPE), which is the average Euclidian distance between the estimated joint coordinate and its ground truth. A large part of studies investigating 3D joint center estimation choose to triangulate the output of OpenPose [Cao2019]. Their MPJPE usually lies between 30 and 40 mm [Nakano2019, Slembruck2020, Labuguen2020]. Ankle MPJPEs are within the margin of error of marker-based technologies (1–15 mm), whereas knee and hip MPJPEs are greater (30–50 mm). These errors are systematic and likely due to "ground-truth" images being mislabeled in the training dataset [Needham2021b]. Triangulation from other 2D deep-learning algorithms (such as AlphaPose [Fang2017] and DeepLabCut [Mathis2018]) have also been compared [Needham2021b]. AlphaPose results are similar to OpenPose's; however, DeepLabCut errors are substantially higher.

Numerous studies have focused on the accuracy of 3D joint center estimation, but far fewer have examined 3D joint angle estimation. D'Antonio et al. computed direct flexion-extension angles for the lower limb from two cameras processed with OpenPose [D'Antonio2021]. Range of Motion (ROM) errors lay between 2.8° and 14.1°. Wade et al. calculated frontal and sagittal knee and hip angles with OpenPose, AlphaPose, and DeepLabCut [Wade2021]. They deemed the method accurate enough for assessing step length and velocity, but not for joint angle analysis. AniPose offers a toolkit for triangulating 2D poses from DeepLabCut [Karashchuk2021]. To our knowledge, it has only been concurrently validated for index finger angles in the sagittal plane, resulting in a root-mean-square error of 7.5 degrees [Geelen2021]. Theia, a commercially available software package for markerless analysis, uses its own patent-protected 2D pose estimator and triangulation procedure, and runs a skeletal model to constrain the results to physically consistent poses and movements [Kanko2021b]. Their root-mean-square error (RMSE) compared to a marker-based method ranged between 2.6° and 13.2°.

We previously proposed our open-source solution, Pose2Sim (see [Proposed solution: Pose2Sim Python package](#) [Pagnon2022b]). It robustly triangulates OpenPose results [Cao2019], and leads to an OpenSim output [Delp2007, Seth2018]. We showed that Pose2Sim was robust people in the background, to different sorts of movements (walking, running, and cycling), to dark and blurry images (0.5 gamma compression and 5.5 cm Gaussian blur), to 1 cm random calibration errors, and to using as few as four cameras (see previous chapter on [Robustness assessment](#) [Pagnon2021]). Now, the objective of this present study is to concurrently evaluate Pose2Sim's lower-limb 3D accuracy, with a marker-based method, and on the same tasks.

5.2 Methods

5.2.1 Data collection

The same adult male participant as in the previous chapter on [Robustness assessment](#) (1.89 m, 69 kg) was equipped with 83 reflective markers inspired from the CAST marker set [[Cappozzo1995](#)], composed of 35 anatomical markers, and 12 clusters of 4 markers (Figure 3.8). He was asked to perform three tasks: walking, running, and cycling, at a regular pace, back and forth across the capture space, following a regular pulsing sound (see previous chapter for further details). He provided his written consent prior to participating.

All tasks were performed in a room equipped with a green background for optimal segmentation of the subject with respect to the background, and 3D animated mesh extraction using a visual hull approach at each video frame [[Laurentini1994](#)]. Twenty opto-electronic cameras captured the 3D coordinates of the markers, and 68 video cameras allowed retrieval of 3D textured meshes of the participant, which we subsequently placed in a virtual environment and filmed from 8 virtual cameras (Figure 4.2). This gave us the opportunity to overlay our reflective markers, calculated joint centers, and OpenPose keypoints to the extracted mesh. This was particularly useful to correctly place OpenPose keypoints on the OpenSim model, i.e., with a systematic offset as regards true joint centers ([section 3.3](#)). The acquisition was restricted in terms of 3D volume covered by both systems and data storage, resulting in the analysis of 8, 13, and 13 cycles of walking, running, and cycling, respectively. Once 3D point coordinates were retrieved, both systems underwent processes that were as close to each other as possible: coordinates were sampled at 30 Hz, then they were filtered with a 4th-order 6 Hz low-pass Butterworth filter (which efficiently filtered out noise without underestimating peak values, including in extremities); heel strikes were detected in both cases with the method proposed by [[Zeni2008](#)]; stride duration was determined as the inverse of the frequency of the metronome followed by the participant; and inverse kinematics were optimized with the same OpenSim skeletal model.

5.2.2 Markerless analysis

All videos from our virtual cameras were processed by OpenPose (version 1.6), which delivered 2D joint coordinates for each view. We used the OpenPose experimental body_25b model (Figure 3.7) with the highest accuracy parameters [[Hidalgo2021](#)]. The Pose2Sim workflow was then used to track the person of interest, robustly triangulate the OpenPose 2D joint coordinates, and filter the resulting 3D coordinates. Then this output was fed to our OpenSim setup to constrain the results to physically consistent kinematics (more details in previous chapter).

Pose2Sim comes with a generic OpenSim skeletal model, that has been slightly improved as regard to the previous chapter. It was adapted from the human gait full-body model [[Rajagopal2016](#)] and the lifting full-body model [[Beaucage-Gauvreau2019](#)]. While the spine of the gait model is represented as a single rigid bone, it is articulated in the lifting model, and each lumbar vertebra is constrained to the next one. This is more accurate for activities for which the spine is bent, such as cycling. However, the knee joint is more accurately defined in the gait model: abduction/adduction and internal/external rotation angles are constrained to the flexion/extension angle, whereas they are simply ignored in the lifting one. This also improves the estimation of knee flexion. All else being equal, as we want our model to be as versatile as possible, we used the spine definition of the lifting model, and the knee definition of the gait model. Since we did not investigate muscle-related issues, they were removed to decrease computation time. Since no keypoint would have accounted for it, wrist flexion and deviation were locked at 0°, and arm pronation/supination was locked at 90°. Conversely, the translation of the pelvis was unlocked, in addition to the subtalar angle; and hip flexion was limited to 150° instead of 120° (which was not enough for the pedaling task). With regards to the previous chapter, marker placement was also improved in the OpenSim model. The average systematic offset between OpenPose-triangulated

keypoints and MoCap-calculated joint centers was measured on our 3D overlay view (Figure 3.8), and was taken into account when manually placing OpenPose keypoints onto the OpenSim unscaled model.

OpenSim (version 4.2) was used to scale the model to the participant on a T-pose, and then inverse kinematics was performed. Scale factors were computed with measurement-based scaling, i.e., by computing the ratio of distances between keypoints on the model, and experimental keypoints provided by the coordinates file of triangulated OpenPose data. Static pose weights were all set to 1, apart from Nose and Head keypoints which were set to 0.1, and Shoulder and Hip keypoints were set to 2. The participant was standing upright with feet flat during his T-pose, so we set a weight of 1 for a zero angle in pelvis list, pelvis tilt, L5-S1 flexion, and ankle angles. The offset in machine-learning-based joint center estimations has been demonstrated to be systematic and not dependent on the subject [Needham2021b] (nor on the operator); hence, once this bias has been taken into account in the generic model, the markers' adjustment step is unnecessary. Keypoint weight markers for inverse kinematics were the same as for scaling.

5.2.3 Marker-based analysis

The captured markers were automatically identified with an AIM procedure within the Qualisys Track Manager software (version 2019.1). Joint centers were then calculated. The centers of ankles, knees, wrists, and elbows were defined as the midpoints between the malleoli/epicondyles/styloids since it has been shown that when executed on a lean participant, functional methods do not improve the reliability of the kinematics of running [Pohl2010]. Hip joint center was defined with a functional method [Halvorsen2003]. The OpenSim model used for marker-based scaling and inverse kinematics was the same as the Pose2Sim model. Scale factors were computed similarly, but with marker data rather than with OpenPose keypoints. Weights proposed by the inverse kinematics solver of OpenSim were set to 5 for joint centers, to 1 for cluster markers, and to 2 for other anatomical markers. Inverse kinematics was processed with the same marker weights.

5.2.4 Statistical analysis

Since the participant did not report any locomotion impairment and the captured movements were mostly symmetrical, we only analyzed the right side. Our study focuses on the lower limb, but results for upper limb and sacro-lumbar joints are detailed in the [Appendix B](#) for information (Figure B.5 and Figure B.6 for walking, Figure B.7 and Figure B.8 for running, and Figure B.9 and Figure B.10 for cycling). The analyzed angles were ankle flexion/extension, subtalar angle, knee flexion/extension, and hip flexion/extension, abduction/adduction, and internal/external rotation provided by the OpenSim inverse kinematics procedure.

First, Pose2Sim scale factors were compared to marker-based ones, and RMS errors were reported and compared to OpenSim's best practice rules. Then, the overall similarity of paired angle waveforms was assessed with a special formulation of the coefficient of multiple correlation (CMC), specifically designed to compare different protocols or measurement systems [Ferrari2010]. The CMC gives a single result taking into account differences in correlation, gain, and offset. It reaches 1 if the curves are perfectly overlapped, and drops to zero if the curves are very dissimilar, or even to complex values (reported as "nan" hereafter). This is, for example, the case if the mean inter-protocol offset (averaged over time and trials) exceeds the grand mean ROM, which results in taking the square root of a negative number. CMC values are deemed good if between 0.75 and 0.84, very good if between 0.85 and 0.94, and excellent if above 0.95 [Ferrari2010]. The CMC results were then broken down to take an in-depth look into correlation, gain, and offset, separately. The strength of the linear relationship between kinematic analysis systems was assessed with the Pearson's r correlation coefficient. Gain was evaluated by computing the paired ROM differences. Once normality of the ROM errors was checked with a Shapiro-Wilk test [Shapiro1965], we computed related t-tests to verify whether the error was significant. Mean

inter-protocol offset angle, hereafter called mean error, was one of the outputs of the subsequent Bland–Altman analysis [Bland1986, Atkinson1998]. Once normality of the paired means of the angle differences was verified, we determined if the mean markerless angles were significantly different to the mean marker-based ones.

The Bland–Altman analysis gives some more information about the agreement between the considered markerless and marker-based systems [Bland1986, Atkinson1998]. It consists of plotting the difference between the values given by both systems against their mean, for all angular points at all time instances. Limits of agreement were defined as the interval within which 95% of data will be found, i.e., between mean difference ± 1.96 standard deviation, provided that the differences follow a normal distribution. Bland–Altman plots also help to identify the potential presence of heteroscedasticity, i.e., the fact that the spread of the error may depend on the angle magnitude [Atkinson1998].

Finally, root-mean-square errors (RMSE), mean errors ($Mean_{err}$), and ROM errors (ROM_{err}) were computed for the walking task to enable comparison with previously published metrics obtained using Theia3D, a commercial markerless solution [Kanko2021b], and Xsens [Zhang2013], a commercial system based on IMUs. Theia3D’s ROM results were approximated from reported graphics along the flexion/extension degree of freedom.

5.3 Results

5.3.1 Concurrent validation

Inverse kinematics is successful when OpenSim’s global optimizer keeps the model markers close to experimental markers, i.e., when RMSE is less than 2–4 cm according to OpenSim’s best practices. This was the case for both systems (Table 5.1). However, RMSE was particularly higher in cycling than in walking or running.

Task	Marker-based RMSE (cm)	Markerless RMSE (cm)
Walking	1.1–1.2	1.4–1.9
Running	1.5–1.7	1.5–2.1
Cycling	≈ 3.5	3.0–3.6

Table 5.1: RMSE between experimental and theoretical markers during OpenSim inverse kinematics, for both marker-based and Pose2Sim models.

CMC assesses waveform similarities between Pose2Sim and the marker-based reference method, by jointly evaluating correlation, gain, and offset. It was mostly very good ($CMC > 0.85$) to excellent ($CMC > 0.95$) in all tasks, all degrees of freedom, and all lower-body joints (Table 5.2, Figure 5.1, Figure B.1, and Figure B.3). This was especially the case along the flexion/extension degree of freedom, except for angles of the hip in running and of the ankle in cycling, for which CMC results suffered from an offset compared to the marker-based method. Hip abduction/adduction and internal/external rotation waveforms were not in good agreement ($CMC < 0.75$), except for the hip internal/external rotation angles in running. In cycling, all non-sagittal angles had complex CMCs, which means that no agreement was found at all.

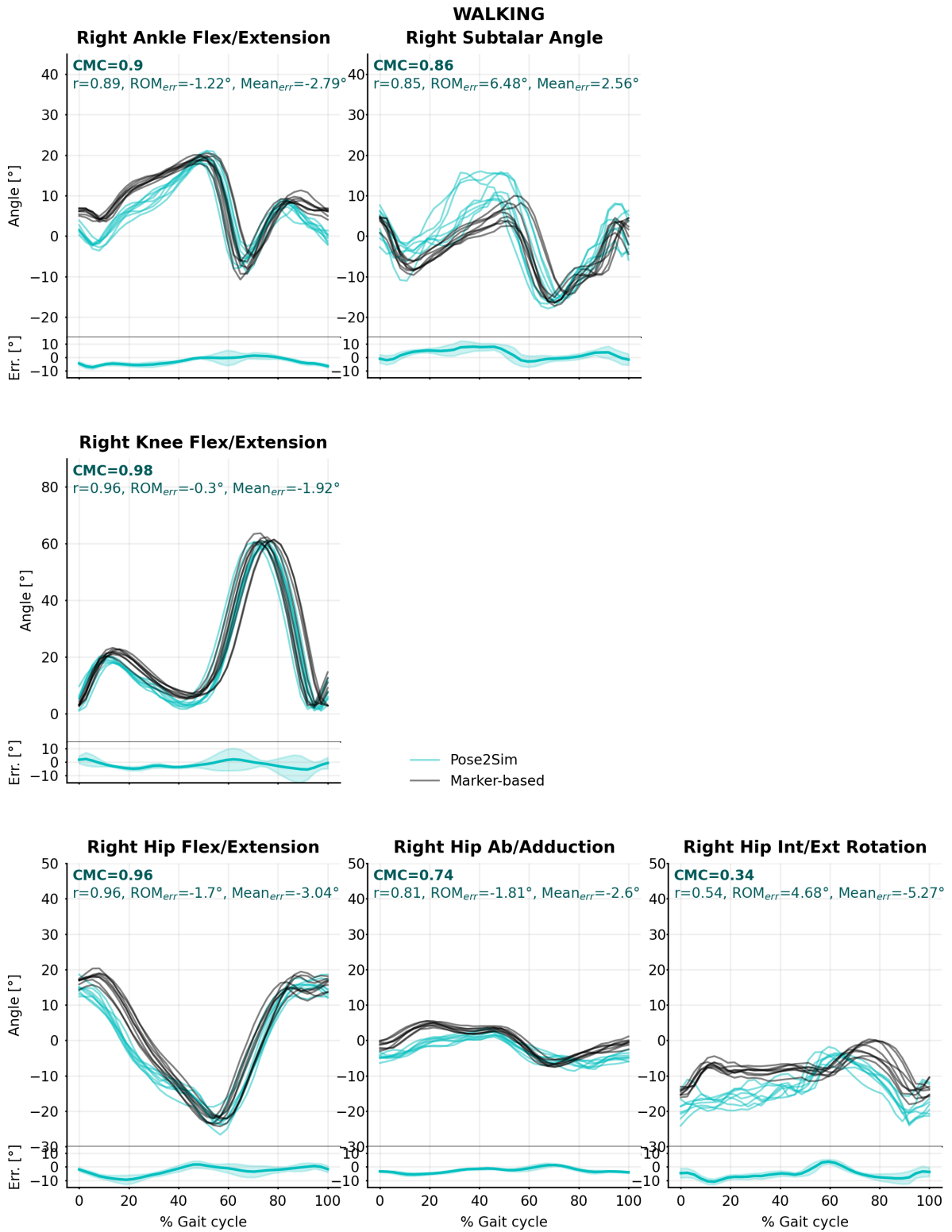


Figure 5.1: Pose2Sim (cyan) and marker-based (black) lower-body joint angles for the walking task. Coefficient of multiple correlation (CMC) is indicated, and broken down into, respectively, Pearson's coefficient (r) for correlation assessment, range of motion errors (ROM_{err}) for gain, and overall mean errors ($Mean_{err}$) for offset. Mean error and standard deviations are also represented at the bottom of the graphics. See Appendix B for running and cycling results, and for sacro-lumbar and upper-body results.

Task	Joint	Flex./Ext.				Abd./Add. ¹				Int./Ext. rot.			
		CMC	r	ROM _{err}	Mean _{err}	CMC	r	ROM _{err}	Mean _{err}	CMC	r	ROM _{err}	Mean _{err}
Walking	Ankle	0.90	0.89	-1.22	-2.79*	0.86	0.85	6.48*	2.56*	—	—	—	—
	Knee	0.98	0.96	-0.30	-1.92*	—	—	—	—	—	—	—	—
	Hip	0.96	0.96	-1.70	-3.04*	0.74	0.81	-1.81*	-2.6*	0.34	0.54	4.68*	-5.27*
Running	Ankle	0.99	0.99	-2.9*	-0.71*	0.97	0.96	2.20	0.96	—	—	—	—
	Knee	1.00	1.00	0.04	-0.65*	—	—	—	—	—	—	—	—
	Hip	0.65	0.95	4.01*	15.18*	0.37	0.65	-3.94*	-3.76*	0.93	0.95	1.25	-3.49*
Cycling	Ankle	0.75	0.85	1.93*	-6.73	nan	-0.32	10.27*	1.59*	—	—	—	—
	Knee	1.00	1.00	-2.94*	2.12*	—	—	—	—	—	—	—	—
	Hip	0.92	0.97	-5.91*	6.12*	nan	0.14	1.72*	-5.62*	nan	-0.07	3.07*	2.11*

*Table 5.2: Summary of comparisons between Pose2Sim and marker-based angle waveforms. A specific formulation of the Coefficient of Multiple Correlation (CMC) was used, specifically designed to compare different protocols or measurement systems. CMC jointly evaluates correlation, gain, and offset, which were respectively assessed with r-Pearson's coefficient, range of motion errors (ROM_{err}), and mean errors (Mean_{err}). *Significant at 5% level. ¹Despite ankle subtalar angle combines abduction/adduction and internal/external rotation, it is thereafter reported in the abduction/adduction column.*

Pearson's r correlation coefficient results were close to the CMC ones, albeit they became very good to excellent in the two angles that were affected by an offset. When averaged over all joint angles, errors in the range of motion (ROM_{err}) were 2.7° (sd = 2.1°), 2.3° (sd = 1.1°), and 4.3° (sd = 2.5°) in walking, running, and cycling, respectively. Along the flexion/extension degree of freedom, they were below 2°, 4°, and 6°, in walking, running, and cycling, respectively. Along the internal/external rotation degree of freedom, they stayed below 5°; however, they reached up to 10° along the abduction/adduction degree of freedom. Average mean angle errors (Mean_{err}) were 3.0° (sd = 1.0°), 4.1° (sd = 1.6°), and 4.0° (sd = 0.59°), in walking, running, and cycling, respectively. In walking and running, mean errors remained under 5.3° in all degrees of freedom, apart from the hip flexion/extension angle in running, which was offset by 15°. Although they were noticeably larger, mean errors were always under 7° in cycling (Table 5.2 and Table 5.3, Figure 5.1, Figure B.1, and Figure B.3)

Task	Joint	Flex./Ext.		Abd./Add.*		Int./Ext. rot.	
		Mean _{err} (°)	95% LoA (°)	Mean _{err} (°)	95% LoA (°)	Mean _{err} (°)	95% LoA (°)
Walking	Ankle	-2.79	[-9.4,3.8]	2.56	[-6.9,12]	—	—
	Knee	-1.92	[-12,8.4]	—	—	—	—
	Hip	-3.04	[-11.5,5.2]	-2.6	[-6.9,1.7]	-5.27	[-14,3.5]
Running	Ankle	-0.71	[-4.5,3.0]	0.96	[-5.3,7.2]	—	—
	Knee	-0.65	[-2.9,1.6]	—	—	—	—
	Hip	15.18	[5.5,25]	-3.76	[-9.2,1.6]	-3.49	[-9.3,2.4]
Cycling	Ankle	-6.73	[-16,2.1]	1.59	[-9.8,13]	—	—
	Knee	2.12	[-1.1,5.3]	—	—	—	—
	Hip	6.12	[-1.7,14]	-5.62	[-10,-1.1]	2.11	[-4.5,8.7]

*Table 5.3: Bland–Altman analysis results of 3D angle errors between Pose2Sim analysis and the reference marker-based one. Mean errors (Mean_{err}) and 95% limits of agreement (LoA) are represented. *Although ankle subtalar angle combines abduction/adduction and internal/external rotation, it is hereafter reported in the abduction/adduction column.*

Limits of Agreement (LoA) values were relatively evenly and randomly distributed among all tasks, degrees of freedom, and joints, averaging to an interval of 15° within which 95% of the errors would lie (Table 5.3, Figure 5.2, Figure B.2, and Figure B.4). Due to the limited range of motion of sacro-lumbar and upper-body angles, limits of agreement were smaller in these joint angles (Figure B.6, Figure B.8, and Figure B.10). Angle magnitude did not have an influence on the spread of errors (hence the data are homoscedastic), except for the cycling task for ankle angles and flexion/extension hip angles.

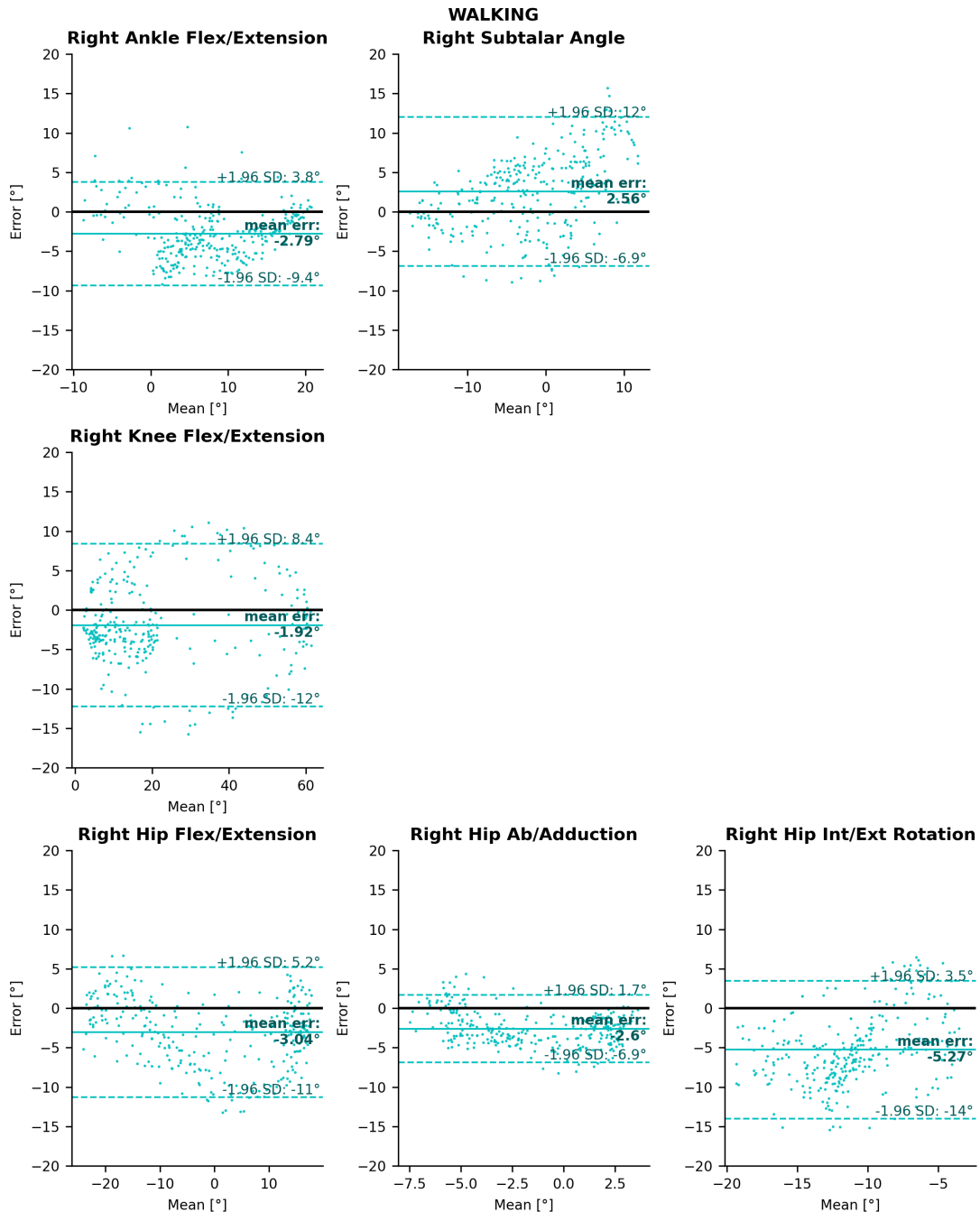


Figure 5.2: Bland–Altman analysis of lower-body joint angle errors for the walking task. Mean bias is represented as a horizontal solid, bold line, and 95% limits of agreement are represented as dotted lines. See Appendix B for running and cycling results, and for sacro-lumbar and upper-body results.

5.3.2 Comparison with other systems

The RMSE reported by Theia3D [Kanko2021b] was, on average, 1.5° higher than that of Pose2Sim, and its ROM errors were consistently higher, at least along the flexion/extension degree of freedom. However, the study using Xsens [Zhang2013] reported mean errors 0.3° lower on average, and ROM errors 1.0° lower on average (Table 5.4).

Error metric	Joint	Flex./Ext.			Abd./Add.			Int./Ext. rot.		
		Ours	Theia	Xsens	Ours	Theia	Xsens	Ours	Theia	Xsens
RMSE ($^\circ$)	Ankle	4	6.7	—	5.1	8	—	—	—	—
	Knee	5.1	3.3	—	—	—	—	—	—	—
	Hip	5.6	11	—	3.1	2.6	—	6.6	6.9	—
Mean _{err} ($^\circ$)	Ankle	2.79	—	2.15	2.56	—	1.81	—	—	—
	Knee	1.92	—	1.87	—	—	—	—	—	—
	Hip	3.04	—	2.47	2.6	—	4.83	5.27	—	3.02
ROM _{err} ($^\circ$)	Ankle	-1.22	≈ -10	0.4	6.48	—	1.38	—	—	—
	Knee	-0.3	≈ -1	0.8	—	—	—	—	—	—
	Hip	-1.7	≈ -10	2.42	-1.81	—	5.37	4.68	—	0.04

Table 5.4: Pose2Sim results compared to Theia3D [Kanko2021b] and to Xsens [Zhang2013] in the walking task. Root-mean-square error (RMSE), mean error (Meanerr), and range of motion (ROM) are examined. Theia3D’s ROM results were approximated from reported graphics along the flexion/extension degree of freedom. Both studies to which we compared our results involved a different setup (participants, cameras, protocol, etc.), therefore the differences cannot be totally attributed to the different technologies (markerless or IMU) nor to the different algorithm (Pose2Sim or Theia3D). * Although ankle subtalar angle combines abduction/adduction and internal/external rotation, it is hereafter reported in the abduction/adduction column.

5.4 Discussion

5.4.1 Strengths of Pose2Sim and of markerless kinematic

Hello, here is some text without a meaning. This text should show what a printed text will look like at this place. If you read this text, you will get no information. Really? Is there no information? Is there a difference between this text and some nonsense like “Huardest gefburn”? Kjift – not at all! A blind text like this gives you information about the selected font, how the letters are written and an impression of the look. This text should contain all letters of the alphabet and it should be written in of the original language. There is no need for special content, but the length of words should match the language.

5.4.2 Limits and perspectives

Hello, here is some text without a meaning. This text should show what a printed text will look like at this place. If you read this text, you will get no information. Really? Is there no information? Is there a difference between this text and some nonsense like “Huardest gefburn”?

Kjift – not at all! A blind text like this gives you information about the selected font, how the letters are written and an impression of the look. This text should contain all letters of the alphabet and it should be written in of the original language. There is no need for special content, but the length of words should match the language.

5.5 Conclusions

Hello, here is some text without a meaning. This text should show what a printed text will look like at this place. If you read this text, you will get no information. Really? Is there no information? Is there a difference between this text and some nonsense like “Huardest gefburn”? Kjift – not at all! A blind text like this gives you information about the selected font, how the letters are written and an impression of the look. This text should contain all letters of the alphabet and it should be written in of the original language. There is no need for special content, but the length of words should match the language.

6

Application to boxing, using action cameras

Pose2Sim in suboptimal conditions:

This chapter is adapted from the poster presented at the congress of the European College of Sport Science (ECSS): "A 3D markerless protocol with action cameras – Key performance indicators in boxing" [Pagnon2022c].

Contents

6.1	Objectives	78
6.1.1	Key Performance Indicators in boxing	78
6.1.2	Limits of research-grade systems in competitions	78
6.1.3	Objectives	78
6.2	Methods	79
6.2.1	4 conditions	79
6.2.2	Pose-calibration on ring dimensions	79
6.2.3	Post-synchronization on 2D movement speeds	79
6.2.4	GoPro spatio-temporal base into Qualysis'	79
6.2.5	Statistical analysis	79
6.3	Results	80
6.4	Discussion	80
6.4.1	Equipment and protocol vs. pose estimation model	80
6.4.2	Pros and cons of different systems	80

Calibration remains a challenging task in daylight, at a distance, with non research-grade cameras, and in a sports scene. It could be useful to make it more robust, either by implementing the Aniposelib library [[Karashchuk2020](#)], or by calibrating automatically on people's limb length [[Liu2022a](#)].

Along with synchronization, this topic will be detailed in Chapter 6 on [Application to boxing, using action cameras](#).

La calibration sera impossible si vous êtes trop loin. Les marqueurs réfléchissants ne réfléchiront pas la lumière des caméras (à tester : marqueurs actifs). Si vous voulez effectuer une post-calibration avec un checkerboard (avec cette méthode par exemple), il faudra que le checkerboard soit assez grand pour qu'il soit bien détecté. Une règle simple : pour avoir de bons résultats, la largeur du checkerboard doit remplir au moins un cinquième de l'image. Si vous voulez couvrir une scène de 20 m, il faudra un checkerboard de 4 m de large... Autre solution non testée : Calculer hors manip les paramètres intrinsèques des caméras vidéo. En manip, placer côté à côté des caméras MoCap Arqus et vidéo Miquis, faire la calibration des Arqus (plus performantes), et ajouter une translation dans les paramètres extrinsèques des Arqus pour avoir ceux des Miquis.

6.1 Objectives

6.1.1 Key Performance Indicators in boxing

Hello, here is some text without a meaning. This text should show what a printed text will look like at this place. If you read this text, you will get no information. Really? Is there no information? Is there a difference between this text and some nonsense like "Huardest gefburn"? Kjift – not at all! A blind text like this gives you information about the selected font, how the letters are written and an impression of the look. This text should contain all letters of the alphabet and it should be written in of the original language. There is no need for special content, but the length of words should match the language.

6.1.2 Limits of research-grade systems in competitions

Hello, here is some text without a meaning. This text should show what a printed text will look like at this place. If you read this text, you will get no information. Really? Is there no information? Is there a difference between this text and some nonsense like "Huardest gefburn"? Kjift – not at all! A blind text like this gives you information about the selected font, how the letters are written and an impression of the look. This text should contain all letters of the alphabet and it should be written in of the original language. There is no need for special content, but the length of words should match the language.

6.1.3 Objectives

Hello, here is some text without a meaning. This text should show what a printed text will look like at this place. If you read this text, you will get no information. Really? Is there no information? Is there a difference between this text and some nonsense like "Huardest gefburn"? Kjift – not at all! A blind text like this gives you information about the selected font, how the letters are written and an impression of the look. This text should contain all letters of the alphabet and it should be written in of the original language. There is no need for special content, but the length of words should match the language.

6.2 Methods

6.2.1 4 conditions

Hello, here is some text without a meaning. This text should show what a printed text will look like at this place. If you read this text, you will get no information. Really? Is there no information? Is there a difference between this text and some nonsense like “Huardest gefburn”? Kjift – not at all! A blind text like this gives you information about the selected font, how the letters are written and an impression of the look. This text should contain all letters of the alphabet and it should be written in of the original language. There is no need for special content, but the length of words should match the language.

6.2.2 Pose-calibration on ring dimensions

Hello, here is some text without a meaning. This text should show what a printed text will look like at this place. If you read this text, you will get no information. Really? Is there no information? Is there a difference between this text and some nonsense like “Huardest gefburn”? Kjift – not at all! A blind text like this gives you information about the selected font, how the letters are written and an impression of the look. This text should contain all letters of the alphabet and it should be written in of the original language. There is no need for special content, but the length of words should match the language.

6.2.3 Post-synchronization on 2D movement speeds

Hello, here is some text without a meaning. This text should show what a printed text will look like at this place. If you read this text, you will get no information. Really? Is there no information? Is there a difference between this text and some nonsense like “Huardest gefburn”? Kjift – not at all! A blind text like this gives you information about the selected font, how the letters are written and an impression of the look. This text should contain all letters of the alphabet and it should be written in of the original language. There is no need for special content, but the length of words should match the language.

6.2.4 GoPro spatio-temporal base into Qualysis'

Hello, here is some text without a meaning. This text should show what a printed text will look like at this place. If you read this text, you will get no information. Really? Is there no information? Is there a difference between this text and some nonsense like “Huardest gefburn”? Kjift – not at all! A blind text like this gives you information about the selected font, how the letters are written and an impression of the look. This text should contain all letters of the alphabet and it should be written in of the original language. There is no need for special content, but the length of words should match the language.

6.2.5 Statistical analysis

Hello, here is some text without a meaning. This text should show what a printed text will look like at this place. If you read this text, you will get no information. Really? Is there no information? Is there a difference between this text and some nonsense like “Huardest gefburn”? Kjift – not at all! A blind text like this gives you information about the selected font, how the letters are written and an impression of the look. This text should contain all letters of the alphabet and it should be written in of the original language. There is no need for special content, but the length of words should match the language.

6.3 Results

Hello, here is some text without a meaning. This text should show what a printed text will look like at this place. If you read this text, you will get no information. Really? Is there no information? Is there a difference between this text and some nonsense like “Huardest gefburn”? Kjift – not at all! A blind text like this gives you information about the selected font, how the letters are written and an impression of the look. This text should contain all letters of the alphabet and it should be written in of the original language. There is no need for special content, but the length of words should match the language.

6.4 Discussion

6.4.1 Equipment and protocol vs. pose estimation model

Hello, here is some text without a meaning. This text should show what a printed text will look like at this place. If you read this text, you will get no information. Really? Is there no information? Is there a difference between this text and some nonsense like “Huardest gefburn”? Kjift – not at all! A blind text like this gives you information about the selected font, how the letters are written and an impression of the look. This text should contain all letters of the alphabet and it should be written in of the original language. There is no need for special content, but the length of words should match the language.

6.4.2 Pros and cons of different systems

- Auto-calibration with person?
- Cloud computing?
- Temporal consistency?
- Shape information for less cameras?

Hello, here is some text without a meaning. This text should show what a printed text will look like at this place. If you read this text, you will get no information. Really? Is there no information? Is there a difference between this text and some nonsense like “Huardest gefburn”? Kjift – not at all! A blind text like this gives you information about the selected font, how the letters are written and an impression of the look. This text should contain all letters of the alphabet and it should be written in of the original language. There is no need for special content, but the length of words should match the language.

7

Application to BMX racing, jointly capturing pilot and bike

Résumé du chapitre possible ici.

Contents

7.1	Introduction	83
7.1.1	The start in BMX racing	83
7.2	Methods	83
7.2.1	Material and protocol	83
7.2.2	Pilot inverse kinematics	83
7.2.3	Bike inverse kinematics	83
7.2.4	Joined pilot and bike inverse kinematics	83
7.3	Results	84
7.4	Discussion	84
7.4.1	On these data	84
7.4.2	Limits and perspectives	84

7.1 Introduction

7.1.1 The start in BMX racing

Hello, here is some text without a meaning. This text should show what a printed text will look like at this place. If you read this text, you will get no information. Really? Is there no information? Is there a difference between this text and some nonsense like “Huardest gefburn”? Kjift – not at all! A blind text like this gives you information about the selected font, how the letters are written and an impression of the look. This text should contain all letters of the alphabet and it should be written in of the original language. There is no need for special content, but the length of words should match the language.

7.2 Methods

7.2.1 Material and protocol

Hello, here is some text without a meaning. This text should show what a printed text will look like at this place. If you read this text, you will get no information. Really? Is there no information? Is there a difference between this text and some nonsense like “Huardest gefburn”? Kjift – not at all! A blind text like this gives you information about the selected font, how the letters are written and an impression of the look. This text should contain all letters of the alphabet and it should be written in of the original language. There is no need for special content, but the length of words should match the language.

7.2.2 Pilot inverse kinematics

Hello, here is some text without a meaning. This text should show what a printed text will look like at this place. If you read this text, you will get no information. Really? Is there no information? Is there a difference between this text and some nonsense like “Huardest gefburn”? Kjift – not at all! A blind text like this gives you information about the selected font, how the letters are written and an impression of the look. This text should contain all letters of the alphabet and it should be written in of the original language. There is no need for special content, but the length of words should match the language.

7.2.3 Bike inverse kinematics

Hello, here is some text without a meaning. This text should show what a printed text will look like at this place. If you read this text, you will get no information. Really? Is there no information? Is there a difference between this text and some nonsense like “Huardest gefburn”? Kjift – not at all! A blind text like this gives you information about the selected font, how the letters are written and an impression of the look. This text should contain all letters of the alphabet and it should be written in of the original language. There is no need for special content, but the length of words should match the language.

7.2.4 Joined pilot and bike inverse kinematics

Marche pas avec nos qualités de vidéo : simulations

Hello, here is some text without a meaning. This text should show what a printed text will look like at this place. If you read this text, you will get no information. Really? Is there no information? Is there a difference between this text and some nonsense like “Huardest gefburn”? Kjift – not at all! A blind text like this gives you information about the selected font, how the letters are written and an impression of the look. This text should contain all letters of the alphabet

and it should be written in of the original language. There is no need for special content, but the length of words should match the language.

7.3 Results

Hello, here is some text without a meaning. This text should show what a printed text will look like at this place. If you read this text, you will get no information. Really? Is there no information? Is there a difference between this text and some nonsense like “Huardest gefburn”? Kjift – not at all! A blind text like this gives you information about the selected font, how the letters are written and an impression of the look. This text should contain all letters of the alphabet and it should be written in of the original language. There is no need for special content, but the length of words should match the language.

7.4 Discussion

7.4.1 On these data

Hello, here is some text without a meaning. This text should show what a printed text will look like at this place. If you read this text, you will get no information. Really? Is there no information? Is there a difference between this text and some nonsense like “Huardest gefburn”? Kjift – not at all! A blind text like this gives you information about the selected font, how the letters are written and an impression of the look. This text should contain all letters of the alphabet and it should be written in of the original language. There is no need for special content, but the length of words should match the language.

7.4.2 Limits and perspectives

Mathis2020 Principles, pitfalls and perspectives

splashes, occlusions, distance, etc

Voir Protocole doc:

General conclusion

*C*onclusion here.

Bibliography

- [Ahmad2013] Norhafizan Ahmad, Raja Ariffin Raja Ghazilla, Nazirah M. Khairi and Vijayabaskar Kasi. *Reviews on Various Inertial Measurement Unit (IMU) Sensor Applications*. International Journal of Signal Processing Systems, pages 256–262, 2013.
- [Aizerman1964] Mark A Aizerman. *Theoretical foundations of the potential function method in pattern recognition learning*. Automation and remote control, vol. 25, pages 821–837, 1964.
- [Andriluka2014] Mykhaylo Andriluka, Leonid Pishchulin, Peter Gehler and Bernt Schiele. *2D Human Pose Estimation: New Benchmark and State of the Art Analysis*. In IEEE Conference on Computer Vision and Pattern Recognition (CVPR), June 2014.
- [Argus2020] Argus. *Argus - 3D for the people*. Github, 2020.
- [Atha1984] J Atha. *Current techniques for measuring motion*. Applied ergonomics, vol. 15, no. 4, pages 245–257, 1984.
- [Atkinson1998] Greg Atkinson and Alan M Nevill. *Statistical methods for assessing measurement error (reliability) in variables relevant to sports medicine*. Sports medicine, vol. 26, no. 4, pages 217–238, 1998.
- [Baker2007] Richard Baker. *The history of gait analysis before the advent of modern computers*. Gait and Posture, vol. 26, no. 3, pages 331–342, 9 2007.
- [Bala2020] Praneet C. Bala, Benjamin R. Eisenreich, Seng Bum Michael Yoo, Benjamin Y. Hayden, Hyun Soo Park and Jan Zimmermann. *Automated markerless pose estimation in freely moving macaques with OpenMonkeyStudio*. Nature Communications, vol. 11, no. 1, page 4560, 9 2020.
- [Bao2022] Yiming Bao, Xu Zhao and Dahong Qian. *FusePose: IMU-Vision Sensor Fusion in Kinematic Space for Parametric Human Pose Estimation*. arXiv preprint arXiv:2208.11960, 2022.
- [Baral2018] Chitta Baral, Olac Fuentes and Vladik Kreinovich. *Why deep neural networks: a possible theoretical explanation*. In Constraint programming and decision making: Theory and applications, pages 1–5. Springer, 2018.
- [Barone2020] Francesco Barone, Marco Marrazzo and Claudio J Oton. *Camera calibration with weighted direct linear transformation and anisotropic uncertainties of image control points*. Sensors, vol. 20, no. 4, page 1175, 2020.

Bibliography

- [Barreto2022] Carlos Barreto. *Mocap MPP2SOS*, 2022.
- [Bazarevsky2020] Valentin Bazarevsky, Ivan Grishchenko, Karthik Raveendran, Tyler Zhu, Fan Zhang and Matthias Grundmann. *Blazepose: On-device real-time body pose tracking*. arXiv preprint arXiv:2006.10204, 2020.
- [Beaucage-Gauvreau2019] Erica Beaucage-Gauvreau, William S. P. Robertson, Scott C. E. Brandon, Robert Fraser, Brian J. C. Freeman, Ryan B. Graham, Dominic Thewlis and Claire F. Jones. *Validation of an OpenSim full-body model with detailed lumbar spine for estimating lower lumbar spine loads during symmetric and asymmetric lifting tasks*. Computer Methods in Biomechanics and Biomedical Engineering, vol. 22, no. 5, pages 451–464, 4 2019.
- [Benoit2015] D. L. Benoit, M. Damsgaard and M. S. Andersen. *Surface marker cluster translation, rotation, scaling and deformation: Their contribution to soft tissue artefact and impact on knee joint kinematics*. Journal of Biomechanics, vol. 48, no. 10, pages 2124–2129, 7 2015.
- [Bland1986] J Martin Bland and Douglas G Altman. *Statistical methods for assessing agreement between two methods of clinical measurement*. The lancet, vol. 327, no. 8476, pages 307–310, 1986.
- [Blender1998] Blender. *Blender*, 1998.
- [Bolaños2021] Luis A Bolaños, Dongsheng Xiao, Nancy L Ford, Jeff M LeDue, Pankaj K Gupta, Carlos Doeblei, Hao Hu, Helge Rhodin and Timothy H Murphy. *A three-dimensional virtual mouse generates synthetic training data for behavioral analysis*. Nature methods, vol. 18, no. 4, pages 378–381, 2021.
- [Borji2019] Ali Borji. *Pros and cons of gan evaluation measures*. Computer Vision and Image Understanding, vol. 179, pages 41–65, 2019.
- [Borji2022] Ali Borji. *Pros and cons of GAN evaluation measures: New developments*. Computer Vision and Image Understanding, vol. 215, page 103329, 2022.
- [Boser1992] Bernhard E Boser, Isabelle M Guyon and Vladimir N Vapnik. *A training algorithm for optimal margin classifiers*. In Proceedings of the fifth annual workshop on Computational learning theory, pages 144–152, 1992.
- [Bouwmans2019] Thierry Bouwmans, Sajid Javed, Maryam Sultana and Soon Ki Jung. *Deep neural network concepts for background subtraction: A systematic review and comparative evaluation*. Neural Networks, vol. 117, pages 8–66, 2019.
- [Bradski2000] G. Bradski. *The OpenCV Library*. Dr. Dobb's Journal of Software Tools, 2000.
- [Bridgeman2019] Lewis Bridgeman, Marco Volino, Jean-Yves Guillemaut and Adrian Hilton. *Multi-Person 3D Pose Estimation and Tracking in Sports*. pages 2487–2496, Long Beach, CA, USA, 6 2019. 2019 IEEE/CVF Conference on Computer Vision and Pattern Recognition Workshops (CVPRW), IEEE.

- [Bruno2015] Alexander G. Bruno, Mary L. Bouxsein and Dennis E. Anderson. *Development and Validation of a Musculoskeletal Model of the Fully Articulated Thoracolumbar Spine and Rib Cage*. Journal of Biomechanical Engineering, vol. 137, no. 8, page 081003, 8 2015.
- [Butterworth1930] Stephen Butterworth. *On the theory of filter amplifiers*. Wireless Engineer, vol. 7, no. 6, pages 536–541, 1930.
- [Cao2019] Zhe Cao, Gines Hidalgo, Tomas Simon, Shih-En Wei and Yaser Sheikh. *OpenPose: realtime multi-person 2D pose estimation using Part Affinity Fields*. IEEE transactions on pattern analysis and machine intelligence, vol. 43, no. 1, pages 172–186, 2019.
- [Cappozzo1995] A Cappozzo, F Catani, U Della Croce and A Leardini. *Position and orientation in space of bones during movement: anatomical frame definition and determination*. Clinical Biomechanics, vol. 10, no. 4, pages 171–178, 6 1995.
- [Carraro2017] Marco Carraro, Matteo Munaro, Jeff Burke and Emanuele Menegatti. *Real-time marker-less multi-person 3D pose estimation in RGB-Depth camera networks*. arXiv:1710.06235 [cs], 10 2017. arXiv: 1710.06235.
- [Ceseracciu2014] Elena Ceseracciu, Zimi Sawacha and Claudio Cobelli. *Comparison of Markerless and Marker-Based Motion Capture Technologies through Simultaneous Data Collection during Gait: Proof of Concept*. PLoS ONE, vol. 9, no. 3, page e87640, 3 2014.
- [Chai2014] T. Chai and R. R. Draxler. *Root mean square error (RMSE) or mean absolute error (MAE)? – Arguments against avoiding RMSE in the literature*. Geoscientific Model Development, vol. 7, no. 3, pages 1247–1250, 6 2014.
- [Chambers2015] Ryan Chambers, Tim J Gabbett, Michael H Cole and Adam Beard. *The use of wearable microsensors to quantify sport-specific movements*. Sports medicine, vol. 45, no. 7, pages 1065–1081, 2015.
- [Chen2020] Yucheng Chen, Yingli Tian and Mingyi He. *Monocular human pose estimation: A survey of deep learning-based methods*. Computer Vision and Image Understanding, vol. 192, page 102897, 3 2020.
- [Chicco2017] Davide Chicco. *Ten quick tips for machine learning in computational biology*. BioData mining, vol. 10, no. 1, pages 1–17, 2017.
- [Choppin2013] Simon Choppin and Jonathan Wheat. *The potential of the Microsoft Kinect in sports analysis and biomechanics*. Sports Technology, vol. 6, no. 2, pages 78–85, 5 2013.
- [Chu2021] Hau Chu, Jia-Hong Lee, Yao-Chih Lee, Ching-Hsien Hsu, Jia-Da Li and Chu-Song Chen. *Part-Aware Measurement for Robust Multi-View Multi-Human 3D Pose Estimation and Tracking*. page 10, 2021.
- [Cireşan2012] Dan Cireşan, Ueli Meier, Jonathan Masci and Jürgen Schmidhuber. *Multi-column deep neural network for traffic sign classification*. Neural networks, vol. 32, pages 333–338, 2012.

Bibliography

- [Cleveland1981] William S Cleveland. *LOWESS: A program for smoothing scatterplots by robust locally weighted regression.* American Statistician, vol. 35, no. 1, page 54, 1981.
- [Colombel2020] Jessica Colombel, Vincent Bonnet, David Daney, Raphael Dumas, Antoine Seilles and François Charpillet. *Physically Consistent Whole-Body Kinematics Assessment Based on an RGB-D Sensor. Application to Simple Rehabilitation Exercises.* Sensors, vol. 20, no. 10, page 2848, 5 2020.
- [Colyer2018] Steffi L Colyer, Murray Evans, Darren P Cosker and Aki IT Salo. *A review of the evolution of vision-based motion analysis and the integration of advanced computer vision methods towards developing a markerless system.* Sports medicine-open, vol. 4, no. 1, pages 1–15, 2018.
- [Cronin2019] Neil J. Cronin, Timo Rantalainen, Juha P. Ahtiainen, Esa Hynynen and Ben Waller. *Markerless 2D kinematic analysis of underwater running: A deep learning approach.* Journal of Biomechanics, vol. 87, pages 75–82, 4 2019.
- [Cronin2021] Neil J. Cronin. *Using deep neural networks for kinematic analysis: challenges and opportunities.* Journal of Biomechanics, page 110460, 5 2021.
- [Cybenko1989] George Cybenko. *Approximation by superpositions of a sigmoidal function.* Mathematics of control, signals and systems, vol. 2, no. 4, pages 303–314, 1989.
- [Dalal2005] Navneet Dalal and Bill Triggs. *Histograms of oriented gradients for human detection.* In 2005 IEEE computer society conference on computer vision and pattern recognition (CVPR’05), volume 1, pages 886–893. Ieee, 2005.
- [D’Antonio2021] Erika D’Antonio, Juri Taborri, Ilaria Miletì, Stefano Rossi and Fabrizio Patane. *Validation of a 3D Markerless System for Gait Analysis based on OpenPose and Two RGB Webcams.* IEEE Sensors Journal, pages 1–1, 2021.
- [Dawson-Howe1994] Kenneth M. Dawson-Howe and David Vernon. *Simple pinhole camera calibration.* International Journal of Imaging Systems and Technology, vol. 5, no. 1, pages 1–6, 1994.
- [della Croce1999] U. della Croce, A. Cappozzo and D. C. Kerrigan. *Pelvis and lower limb anatomical landmark calibration precision and its propagation to bone geometry and joint angles.* Medical and Biological Engineering and Computing, vol. 37, no. 2, pages 155–161, 3 1999.
- [Delp2007] Scott L Delp, Frank C Anderson, Allison S Arnold, Peter Loan, Ayman Habib, Chand T John, Eran Guendelman and Darryl G Thelen. *OpenSim: open-source software to create and analyze dynamic simulations of movement.* IEEE transactions on biomedical engineering, vol. 54, no. 11, pages 1940–1950, 2007.
- [Deng2009] J. Deng, W. Dong, R. Socher, L.-J. Li, K. Li and L. Fei-Fei. *ImageNet: A Large-Scale Hierarchical Image Database.* 2009.

- [Desmarais2021] Yann Desmarais, Denis Mottet, Pierre Slanger and Philippe Montesinos. *A review of 3D human pose estimation algorithms for markerless motion capture*. Computer Vision and Image Understanding, vol. 212, page 103275, 2021.
- [Dong2019] Junting Dong, Wen Jiang, Qixing Huang, Hujun Bao and Xiaowei Zhou. *Fast and Robust Multi-Person 3D Pose Estimation From Multiple Views*. pages 7784–7793, Long Beach, CA, USA, 6 2019. 2019 IEEE/CVF Conference on Computer Vision and Pattern Recognition (CVPR), IEEE.
- [Dong2020] Junting Dong, Qing Shuai, Yuanqing Zhang, Xian Liu, Xiaowei Zhou and Hujun Bao. *Motion Capture from Internet Videos*. In Andrea Vedaldi, Horst Bischof, Thomas Brox and Jan-Michael Frahm, éditeurs, Computer Vision – ECCV 2020, volume 12347, pages 210–227. Springer International Publishing, Cham, 2020.
- [Drazan2021] John F. Drazan, William T. Phillips, Nidhi Seethapathi, Todd J. Hullfish and Josh R. Baxter. *Moving outside the lab: Markerless motion capture accurately quantifies sagittal plane kinematics during the vertical jump*. Journal of Biomechanics, vol. 125, page 110547, 8 2021.
- [EasyMocap2021] EasyMocap. *EasyMoCap - Make human motion capture easier*. Github, 2021.
- [Ershadi-Nasab2021] Sara Ershadi-Nasab, Shohreh Kasaei and Esmaeil Sanaei. *Uncalibrated multi-view multiple humans association and 3D pose estimation by adversarial learning*. Multimedia Tools and Applications, vol. 80, no. 2, pages 2461–2488, 1 2021.
- [Fang2017] Hao-Shu Fang, Shuqin Xie, Yu-Wing Tai and Cewu Lu. *RMPE: Regional Multi-person Pose Estimation*. pages 2353–2362, Venice, 10 2017. 2017 IEEE International Conference on Computer Vision (ICCV), IEEE.
- [Fernández-González2020] Pilar Fernández-González, Aikaterini Koutsou, Alicia Cuesta-Gómez, María Carratalá-Tejada, Juan Carlos Miangolarra-Page and Francisco Molina-Rueda. *Reliability of kinovea® software and agreement with a three-dimensional motion system for gait analysis in healthy subjects*. Sensors, vol. 20, no. 11, page 3154, 2020.
- [Ferrari2010] Alberto Ferrari, Andrea Giovanni Cutti and Angelo Cappello. *A new formulation of the coefficient of multiple correlation to assess the similarity of waveforms measured synchronously by different motion analysis protocols*. Gait & posture, vol. 31, no. 4, pages 540–542, 2010.
- [Fisch2020] Martin Fisch and Ronald Clark. *Orientation Keypoints for 6D Human Pose Estimation*. arXiv:2009.04930 [cs], 9 2020. arXiv: 2009.04930.
- [Fischler1981] Martin A Fischler and Robert C Bolles. *Random sample consensus: a paradigm for model fitting with applications to image analysis and automated cartography*. Communications of the ACM, vol. 24, no. 6, pages 381–395, 1981.

Bibliography

- [Fukuchi2018] Claudiane A. Fukuchi, Reginaldo K. Fukuchi and Marcos Duarte. *A public dataset of overground and treadmill walking kinematics and kinetics in healthy individuals*. PeerJ, vol. 6, page e4640, 4 2018.
- [Geelen2021] Jinne E Geelen, Mariana P Branco, Nick F Ramsey, Frans CT Van Der Helm, Winfred Mugge and Alfred C Schouten. *MarkerLess Motion Capture: ML-MoCap, a low-cost modular multi-camera setup*. In 2021 43rd Annual International Conference of the IEEE Engineering in Medicine & Biology Society (EMBC), pages 4859–4862. IEEE, 2021.
- [Ghasemzadeh2021] Seyed Abolfazl Ghasemzadeh, Gabriel Van Zandycke, Maxime Istasse, Niels Sayez, Amirafshar Moshtaghpoor and Christophe De Vleeschouwer. *DeepSportLab: a Unified Framework for Ball Detection, Player Instance Segmentation and Pose Estimation in Team Sports Scenes*. arXiv preprint arXiv:2112.00627, 2021.
- [Girshick2014] Ross Girshick, Jeff Donahue, Trevor Darrell and Jitendra Malik. *Rich Feature Hierarchies for Accurate Object Detection and Semantic Segmentation*. In 2014 IEEE Conference on Computer Vision and Pattern Recognition, pages 580–587, 2014.
- [Girshick2015] Ross Girshick. *Fast r-cnn*. In Proceedings of the IEEE international conference on computer vision, pages 1440–1448, 2015.
- [Goodfellow2016] Ian Goodfellow, Yoshua Bengio and Aaron Courville. Deep learning. MIT Press, 2016. <http://www.deeplearningbook.org>.
- [Gorton2009] George E. Gorton, David A. Hebert and Mary E. Gannotti. *Assessment of the kinematic variability among 12 motion analysis laboratories*. Gait and Posture, vol. 29, no. 3, pages 398–402, 4 2009.
- [Guo2022] Jiamin Guo, Qin Zhang, Hui Chai and Yibin Li. *Obtaining lower-body Euler angle time series in an accurate way using depth camera relying on Optimized Kinect CNN*. Measurement, vol. 188, page 110461, 2022.
- [Halvorsen2003] Kjartan Halvorsen. *Bias compensated least squares estimate of the center of rotation*. Journal of Biomechanics, vol. 36, no. 7, pages 999–1008, 2003.
- [Han2013] Jungong Han, Ling Shao, Dong Xu and Jamie Shotton. *Enhanced Computer Vision With Microsoft Kinect Sensor: A Review*. IEEE Transactions on Cybernetics, vol. 43, no. 5, pages 1318–1334, 10 2013. event: IEEE Transactions on Cybernetics.
- [Haralabidis2020] Nicos Haralabidis, David John Saxby, Claudio Pizzolato, Laurie Needham, Dario Cazzola and Clare Minahan. *Fusing Accelerometry with Videography to Monitor the Effect of Fatigue on Punching Performance in Elite Boxers*. Sensors (Basel, Switzerland), vol. 20, no. 20, 10 2020.
- [Hartley1997] Richard I. Hartley and Peter Sturm. *Triangulation*. Computer Vision and Image Understanding, vol. 68, no. 2, pages 146–157, 11 1997.

- [Hawkins2004] Douglas M Hawkins. *The problem of overfitting*. Journal of chemical information and computer sciences, vol. 44, no. 1, pages 1–12, 2004.
- [He2017] Kaiming He, Georgia Gkioxari, Piotr Dollár and Ross Girshick. *Mask r-cnn*. In Proceedings of the IEEE international conference on computer vision, pages 2961–2969, 2017.
- [He2020] Yihui He, Rui Yan, Katerina Fragkiadaki and Shou-I Yu. *Epi-polar Transformers*. pages 7776–7785. 2020 IEEE/CVF Conference on Computer Vision and Pattern Recognition (CVPR), 6 2020. ISSN: 2575-7075.
- [Hidalgo2019] Gines Hidalgo, Yaadhav Raaj, Haroon Idrees, Donglai Xiang, Hanbyul Joo, Tomas Simon and Yaser Sheikh. *Single-network whole-body pose estimation*. In Proceedings of the IEEE/CVF International Conference on Computer Vision, pages 6982–6991, 2019.
- [Hidalgo2021] Ginés Hidalgo. *OpenPose 3D reconstruction module*, 2021.
- [Hofmann2008] Thomas Hofmann, Bernhard Schölkopf and Alexander J Smola. *Kernel methods in machine learning*. The annals of statistics, vol. 36, no. 3, pages 1171–1220, 2008.
- [Holm2013] Søren Holm. *Declaration of helsinki*. International encyclopedia of ethics, 2013.
- [Insafutdinov2016] Eldar Insafutdinov, Leonid Pishchulin, Bjoern Andres, Mykhaylo Andriluka and Bernt Schiele. *Deepcut: A deeper, stronger, and faster multi-person pose estimation model*. In European conference on computer vision, pages 34–50. Springer, 2016.
- [Iskakov2019] Karim Iskakov, Egor Burkov, Victor Lempitsky and Yury Malkov. *Learnable Triangulation of Human Pose*. pages 7717–7726, Seoul, Korea (South), 10 2019. 2019 IEEE/CVF International Conference on Computer Vision (ICCV), IEEE.
- [Johnston2019] William Johnston, Martin O'Reilly, Rob Argent and Brian Caulfield. *Reliability, validity and utility of inertial sensor systems for postural control assessment in sport science and medicine applications: a systematic review*. Sports Medicine, vol. 49, no. 5, pages 783–818, 2019.
- [Kang2008] Hyun Gu Kang and Jonathan B. Dingwell. *Separating the effects of age and walking speed on gait variability*. Gait and Posture, vol. 27, no. 4, pages 572–577, 5 2008.
- [Kanko2021a] Robert M. Kanko, Elise Laende, W. Scott Selbie and Kevin J. Deluzio. *Inter-session repeatability of markerless motion capture gait kinematics*. Journal of Biomechanics, vol. 121, page 110422, 5 2021.
- [Kanko2021b] Robert M. Kanko, Elise K. Laende, Elysia M. Davis, W. Scott Selbie and Kevin J. Deluzio. *Concurrent assessment of gait kinematics using marker-based and markerless motion capture*. Journal of Biomechanics, page 110665, 8 2021.

Bibliography

- [Karashchuk2020] Pierre Karashchuk. *Anipose lib: An easy-to-use library for calibrating cameras in python*, 2020.
- [Karashchuk2021] Pierre Karashchuk, Katie L Rupp, Evyn S Dickinson, Sarah Walling-Bell, Elischa Sanders, Eiman Azim, Bingni W Brunton and John C Tuthill. *Anipose: a toolkit for robust markerless 3D pose estimation*. Cell reports, vol. 36, no. 13, page 109730, 2021.
- [Kidziński2020] Łukasz Kidziński, Bryan Yang, Jennifer L. Hicks, Apoorva Rajagopal, Scott L. Delp and Michael H. Schwartz. *Deep neural networks enable quantitative movement analysis using single-camera videos*. Nature Communications, vol. 11, no. 1, page 4054, 12 2020.
- [Kitamura2022] Takumi Kitamura, Hitoshi Teshima, Diego Thomas and Hiroshi Kawasaki. *Refining OpenPose with a new sports dataset for robust 2D pose estimation*. In Proceedings of the IEEE/CVF Winter Conference on Applications of Computer Vision, pages 672–681, 2022.
- [Kreiss2022] Sven Kreiss, Lorenzo Bertoni and Alexandre Alahi. *OpenPif-Paf: Composite Fields for Semantic Keypoint Detection and Spatio-Temporal Association*. IEEE Transactions on Intelligent Transportation Systems, vol. 23, no. 8, pages 13498–13511, 2022.
- [Krizhevsky2017] Alex Krizhevsky, Ilya Sutskever and Geoffrey E Hinton. *Imagenet classification with deep convolutional neural networks*. Communications of the ACM, vol. 60, no. 6, pages 84–90, 2017.
- [Labuguen2020] Rollyn T. Labuguen, Wally Enrico M. Ingco, Salvador Blanco Negrete, Tonan Kogami and Tomohiro Shibata. *Performance Evaluation of Markerless 3D Skeleton Pose Estimates with Pop Dance Motion Sequence*. Rapport technique, 4 2020. DOI: 10.1101/2020.04.15.010702.
- [Lauer2022] Jessy Lauer, Mu Zhou, Shaokai Ye, William Menegas, Steffen Schneider, Tanmay Nath, Mohammed Mostafizur Rahman, Valentina Di Santo, Daniel Soberanes, Guoping Fenget al. *Multi-animal pose estimation, identification and tracking with DeepLabCut*. Nature Methods, vol. 19, no. 4, pages 496–504, 2022.
- [Laurentini1994] Aldo Laurentini. *The visual hull concept for silhouette-based image understanding*. IEEE Transactions on pattern analysis and machine intelligence, vol. 16, no. 2, pages 150–162, 1994.
- [Leboeuf2019] F. Leboeuf, J. Reay, R. Jones and M. Sangeux. *The effect on conventional gait model kinematics and kinetics of hip joint centre equations in adult healthy gait*. Journal of Biomechanics, vol. 87, pages 167–171, 4 2019.
- [LeCun1998] Yann LeCun, Léon Bottou, Yoshua Bengio and Patrick Haffner. *Gradient-based learning applied to document recognition*. Proceedings of the IEEE, vol. 86, no. 11, pages 2278–2324, 1998.
- [Li2019] Zongmian Li, Jiri Sedlar, Justin Carpentier, Ivan Laptev, Nicolas Mansard and Josef Sivic. *Estimating 3D Motion and Forces of*

- Person-Object Interactions From Monocular Video.* pages 8632–8641, Long Beach, CA, USA, 6 2019. 2019 IEEE/CVF Conference on Computer Vision and Pattern Recognition (CVPR), IEEE.
- [Li2020] Yong-Lu Li, Liang Xu, Xinpeng Liu, Xijie Huang, Yue Xu, Shiyi Wang, Hao-Shu Fang, Ze Ma, Mingyang Chen and Cewu Lu. *Pastanet: Toward human activity knowledge engine*. In Proceedings of the IEEE/CVF Conference on Computer Vision and Pattern Recognition, pages 382–391, 2020.
- [Liao2020] Rijun Liao, Shiqi Yu, Weizhi An and Yongzhen Huang. *A model-based gait recognition method with body pose and human prior knowledge*. Pattern Recognition, vol. 98, page 107069, 2 2020.
- [Lin2014] Tsung-Yi Lin, Michael Maire, Serge Belongie, James Hays, Pietro Perona, Deva Ramanan, Piotr Dollár and C Lawrence Zitnick. *Microsoft coco: Common objects in context*. In European conference on computer vision, pages 740–755. Springer, 2014.
- [Liu2022a] Kang Liu, Lingling Chen, Liang Xie, Jian Yin, Shuwei Gan, Ye Yan and Erwei Yin. *Auto calibration of multi-camera system for human pose estimation*. IET Computer Vision, 2022.
- [Liu2022b] Pin-Ling Liu and Chien-Chi Chang. *Simple method integrating Open-Pose and RGB-D camera for identifying 3D body landmark locations in various postures*. International Journal of Industrial Ergonomics, vol. 91, page 103354, 2022.
- [Liu2022c] Wu Liu and Tao Mei. *Recent Advances of Monocular 2D and 3D Human Pose Estimation: A Deep Learning Perspective*. ACM Comput. Surv., mar 2022.
- [Loper2015] Matthew Loper, Naureen Mahmood, Javier Romero, Gerard Pons-Moll and Michael J. Black. *SMPL: a skinned multi-person linear model*. ACM Transactions on Graphics, vol. 34, no. 6, pages 1–16, 11 2015.
- [López-Muñoz2006] Francisco López-Muñoz, Jesús Boya and Cecilio Alamo. *Neuron theory, the cornerstone of neuroscience, on the centenary of the Nobel Prize award to Santiago Ramón y Cajal*. Brain research bulletin, vol. 70, no. 4-6, pages 391–405, 2006.
- [Louis2022] Nathan Louis, Tylan N. Templin, Travis D. Eliason, Daniel P. Nicolella and Jason J. Corso. *Learning to Estimate External Forces of Human Motion in Video*. no. arXiv:2207.05845, Jul 2022.
- [Lu2015] Chaochao Lu and Xiaou Tang. *Surpassing human-level face verification performance on LFW with GaussianFace*. In Twenty-ninth AAAI conference on artificial intelligence, 2015.
- [Ludwig2020] Katja Ludwig, Moritz Einfalt and Rainer Lienhart. *Robust estimation of flight parameters for ski jumpers*. In 2020 IEEE International Conference on Multimedia & Expo Workshops (ICMEW), pages 1–6. IEEE, 2020.

Bibliography

- [Mahmood2019] Naureen Mahmood, Nima Ghorbani, Nikolaus F. Troje, Gerard Pons-Moll and Michael Black. *AMASS: Archive of Motion Capture As Surface Shapes*. In 2019 IEEE/CVF International Conference on Computer Vision (ICCV), pages 5441–5450, 2019.
- [Maji2022] Debapriya Maji, Soyeb Nagori, Manu Mathew and Deepak Poddar. *YOLO-Pose: Enhancing YOLO for Multi Person Pose Estimation Using Object Keypoint Similarity Loss*. In Proceedings of the IEEE/CVF Conference on Computer Vision and Pattern Recognition, pages 2637–2646, 2022.
- [Mathis2018] Alexander Mathis, Pranav Mamidanna, Kevin M. Cury, Taiga Abe, Venkatesh N. Murthy, Mackenzie Weygandt Mathis and Matthias Bethge. *DeepLabCut: markerless pose estimation of user-defined body parts with deep learning*. Nature Neuroscience, vol. 21, no. 9, pages 1281–1289, 9 2018.
- [Matthis2022] Matthis. *FreeMoCap: A free, open source markerless motion capture system*, 2022.
- [Maya1998] Maya. *Maya*, 1998.
- [McCulloch1943] Warren S McCulloch and Walter Pitts. *A logical calculus of the ideas immanent in nervous activity*. The bulletin of mathematical biophysics, vol. 5, no. 4, pages 115–133, 1943.
- [Mehta2020] Dushyant Mehta, Oleksandr Sotnychenko, Franziska Mueller, Weipeng Xu, Mohamed Elgharib, Pascal Fua, Hans-Peter Seidel, Helge Rhodin, Gerard Pons-Moll and Christian Theobalt. *XNect: real-time multi-person 3D motion capture with a single RGB camera*. ACM Transactions on Graphics, vol. 39, no. 4, page 82:82:1–82:82:17, 7 2020.
- [Miller1980] Norman R. Miller, Robert Shapiro and Thomas M. McLaughlin. *A technique for obtaining spatial kinematic parameters of segments of biomechanical systems from cinematographic data*. Journal of Biomechanics, vol. 13, no. 7, pages 535–547, 1 1980.
- [Minaee2021] Shervin Minaee, Yuri Y Boykov, Fatih Porikli, Antonio J Plaza, Nasser Kehtarnavaz and Demetri Terzopoulos. *Image segmentation using deep learning: A survey*. IEEE transactions on pattern analysis and machine intelligence, 2021.
- [Minsky1969] Marvin Minsky and Seymour Papert. *Perceptrons: An introduction to computational geometry*. Cambridge tiass., HIT, vol. 479, page 480, 1969.
- [Moeslund2001] Thomas B. Moeslund and Erik Granum. *Review - A Survey of Computer Vision-Based Human Motion Capture*. Computer Vision and Image Understanding, vol. 81, no. 3, pages 231–268, 3 2001.
- [Mroz2021] Sarah Mroz, Natalie Baddour, Connor McGuirk, Pascale Juneau, Albert Tu, Kevin Cheung and Edward Lemaire. *Comparing the Quality of Human Pose Estimation with BlazePose or OpenPose*. In 2021 4th International Conference on Bio-Engineering for Smart Technologies (BioSMART), page 1–4, Dec 2021.

- [Mündermann2006] Lars Mündermann, Stefano Corazza and Thomas P. Andriacchi. *The evolution of methods for the capture of human movement leading to markerless motion capture for biomechanical applications.* Journal of NeuroEngineering and Rehabilitation, vol. 3, no. 1, page 6, 3 2006.
- [Nakano2019] Nobuyasu Nakano, Tetsuro Sakura, Kazuhiro Ueda, Leon Omura, Arata Kimura, Yoichi Iino, Senshi Fukashiro and Shinsuke Yoshioka. *Evaluation of 3D markerless motion capture accuracy using Open-Pose with multiple video cameras.* Rapport technique, 11 2019. DOI: 10.1101/842492.
- [Needham2021a] Laurie Needham, Murray Evans, Darren P Cosker and Steffi L Colyer. *Can markerless pose estimation algorithms estimate 3D mass centre positions and velocities during linear sprinting activities?* Sensors, vol. 21, no. 8, page 2889, 2021.
- [Needham2021b] Laurie Needham, Murray Evans, Darren P Cosker, Logan Wade, Polly M McGuigan, James L Bilzon and Steffi L Colyer. *The accuracy of several pose estimation methods for 3D joint centre localisation.* Scientific reports, vol. 11, no. 1, pages 1–11, 2021.
- [Novikoff1963] Albert B Novikoff. *On convergence proofs for perceptrons.* Rapport technique, STANFORD RESEARCH INST MENLO PARK CA, 1963.
- [Pagliari2015] Diana Pagliari and Livio Pinto. *Calibration of kinect for xbox one and comparison between the two generations of microsoft sensors.* Sensors, vol. 15, no. 11, pages 27569–27589, 2015.
- [Pagnon2020] David Pagnon. *Maya MoCap*, 2020.
- [Pagnon2021] David Pagnon, Mathieu Domalain and Lionel Reveret. *Pose2Sim: An End-to-End Workflow for 3D Markerless Sports Kinematics—Part 1: Robustness.* Sensors, vol. 21, no. 19, 2021.
- [Pagnon2022a] David Pagnon, Mathieu Domalain and Lionel Reveret. *Pose2Sim: An End-to-End Workflow for 3D Markerless Sports Kinematics—Part 2: Accuracy.* Sensors, vol. 22, no. 7, 2022.
- [Pagnon2022b] David Pagnon, Mathieu Domalain and Lionel Reveret. *Pose2Sim: An open-source Python package for multiview markerless kinematics.* Journal of Open Source Software, vol. 7, no. 77, page 4362, 2022.
- [Pagnon2022c] David Pagnon, Mathieu Domalain, Thomas Robert, Bhrigu-Kumar Lahkar, Issa Moussa, Guillaume Saulière, Thibault Goyallon and Lionel Reveret. *A 3D markerless protocol with action cameras – Key performance indicators in boxing.* 2022. Poster.
- [Pan2009] Sinno Jialin Pan and Qiang Yang. *A survey on transfer learning.* IEEE Transactions on knowledge and data engineering, vol. 22, no. 10, pages 1345–1359, 2009.
- [Patel2021] Priyanka Patel, Chun-Hao P Huang, Joachim Tesch, David T Hoffmann, Shashank Tripathi and Michael J Black. *AGORA: Avatars in geography optimized for regression analysis.* In Proceedings of the

- IEEE/CVF Conference on Computer Vision and Pattern Recognition, pages 13468–13478, 2021.
- [Pavlakos2019] Georgios Pavlakos, Vasileios Choutas, Nima Ghorbani, Timo Bolkart, Ahmed AA Osman, Dimitrios Tzionas and Michael J Black. *Expressive body capture: 3d hands, face, and body from a single image*. In Proceedings of the IEEE/CVF conference on computer vision and pattern recognition, pages 10975–10985, 2019.
- [Pereira2022] Talmo D Pereira, Nathaniel Tabris, Arie Matsliah, David M Turner, Junyu Li, Shruthi Ravindranath, Eleni S Papadoyannis, Edna Normand, David S Deutsch, Z Yan Wang *et al.* *SLEAP: A deep learning system for multi-animal pose tracking*. Nature methods, vol. 19, no. 4, pages 486–495, 2022.
- [Pishchulin2016] Leonid Pishchulin, Eldar Insafutdinov, Siyu Tang, Bjoern Andres, Mykhaylo Andriluka, Peter V Gehler and Bernt Schiele. *Deepcut: Joint subset partition and labeling for multi person pose estimation*. In Proceedings of the IEEE conference on computer vision and pattern recognition, pages 4929–4937, 2016.
- [Pohl2010] Michael B Pohl, Chandra Lloyd and Reed Ferber. *Can the reliability of three-dimensional running kinematics be improved using functional joint methodology?* Gait & Posture, vol. 32, no. 4, pages 559–563, 2010.
- [Qualisys2018] Qualisys. *QTM User Manual*, 2018.
- [Raissi2019] Maziar Raissi, Paris Perdikaris and George E Karniadakis. *Physics-informed neural networks: A deep learning framework for solving forward and inverse problems involving nonlinear partial differential equations*. Journal of Computational physics, vol. 378, pages 686–707, 2019.
- [Rajagopal2016] Apoorva Rajagopal, Christopher L. Dembia, Matthew S. DeMers, Denny D. Delp, Jennifer L. Hicks and Scott L. Delp. *Full-Body Musculoskeletal Model for Muscle-Driven Simulation of Human Gait*. IEEE Transactions on Biomedical Engineering, vol. 63, no. 10, pages 2068–2079, 10 2016.
- [Rauch1965] Herbert E Rauch, F Tung and Charlotte T Striebel. *Maximum likelihood estimates of linear dynamic systems*. AIAA journal, vol. 3, no. 8, pages 1445–1450, 1965.
- [Redmon2016] Joseph Redmon, Santosh Divvala, Ross Girshick and Ali Farhadi. *You only look once: Unified, real-time object detection*. In Proceedings of the IEEE conference on computer vision and pattern recognition, pages 779–788, 2016.
- [Rekant2022] Julie Rekant, Scott Rothenberger and April Chambers. *Inertial measurement unit-based motion capture to replace camera-based systems for assessing gait in healthy young adults: Proceed with caution*. Measurement: Sensors, page 100396, 2022.

- [Rempe2020] Davis Rempe, Leonidas J Guibas, Aaron Hertzmann, Bryan Russell, Ruben Villegas and Jimei Yang. *Contact and Human Dynamics from Monocular Video*. page 27, 2020.
- [Rempe2021] Davis Rempe, Tolga Birdal, Aaron Hertzmann, Jimei Yang, Srinath Sridhar and Leonidas J Guibas. *HuMoR: 3D Human Motion Model for Robust Pose Estimation*. page 23, 2021.
- [Ren2015] Shaoqing Ren, Kaiming He, Ross Girshick and Jian Sun. *Faster r-cnn: Towards real-time object detection with region proposal networks*. Advances in neural information processing systems, vol. 28, 2015.
- [Reveret2020] Lionel Reveret, Sylvain Chapelle, Franck Quaine and Pierre Legreneur. *3D visualization of body motion in speed climbing*. Frontiers in Psychology, vol. 11, page 2188, 2020.
- [Rosenblatt1958] Frank Rosenblatt. *The perceptron: a probabilistic model for information storage and organization in the brain*. Psychological review, vol. 65, no. 6, page 386, 1958.
- [Rumelhart1986] David E Rumelhart, Geoffrey E Hinton and Ronald J Williams. *Learning representations by back-propagating errors*. nature, vol. 323, no. 6088, pages 533–536, 1986.
- [Seethapathi2019] Nidhi Seethapathi, Shaofei Wang, Rachit Saluja, Gunnar Blohm and Konrad P. Kording. *Movement science needs different pose tracking algorithms*. arXiv:1907.10226 [cs, q-bio], 7 2019. arXiv: 1907.10226.
- [Serrancolí2020] Gil Serrancolí, Peter Bogatikov, Joana Palés Huix, Ainoa Forcada Barberà, Antonio J. Sánchez Egea, Jordi Torner Ribé, Samir Kanaan-Izquierdo and Antoni Susín. *Marker-Less Monitoring Protocol to Analyze Biomechanical Joint Metrics During Pedaling*. IEEE Access, vol. 8, pages 122782–122790, 2020. event: IEEE Access.
- [Seth2016] Ajay Seth, Ricardo Matias, António P Veloso and Scott L Delp. *A biomechanical model of the scapulothoracic joint to accurately capture scapular kinematics during shoulder movements*. PloS one, vol. 11, no. 1, page e0141028, 2016.
- [Seth2018] Ajay Seth, Jennifer L. Hicks, Thomas K. Uchida, Ayman Habib, Christopher L. Dembia, James J. Dunne, Carmichael F. Ong, Matthew S. DeMers, Apoorva Rajagopal, Matthew Millard, Samuel R. Hamner, Edith M. Arnold, Jennifer R. Yong, Shrinidhi K. Lakshminikanth, Michael A. Sherman, Joy P. Ku and Scott L. Delp. *OpenSim: Simulating musculoskeletal dynamics and neuromuscular control to study human and animal movement*. PLOS Computational Biology, vol. 14, no. 7, page e1006223, 7 2018.
- [Shapiro1965] Samuel Sanford Shapiro and Martin B Wilk. *An analysis of variance test for normality (complete samples)*. Biometrika, vol. 52, no. 3/4, pages 591–611, 1965.

Bibliography

- [Sheshadri2020] Swathi Sheshadri, Benjamin Dann, Timo Hueser and Hansjoerg Scherberger. *3D reconstruction toolbox for behavior tracked with multiple cameras*. Journal of Open Source Software, vol. 5, no. 45, page 1849, 2020.
- [Slembrouck2020] Maarten Slembrouck, Hiep Luong, Joeri Gerlo, Kurt Schütte, Dimitri Van Cauwelaert, Dirk De Clercq, Benedicte Vanwansele, Peter Veelaert and Wilfried Philips. *Multiview 3D Markerless Human Pose Estimation from OpenPose Skeletons*. In Jacques Blanc-Talon, Patrice Delmas, Wilfried Philips, Dan Popescu and Paul Scheunders, éditeurs, Advanced Concepts for Intelligent Vision Systems, volume 12002, pages 166–178. Springer International Publishing, Cham, 2020.
- [Stenum2021] Jan Stenum, Cristina Rossi and Ryan T. Roemmich. *Two-dimensional video-based analysis of human gait using pose estimation*. PLoS Computational Biology, vol. 17, no. 4, 4 2021.
- [Sun2005] Wei Sun and Jeremy R. Cooperstock. *Requirements for Camera Calibration: Must Accuracy Come with a High Price?* volume 1, pages 356–361. 2005 Seventh IEEE Workshops on Applications of Computer Vision (WACV/MOTION’05) - Volume 1, 1 2005.
- [Takahashi2018] Kosuke Takahashi, Dan Mikami, Mariko Isogawa and Hideaki Kimata. *Human Pose as Calibration Pattern: 3D Human Pose Estimation with Multiple Unsynchronized and Uncalibrated Cameras*. pages 1856–18567, Salt Lake City, UT, USA, 6 2018. 2018 IEEE/CVF Conference on Computer Vision and Pattern Recognition Workshops (CVPRW), IEEE.
- [Topham2021] Luke K Topham, Wasiq Khan, Dhiya Al-Jumeily and Abir Hussain. *Human Body Pose Estimation for Gait Identification: A Comprehensive Survey of Datasets and Models*. ACM Computing Surveys, 2021.
- [Topley2020] Matt Topley and James G. Richards. *A comparison of currently available optoelectronic motion capture systems*. Journal of Biomechanics, vol. 106, page 109820, 6 2020.
- [Trinler2019] Ursula Trinler, Hermann Schwameder, Richard Baker and Nathalie Alexander. *Muscle force estimation in clinical gait analysis using AnyBody and OpenSim*. Journal of Biomechanics, vol. 86, pages 55–63, 3 2019.
- [Tsiminaki2014] Vagia Tsiminaki, Jean-Sébastien Franco and Edmond Boyer. *High resolution 3d shape texture from multiple videos*. In Proceedings of the IEEE Conference on Computer Vision and Pattern Recognition, pages 1502–1509, 2014.
- [Tsushima2003] Hitoshi Tsushima, Meg E Morris and Jennifer McGinley. *Test-Retest Reliability and Inter-Tester Reliability of Kinematic Data from a Three-Dimensional Gait Analysis System*. Journal of the Japanese Physical Therapy Association, vol. 6, no. 1, pages 9–17, 2003.
- [Uhlrich2022] Scott D. Uhlrich, Antoine Falisse, Łukasz Kidziński, Julie Muccini, Michael Ko, Akshay S. Chaudhari, Jennifer L. Hicks and Scott L.

- Delp. *OpenCap: 3D human movement dynamics from smartphone videos*. page 2022.07.07.499061, Jul 2022.
- [Uijlings2013] Jasper RR Uijlings, Koen EA Van De Sande, Theo Gevers and Arnold WM Smeulders. *Selective search for object recognition*. International journal of computer vision, vol. 104, no. 2, pages 154–171, 2013.
- [Varol2017] GÜL Varol, Javier Romero, Xavier Martin, Naureen Mahmood, Michael J. Black, Ivan Laptev and Cordelia Schmid. *Learning from Synthetic Humans*. 2017 IEEE Conference on Computer Vision and Pattern Recognition (CVPR), pages 4627–4635, 7 2017. arXiv: 1701.01370.
- [Viswakumar2019] Aditya Viswakumar, Venkateswaran Rajagopalan, Tathagata Ray and Chandu Parimi. *Human Gait Analysis Using OpenPose*. pages 310–314. 2019 Fifth International Conference on Image Information Processing (ICIIP), 11 2019. ISSN: 2640-074X.
- [Wade2021] Logan Wade, Laurie Needham, Murray Evans, Steffi Colyer, Darren Cosker, James Bilzon and Polly McGuigan. *Application of deep learning-based pose estimation methods for clinical gait outcome measures*. In Proceedings of the Congress of the International Society of Biomechanics, Stockholm, Sweden, pages 25–29, 2021.
- [Wang2021a] Jiahang Wang, Sheng Jin, Wentao Liu, Weizhong Liu, Chen Qian and Ping Luo. *When human pose estimation meets robustness: Adversarial algorithms and benchmarks*. In Proceedings of the IEEE/CVF Conference on Computer Vision and Pattern Recognition, pages 11855–11864, 2021.
- [Wang2021b] Jinbao Wang, Shujie Tan, Xiantong Zhen, Shuo Xu, Feng Zheng, Zhenyu He and Ling Shao. *Deep 3D human pose estimation: A review*. Computer Vision and Image Understanding, page 103225, 5 2021.
- [Wang2022a] Chien-Yao Wang, Alexey Bochkovskiy and Hong-Yuan Mark Liao. *YOLOv7: Trainable bag-of-freebies sets new state-of-the-art for real-time object detectors*. arXiv preprint arXiv:2207.02696, 2022.
- [Wang2022b] Wenming Wang, Kaixiang Zhang, Haopan Ren, Dejian Wei, Yanyan Gao and Juncheng Liu. *UULPN: An ultra-lightweight network for human pose estimation based on unbiased data processing*. Neurocomputing, vol. 480, pages 220–233, 2022.
- [Warmenhoven2018] John Warmenhoven, Andrew Harrison, Mark A. Robinson, Jos Vannerenberghem, Norma Bargary, Richard Smith, Stephen Cobley, Conny Draper, Cyril Donnelly and Todd Pataky. *A force profile analysis comparison between functional data analysis, statistical parametric mapping and statistical non-parametric mapping in on-water single sculling*. Journal of Science and Medicine in Sport, vol. 21, no. 10, pages 1100–1105, 10 2018.

Bibliography

- [Windt2020] Johann Windt, Kerry MacDonald, David Taylor, Bruno D Zumbo, Ben C Sporer and David T Martin. *“To tech or not to tech?” A critical decision-making framework for implementing technology in sport.* Journal of Athletic Training, vol. 55, no. 9, pages 902–910, 2020.
- [Wood2021] Erroll Wood, Tadas Baltrušaitis, Charlie Hewitt, Sebastian Dziadzio, Thomas J Cashman and Jamie Shotton. *Fake it till you make it: face analysis in the wild using synthetic data alone.* In Proceedings of the IEEE/CVF international conference on computer vision, pages 3681–3691, 2021.
- [Xiang2019] Donglai Xiang, Hanbyul Joo and Yaser Sheikh. *Monocular total capture: Posing face, body, and hands in the wild.* In Proceedings of the IEEE/CVF conference on computer vision and pattern recognition, pages 10965–10974, 2019.
- [Xu2020a] Hongyi Xu, Eduard Gabriel Bazavan, Andrei Zanfir, William T Freeman, Rahul Sukthankar and Cristian Sminchisescu. *Ghum & ghuml: Generative 3d human shape and articulated pose models.* In Proceedings of the IEEE/CVF Conference on Computer Vision and Pattern Recognition, pages 6184–6193, 2020.
- [Xu2020b] Jingwei Xu, Zhenbo Yu, Bingbing Ni, Jiancheng Yang, Xiaokang Yang and Wenjun Zhang. *Deep kinematics analysis for monocular 3d human pose estimation.* In Proceedings of the IEEE/CVF Conference on computer vision and Pattern recognition, pages 899–908, 2020.
- [Xu2021] Yan Xu, Yu-Jhe Li, Xinshuo Weng and Kris Kitani. *Wide-baseline multi-camera calibration using person re-identification.* In Proceedings of the IEEE/CVF Conference on Computer Vision and Pattern Recognition, pages 13134–13143, 2021.
- [Xu2022] Lumin Xu, Sheng Jin, Wentao Liu, Chen Qian, Wanli Ouyang, Ping Luo and Xiaogang Wang. *ZoomNAS: Searching for Whole-body Human Pose Estimation in the Wild.* IEEE Transactions on Pattern Analysis and Machine Intelligence, 2022.
- [Zago2020] Matteo Zago, Matteo Luzzago, Tommaso Marangoni, Mariolino De Cecco, Marco Tarabini and Manuela Galli. *3D Tracking of Human Motion Using Visual Skeletonization and Stereoscopic Vision.* Frontiers in Bioengineering and Biotechnology, vol. 8, 2020.
- [Zeni2008] J. A. Zeni, J. G. Richards and J. S. Higginson. *Two simple methods for determining gait events during treadmill and overground walking using kinematic data.* Gait and Posture, vol. 27, no. 4, pages 710–714, 5 2008.
- [Zhang2000] Zhengyou Zhang. *A flexible new technique for camera calibration.* IEEE Transactions on pattern analysis and machine intelligence, vol. 22, no. 11, pages 1330–1334, 2000.
- [Zhang2013] Jun-Tian Zhang, Alison C Novak, Brenda Brouwer and Qingguo Li. *Concurrent validation of Xsens MVN measurement of lower limb joint angular kinematics.* Physiological measurement, vol. 34, no. 8, page N63, 2013.

- [Zhang2020] Zhe Zhang, Chunyu Wang, Wenhui Qin and Wenjun Zeng. *Fusing wearable IMUs with multi-view images for human pose estimation: A geometric approach*. In Proceedings of the IEEE/CVF Conference on Computer Vision and Pattern Recognition, pages 2200–2209, 2020.
- [Zheng2022] Ce Zheng, Wenhan Wu, Taojiannan Yang, Sijie Zhu, Chen Chen, Ruixu Liu, Ju Shen, Nasser Kehtarnavaz and Mubarak Shah. *Deep learning-based human pose estimation: A survey*. arXiv, 2022.

List of Figures

1.1	Principles of marker-based motion capture. (Figure 1.1a) presents the functioning of an opto-electronic camera. (Figure 1.1b) shows how a network of calibrated motion capture cameras helps obtaining joint angles.	4
1.2	IMUs are placed on the subject's limbs. The orientation of the limbs is then used to infer the posture of the subject.	5
1.3	A depth-field camera (RGB-D) projects infrared modulated light onto the subject's body. The time it takes for the light to be reflected to the camera sensor (time of flight) depends on distance, and gives access to the depth of the scene. Older RGB-D cameras use structured light rather than time of flight calculations to infer depth.	6
1.4	The search for “deep learning 3D human pose estimation” (dots) fits an exponential curve (line). The search produced less than 100 results until 2015, and is now well over a 1,000 per year.	7
1.5	2D pose estimation by OpenPose. Image courtesy of [Cao2019].	8
2.1	Different types of image analysis. (a) Whole image classification, (b) Object detection and localization, (c) Instance segmentation and shape extraction, (d) Keypoint detection.	15
2.2	The artificial neuron (b) has been modeled after the natural neuron (a). Inputs and weights act as the total nervous influx firing the dendrites. The collected values are summed, and a signal is activated if a threshold is overcome, as the soma does in a natural neuron. The output signal is conveyed the axon in a natural neuron. (b) In the case of a perceptron, the neuron adjusts its weights to minimize the error between the predicted and the expected output. It can be used as a classifier, which outputs class 1 or class 0 depending on the inputs. (c) A dense (fully connected) neural network with one intermediate layer and backpropagation can solve any non-linearly separable classification.	17
2.3	Classification of athletes as "good" (black dot) or "bad" (circle) according to their Force-Velocity results. Weights are adjusted (grey lines), until the perceptron classifies athletes correctly (black line.)	19
2.4	Single layer artificial neural networks such as the perceptron can only classify linearly separable data. (a) is linearly separable. (b) is not linearly separable. However, data are contained in an ellipse. The equation of an ellipse is of the form $a \times x^2 + b \times y^2 = 1$, so if we transform the feature variables into $X = x^2$ and $Y = y^2$, the data become linearly separable. (c) is equivalent to a fundamental XOR gate, and is not linearly separable, which was part of the reasons for the first AI winter. It can either be solved by combining several layers of artificial neurons, or by complex kernel tricks which map the data from the original space into a higher dimensional space where they become linearly separable. (d) is possibly not separable at all. AI: Artificial Intelligence. XOR: Exclusive OR.	20

2.5	A simplified convolutional neural network (CNN.) A convolutional layer consists in a series of filters running across the input image, and producing feature maps, which are then downsampled by pooling. Filters become more and more elaborated along layers, and produce feature maps which look like whole object parts. Filters and weights are randomly initialized at first, and then are adjusted by back-propagation. After the convolutional layers, the feature maps are flattened to produce a 1D vector, which is then processed by dense layers, and finally a softmax layer computes a probability for the image to correspond to each available class.	21
2.6	The body_25b OpenPose model is more accurate than the default body_25 one. As an example, the left knee is slightly misplaced on the default model. Keypoint definition and order also differ between both models.	23
3.1	Pose2Sim full pipeline: (1) 2D keypoint detection; (2.1) Camera calibration; (2.1-2.4) Tracking of the person of interest, Triangulating of keypoint coordinates; and Filtering; (3) Constraining the 3D coordinates to an individually scaled, physically consistent OpenSim skeletal model.	29
3.2	Filtered results. Each keypoint trajectory is displayed in a different tab.	31
3.3	An example .trc file of triangulated keypoint coordinates, directly usable in OpenSim.	31
3.4	First steps of Pose2Sim pipeline in Python. Calibration can either be done from a checkerboard, or by simply converting a Qualisys calibration file. Note that the functions can be used without any arguments if the Config.toml file is left in the default location.	32
3.5	At the end of the demonstration, you should have a skeleton balancing on a beam in OpenSim.	33
3.6	The Pose2Sim workflow, along with some optional utilities provided in the package.	34
3.7	The experimental body_25b OpenPose model is more accurate than the default body_25 one. See how the left knee is slightly misplaced on the default model. The keypoint definition differs between both models.	35
3.8	Triangulated anatomical markers and clusters (dark green), calculated joint centers (light green), and OpenPose body_25b keypoints (pink) on a textured mesh. OpenPose's eyes and ears keypoints were excluded. Mesh opacity was set to 0.5 in order to make all points visible. This view made it possible to precisely place OpenPose triangulated keypoints on the OpenSim model.	38
3.9	The MPP2SOS Blender add-on uses Pose2Sim for realistic 3D markerless animation	41
3.10	The Maya-Mocap add-on (a-b), and the tool set that it should eventually provide (c).	42
4.1	The pinhole camera model permits a correspondence between image coordinates and object coordinates. f: focal distance, D: object to camera distance, Err^{Img} : error on image plane, Err^{Obj} : error on object plane. f and Err^{Img} are usually expressed in pixels, while D and Err^{Obj} are expressed in meters.	48
4.2	The Kinovis room allows for the capture of 3D textured meshes. These meshes are placed in a virtual environment, and then filmed from virtual cameras.	49
4.3	To smooth out sharp edges due to compositing, we applied a 3×3 pixel Gaussian blur to the videos filmed from our virtual scene.	50
4.4	The image under poor image quality (Im) conditions. A Gaussian blur (11×11 px) was applied, and a 0.5 gamma compression made the image darker.	52
4.5	OpenSim inverse kinematics on cycling (C). Model markers are pink; experimental markers are blue.	54

4.6 Comparison between our markerless results (black line: mean stride-to-stride results for our subject) and the normative marker-based database (green line and area: mean and standard deviation across 14 young, healthy, male subjects). Mean absolute error (MAE) and Pearson correlation coefficient (r) are represented.	57
4.7 Joint angle means (solid line) and standard deviations (shaded area) from the eight captured cycles of walking. Reference condition (Ref) is black; degraded image quality (Im) is blue; four cameras instead of eight (4c) is purple; degraded calibration (Cal) is yellow. Pearson's correlation coefficient (r) and mean absolute error (MAE) between Ref and Im, 4c, Cal are reported. Paired t-tests along time were computed by SPM-1D and are represented as bar plots above the curves: a color rectangle means that there was a cluster of statistically significant differences ($\alpha = 0.05$) at that moment. Running and cycling figures can be found in the Supplementary Material.	59
5.1 Pose2Sim (cyan) and marker-based (black) lower-body joint angles for the walking task. Coefficient of multiple correlation (CMC) is indicated, and broken down into, respectively, Pearson's coefficient (r) for correlation assessment, range of motion errors (ROM_{err}) for gain, and overall mean errors ($Mean_{err}$) for offset. Mean error and standard deviations are also represented at the bottom of the graphics. See Appendix B for running and cycling results, and for sacro-lumbar and upper-body results.	71
5.2 Bland–Altman analysis of lower-body joint angle errors for the walking task. Mean bias is represented as a horizontal solid, bold line, and 95% limits of agreement are represented as dotted lines. See Appendix B for running and cycling results, and for sacro-lumbar and upper-body results.	73
A.1 Joint angle means (solid line) and standard deviations (shaded area) from the nine captured cycles of running. Reference condition (Ref) is black; degraded image quality (Im) is blue; four cameras instead of eight (4c) is purple; degraded calibration (Cal) is yellow. Pearson's correlation coefficient (r) and mean absolute error (MAE) between Ref and Im, 4c, Cal were calculated. Paired t-tests along time were computed by SPM-1D and are represented as bar plots above the curves: a color rectangle means that there was a cluster of statistically significant differences ($\alpha = 0.05$) at that moment.	XXVIII
A.2 Joint angle means (solid line) and standard deviations (shaded area) from the 15 captured cycles of cycling. Reference condition (Ref) is black; degraded image quality (Im) is blue; four cameras instead of eight (4c) is purple; degraded calibration (Cal) is yellow. Pearson's correlation coefficient (r) and mean absolute error (MAE) between Ref and Im, 4c, Cal were calculated. Paired t-tests along time were computed by SPM-1D and are represented as bar plots above the curves: a color rectangle means that there was a cluster of statistically significant differences ($\alpha = 0.05$) at that moment.	XXIX
B.1 Pose2Sim (cyan) and marker-based (black) lower-body joint angles for the running task. Coefficient of multiple correlation (CMC) is indicated, and broken down into, respectively, Pearson's coefficient (r) for correlation assessment, range of motion errors (ROM_{err}) for gain, and overall mean errors ($Mean_{err}$) for offset. Mean error and standard deviations are also represented at the bottom of the graphics.	XXXI
B.2 Bland–Altman analysis of lower-body joint angle errors for the running task. Mean bias is represented as a horizontal solid, bold line, and 95% limits of agreement are represented as dotted lines.	XXXII

B.3	Pose2Sim (cyan) and marker-based (black) lower-body joint angles for the cycling task. Coefficient of multiple correlation (CMC) is indicated, and broken down into, respectively, Pearson's coefficient (<i>r</i>) for correlation assessment, range of motion errors (ROM_{err}) for gain, and overall mean errors ($Mean_{err}$) for offset. Mean error and standard deviations are also represented at the bottom of the graphics.	XXXIII
B.4	Bland–Altman analysis of lower-body joint angle errors for the cycling task. Mean bias is represented as a horizontal solid, bold line, and 95% limits of agreement are represented as dotted lines.	XXXIV
B.5	Pose2Sim (cyan) and marker-based (black) sacro-lumbar and upper-body joint angles for the walking task. Coefficient of multiple correlation (CMC) is indicated, and broken down into, respectively, Pearson's coefficient (<i>r</i>) for correlation assessment, range of motion errors (ROM_{err}) for gain, and overall mean error ($Mean_{err}$) for offset. Mean error and standard deviations are also represented at the bottom of the graphics.	XXXVI
B.6	Bland–Altman analysis of sacro-lumbar and upper-body joint angle errors for the walking task. Mean bias is represented as a horizontal solid, bold line, and 95% limits of agreement are represented as dotted lines.	XXXVII
B.7	Pose2Sim (cyan) and marker-based (black) sacro-lumbar and upper-body joint angles for the running task. Coefficient of multiple correlation (CMC) is indicated, and broken down into, respectively, Pearson's coefficient (<i>r</i>) for correlation assessment, range of motion errors (ROM_{err}) for gain, and overall mean error ($Mean_{err}$) for offset. Mean error and standard deviations are also represented at the bottom of the graphics.	XXXVIII
B.8	Bland–Altman analysis of sacro-lumbar and upper-body joint angle errors for the running task. Mean bias is represented as a horizontal solid, bold line, and 95% limits of agreement are represented as dotted lines.	XXXIX
B.9	Pose2Sim (cyan) and marker-based (black) sacro-lumbar and upper-body joint angles for the cycling task. Coefficient of multiple correlation (CMC) is indicated, and broken down into, respectively, Pearson's coefficient (<i>r</i>) for correlation assessment, range of motion errors (ROM_{err}) for gain, and overall mean errors ($Mean_{err}$) for offset. Mean error and standard deviations are also represented at the bottom of the graphics.	XL
B.10	Bland–Altman analysis of sacro-lumbar and upper-body joint angle errors for the cycling task. Mean bias is represented as a horizontal solid, bold line, and 95% limits of agreement are represented as dotted lines.	XLI

List of Tables

1.1	Pros and cons in state-of-the-art approaches for human motion analysis. The multi-person prospect is not addressed, as it can be available with all approaches, but it is not always. IMU: Inertial Measurement Unit. N/A: Not Applicable. kin.: kinematic. RGB-D: red-green-blue-depth.	12
4.1	Descriptive statistics on the triangulation step performed by Pose2Sim from Open-Pose body_25b model. Mean absolute reprojection error and mean number of excluded cameras were calculated over time. Mean (mean), standard deviation (std), and maximum (max) in each of these variables are displayed. Walking, running, and cycling tasks were investigated in each four conditions: reference (Ref), poor image quality (Im), four cameras instead of eight (4c), and calibration errors (Cal).	55
4.2	Descriptive statistics on the inverse kinematics step performed by OpenSim with a full body model adapted from Rajagopal's. Root mean square (RMS) errors between experimental and model markers were calculated over all markers. Mean, standard deviation (std), and maximum (max) are displayed. Dead center refers to the phase where the crank is near the vertical position.	56
4.3	Summary of angles statistics, averaged for all joints. Each condition is represented: reference condition (Ref), degraded image quality (Im), four cameras instead of eight (4c), degraded calibration (Cal). Comparisons between each Im, 4c, Cal conditions, and Ref are accounted for with standard deviation (std), the standard deviation ratio (std/stdref), the Pearson's correlation coefficient (r), and the mean absolute error (MAE).	57
4.4	Stride-to-stride standard deviations of lower-body angles. Comparison between our markerless approach, and a marker-based one (averaged over 18 young subjects). * Ankle subtalar angle is assimilated to an abduction/adduction angle.	58
4.5	Summary of angles statistics in the three rotation planes, averaged over all joints (n = 5, 3, 2 for Flexion/Extension, Abduction/Adduction, and Internal/External Rotation, respectively.). All conditions are represented: degraded image quality (Im), four cameras instead of eight (4c), and degraded calibration (Cal). These conditions were compared to the reference one (Ref) by calculating the ratio of standard deviation (std/stdref), the Pearson's correlation coefficient (r), and the mean absolute error (MAE). *Ankle subtalar angle is assimilated to an abduction/adduction angle.	60
5.1	RMSE between experimental and theoretical markers during OpenSim inverse kinematics, for both marker-based and Pose2Sim models.	70

5.2	Summary of comparisons between Pose2Sim and marker-based angle waveforms. A specific formulation of the Coefficient of Multiple Correlation (CMC) was used, specifically designed to compare different protocols or measurement systems. CMC jointly evaluates correlation, gain, and offset, which were respectively assessed with r-Pearson's coefficient, range of motion errors (ROM_{err}), and mean errors ($Mean_{err}$). *Significant at 5% level. ¹ Despite ankle subtalar angle combines abduction/adduction and internal/external rotation, it is hereafter reported in the abduction/adduction column.	72
5.3	Bland–Altman analysis results of 3D angle errors between Pose2Sim analysis and the reference marker-based one. Mean errors ($Mean_{err}$) and 95% limits of agreement (LoA) are represented. *Although ankle subtalar angle combines abduction/adduction and internal/external rotation, it is hereafter reported in the abduction/adduction column.	72
5.4	Pose2Sim results compared to Theia3D [Kanko2021b] and to Xsens [Zhang2013] in the walking task. Root-mean-square error (RMSE), mean error (Meanerr), and range of motion (ROM) are examined. Theia3D's ROM results were approximated from reported graphics along the flexion/extension degree of freedom. Both studies to which we compared our results involved a different setup (participants, cameras, protocol, etc.), therefore the differences cannot be totally attributed to the different technologies (markerless or IMU) nor to the different algorithm (Pose2Sim or Theia3D). * Although ankle subtalar angle combines abduction/adduction and internal/external rotation, it is hereafter reported in the abduction/adduction column.	74

A

Appendix A on Robustness assessment

Supplementary figures for Chapter 4 on [Robustness assessment](#), for the running and cycling tasks.

All details on methods and results are provided in the fore-mentioned chapter.

Contents

A.1 Robustness: Running task results	XXVIII
A.2 Robustness: Cycling task results	XXIX

A.1 Robustness: Running task results

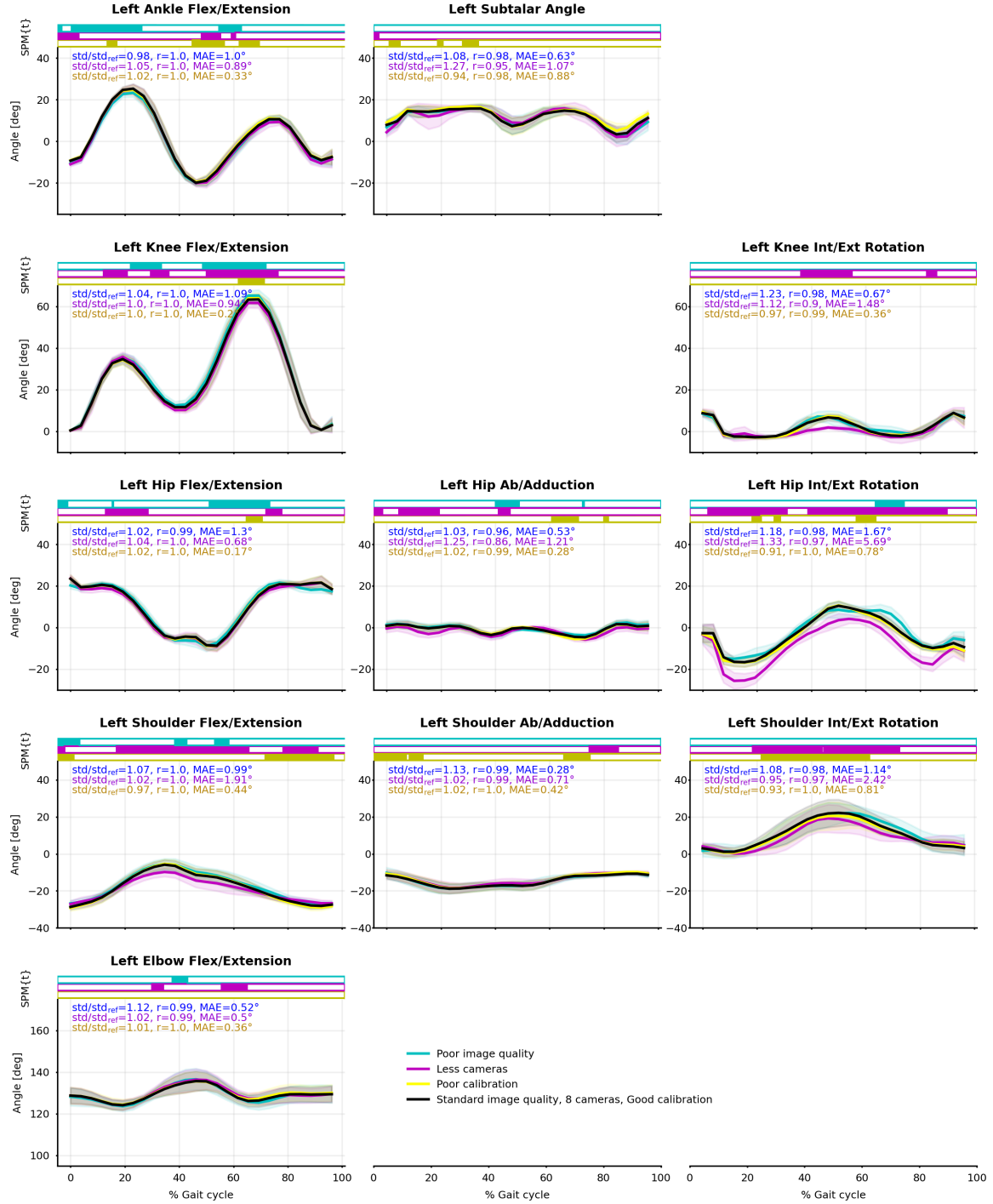


Figure A.1: Joint angle means (solid line) and standard deviations (shaded area) from the nine captured cycles of running. Reference condition (Ref) is black; degraded image quality (Im) is blue; four cameras instead of eight (4c) is purple; degraded calibration (Cal) is yellow. Pearson's correlation coefficient (r) and mean absolute error (MAE) between Ref and Im, 4c, Cal were calculated. Paired t-tests along time were computed by SPM-1D and are represented as bar plots above the curves: a color rectangle means that there was a cluster of statistically significant differences ($\alpha = 0.05$) at that moment.

A.2 Robustness: Cycling task results

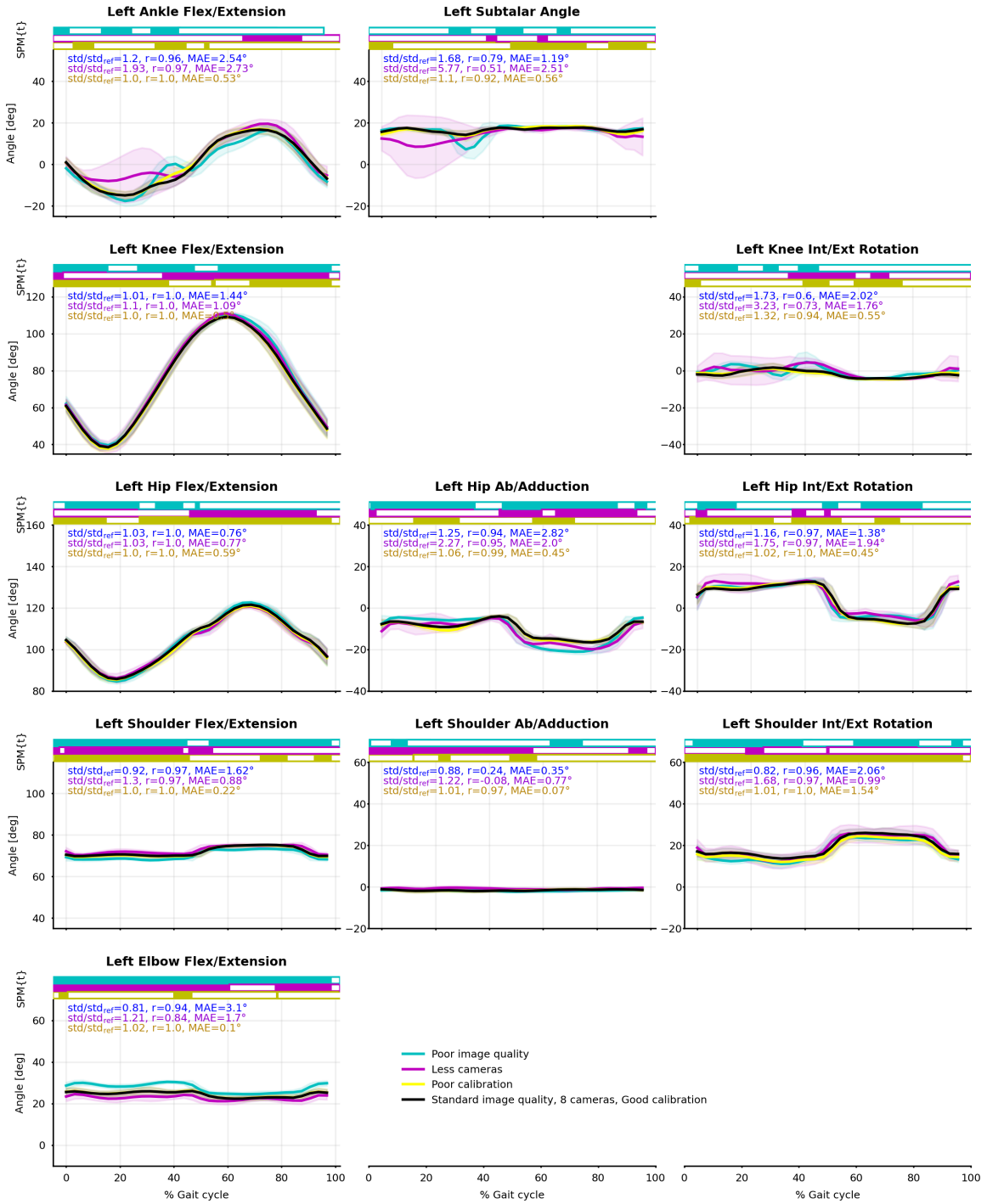


Figure A.2: Joint angle means (solid line) and standard deviations (shaded area) from the 15 captured cycles of cycling. Reference condition (Ref) is black; degraded image quality (Im) is blue; four cameras instead of eight (4c) is purple; degraded calibration (Cal) is yellow. Pearson's correlation coefficient (r) and mean absolute error (MAE) between Ref and Im, 4c, Cal were calculated. Paired t-tests along time were computed by SPM-1D and are represented as bar plots above the curves: a color rectangle means that there was a cluster of statistically significant differences ($\alpha = 0.05$) at that moment.

B

Appendix B on Accuracy assessment

Supplementary figures for Chapter 5 on [Accuracy assessment](#), for the lower-body analysis of the running and cycling tasks, and for the upper-body analysis of all three tasks.

All details on methods and results on the lower-body are provided in the forementioned chapter. Results and discussion on the upper-body are debated section [B.2](#).

Contents

B.1	Lower-body results for the running and cycling tasks	XXXI
B.1.1	Accuracy: Running task results	XXXI
B.1.2	Accuracy: Cycling task results	XXXIII
B.2	Sacro-lumbar and upper-body results for all tasks	XXXV
B.2.1	Accuracy: Upper-body results for the walking task	XXXVI
B.2.2	Accuracy: Upper-body results for the running task	XXXVIII
B.2.3	Accuracy: Upper-body results for the cycling task	XL

B.1 Lower-body results for the running and cycling tasks

Lower-body graphs are provided on Figure B.1 and on Figure B.2 for the running task, and on Figure B.3 and on Figure B.4. However, all results are discussed in the main body of the article on [Accuracy assessment](#).

B.1.1 Accuracy: Running task results

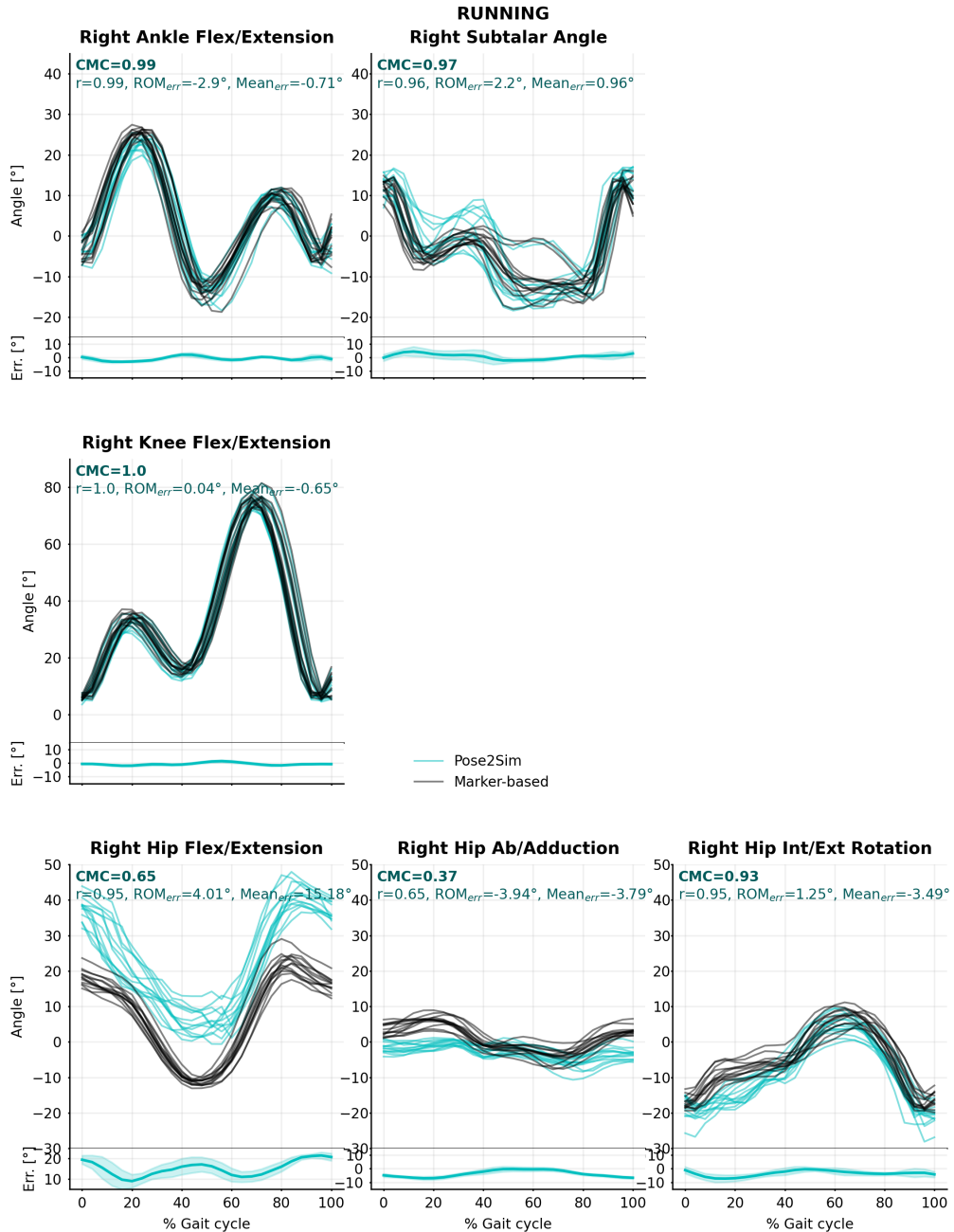


Figure B.1: Pose2Sim (cyan) and marker-based (black) lower-body joint angles for the running task. Coefficient of multiple correlation (CMC) is indicated, and broken down into, respectively, Pearson's coefficient (r) for correlation assessment, range of motion errors (ROM_{err}) for gain, and overall mean errors ($Mean_{err}$) for offset. Mean error and standard deviations are also represented at the bottom of the graphics.

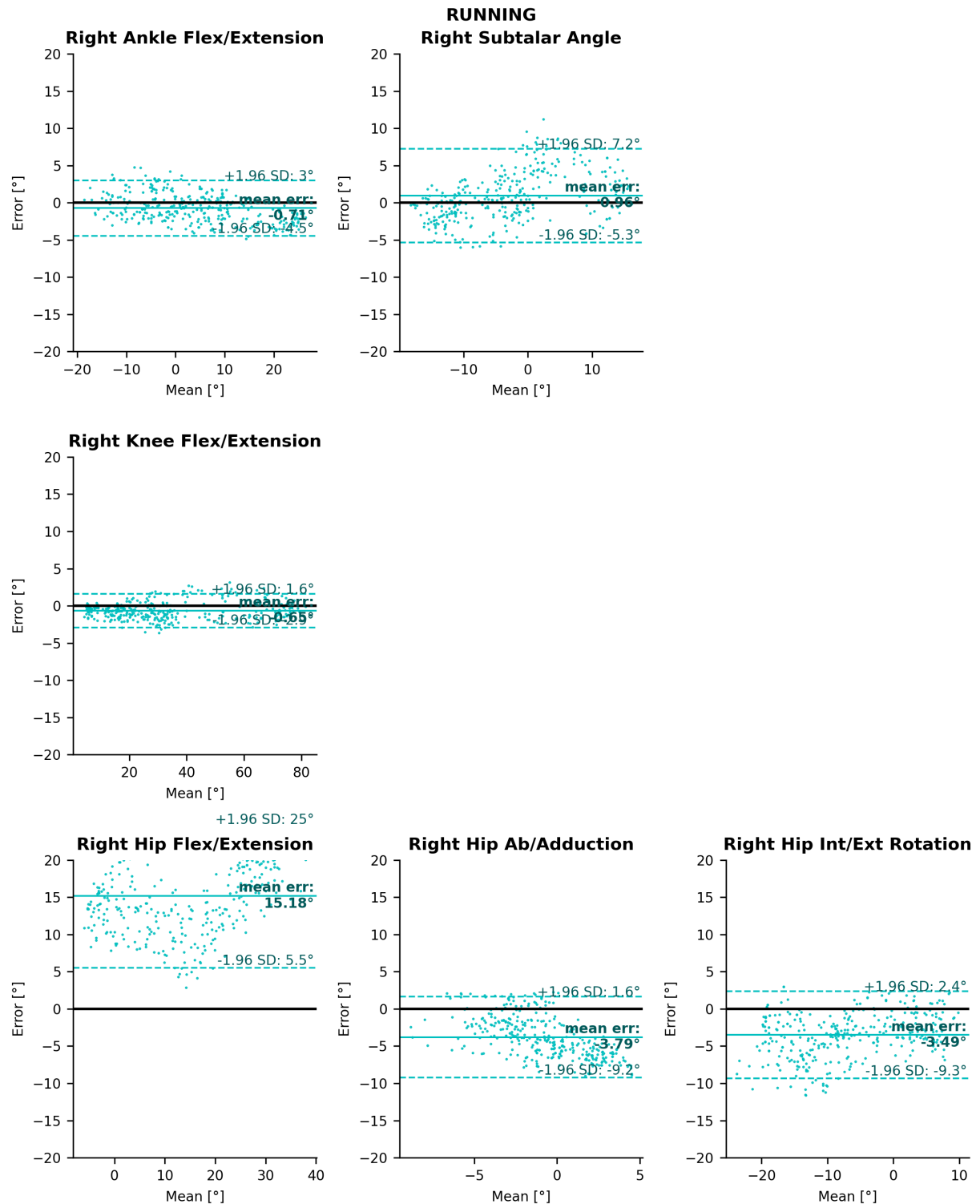


Figure B.2: Bland–Altman analysis of lower-body joint angle errors for the running task. Mean bias is represented as a horizontal solid, bold line, and 95% limits of agreement are represented as dotted lines.

B.1.2 Accuracy: Cycling task results

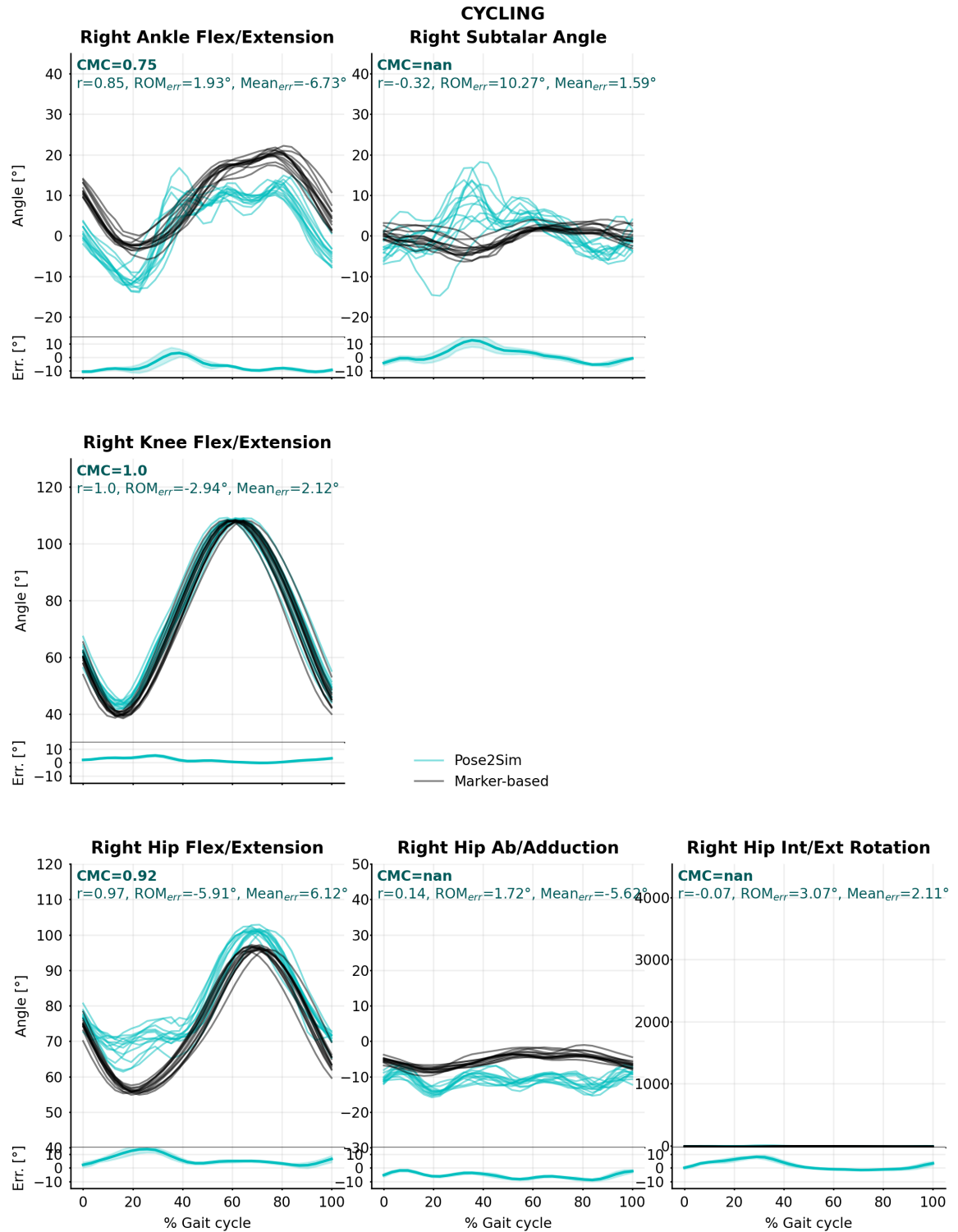


Figure B.3: Pose2Sim (cyan) and marker-based (black) lower-body joint angles for the cycling task. Coefficient of multiple correlation (CMC) is indicated, and broken down into, respectively, Pearson's coefficient (r) for correlation assessment, range of motion errors (ROM_{err}) for gain, and overall mean errors ($Mean_{err}$) for offset. Mean error and standard deviations are also represented at the bottom of the graphics.

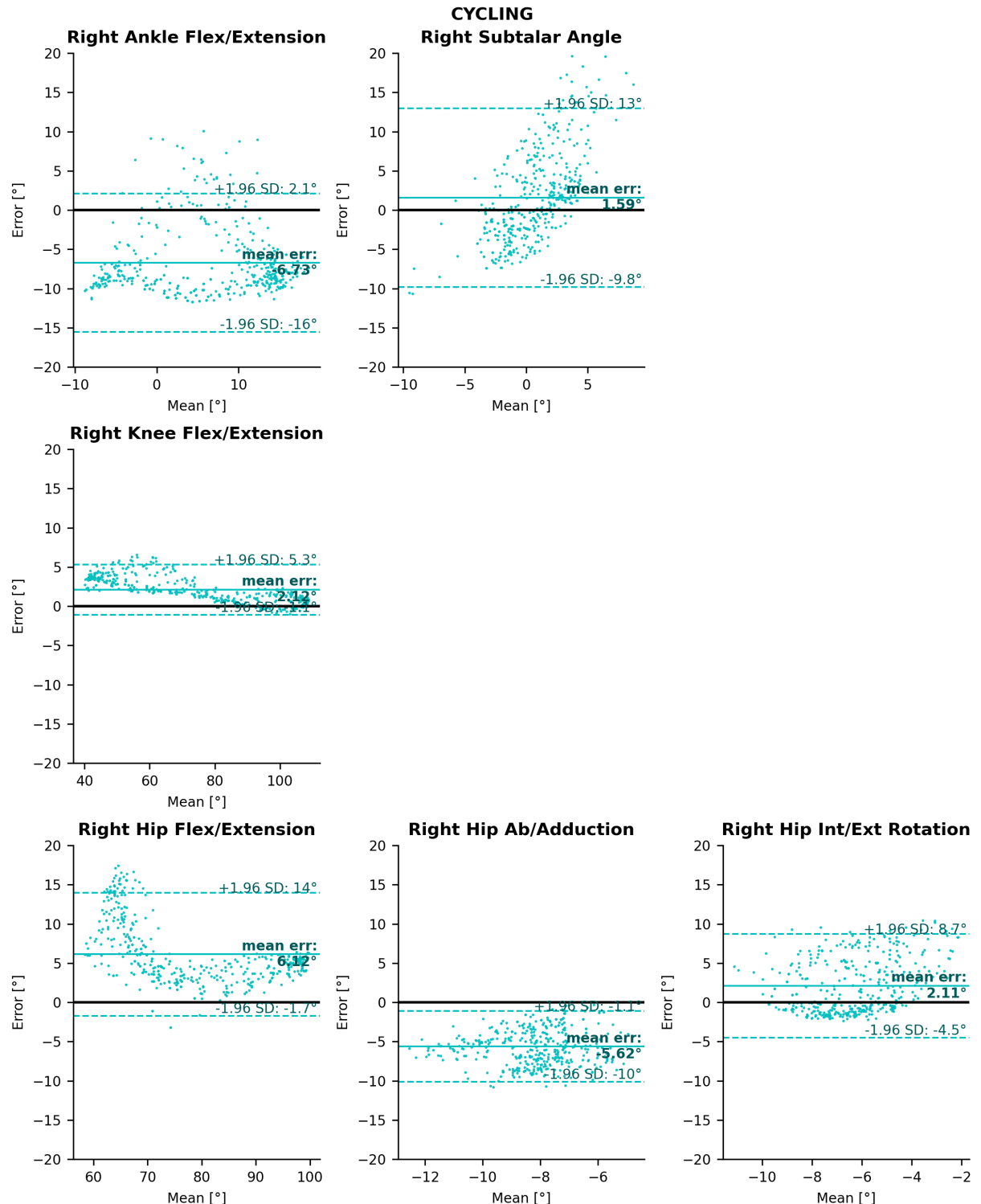


Figure B.4: Bland–Altman analysis of lower-body joint angle errors for the cycling task. Mean bias is represented as a horizontal solid, bold line, and 95% limits of agreement are represented as dotted lines.

B.2 Sacro-lumbar and upper-body results for all tasks

Although the article focused on lower limb kinematics, we ran the same analysis on sacro-lumbar, elbow, and shoulder joints for all three tasks (Figure B.5 and Figure B.6 for walking, Figure B.7 and Figure B.8 for running, and Figure B.9 and Figure B.10 for cycling). The OpenPose model we used does not allow for the capture of wrist deviation or pronation/supination, or of any hand or finger movement.

Results were generally less good than in the lower body, especially on sacro-lumbar flexion/extension, for which all CMC values were complex. This can be attributed both to the lack of OpenPose keypoints in this area, and to the simplicity of the OpenSim model in the upper-body part. Indeed, currently all pelvis, lumbar, and thoracic angles are solely determined by the detection of the hip keypoints on the lower part, and of the shoulder and neck keypoints on the upper part. Moreover, the skeletal model did not allow for any scapulo-thoracic degree of freedom. In addition to the sacro-lumbar joint, upper-body Pearson's correlation coefficients were mostly very good (>0.85) in most planes in walking and running. The range of motion error remained below 1° for shoulder and elbow angles in walking, while it reached almost 5° in the shoulder and 2° in the elbow in running. The mean error in the sagittal plane was below 1° in the shoulder angle in walking, but it reached 10° in the elbow; conversely, in running it reached 9° in the shoulder but remained under 1° in the elbow. In cycling, upper-body Pose2Sim angles were mostly not correlated to marker-based ones, and ROM errors and mean errors were much worse than in other tasks. Moreover, the Bland–Altman analysis showed that the data is heteroscedastic: the spread and magnitude of the errors varied as the joint angle evolved.

In conclusion, Pose2Sim does not evaluate some anatomical joint angles in the upper body, and is generally less accurate than for the lower body. This is mostly due to the lack of keypoints OpenPose detects. To date, OpenPose offers hand and face models but no detailed model of the upper limb exists. Pose2Sim could be used with other pose estimation algorithms, including custom ones leveraging DeepLabCut [Mathis2018, Lauer2022], for example, although it would involve manually labeling a large training dataset. This would enable the use of a more anatomically realistic kinematic model, such as the one proposed by [Seth2016] for the shoulder girdle.

B.2.1 Accuracy: Upper-body results for the walking task

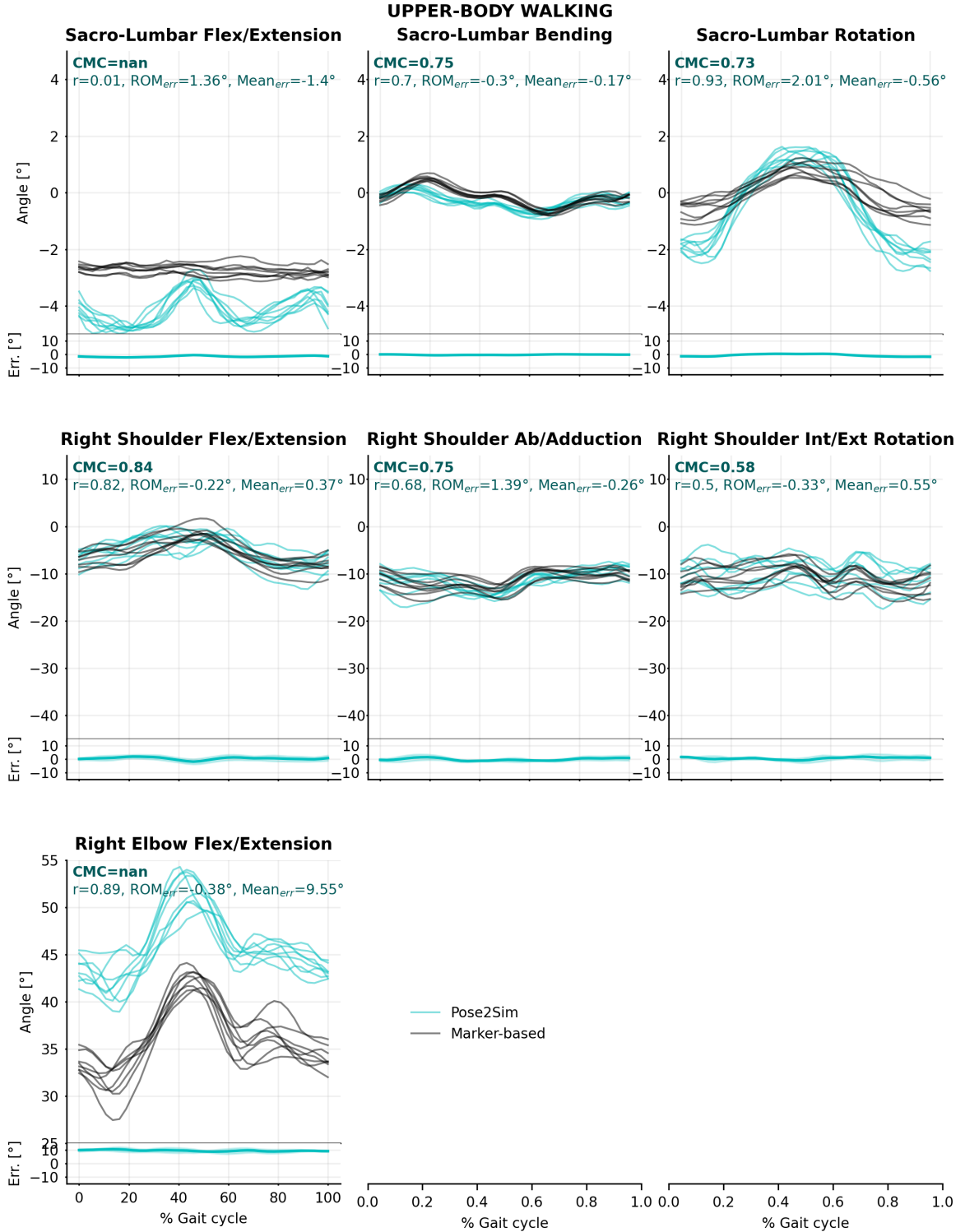


Figure B.5: Pose2Sim (cyan) and marker-based (black) sacro-lumbar and upper-body joint angles for the walking task. Coefficient of multiple correlation (CMC) is indicated, and broken down into, respectively, Pearson's coefficient (r) for correlation assessment, range of motion errors (ROM_{err}) for gain, and overall mean error ($Mean_{err}$) for offset. Mean error and standard deviations are also represented at the bottom of the graphics.

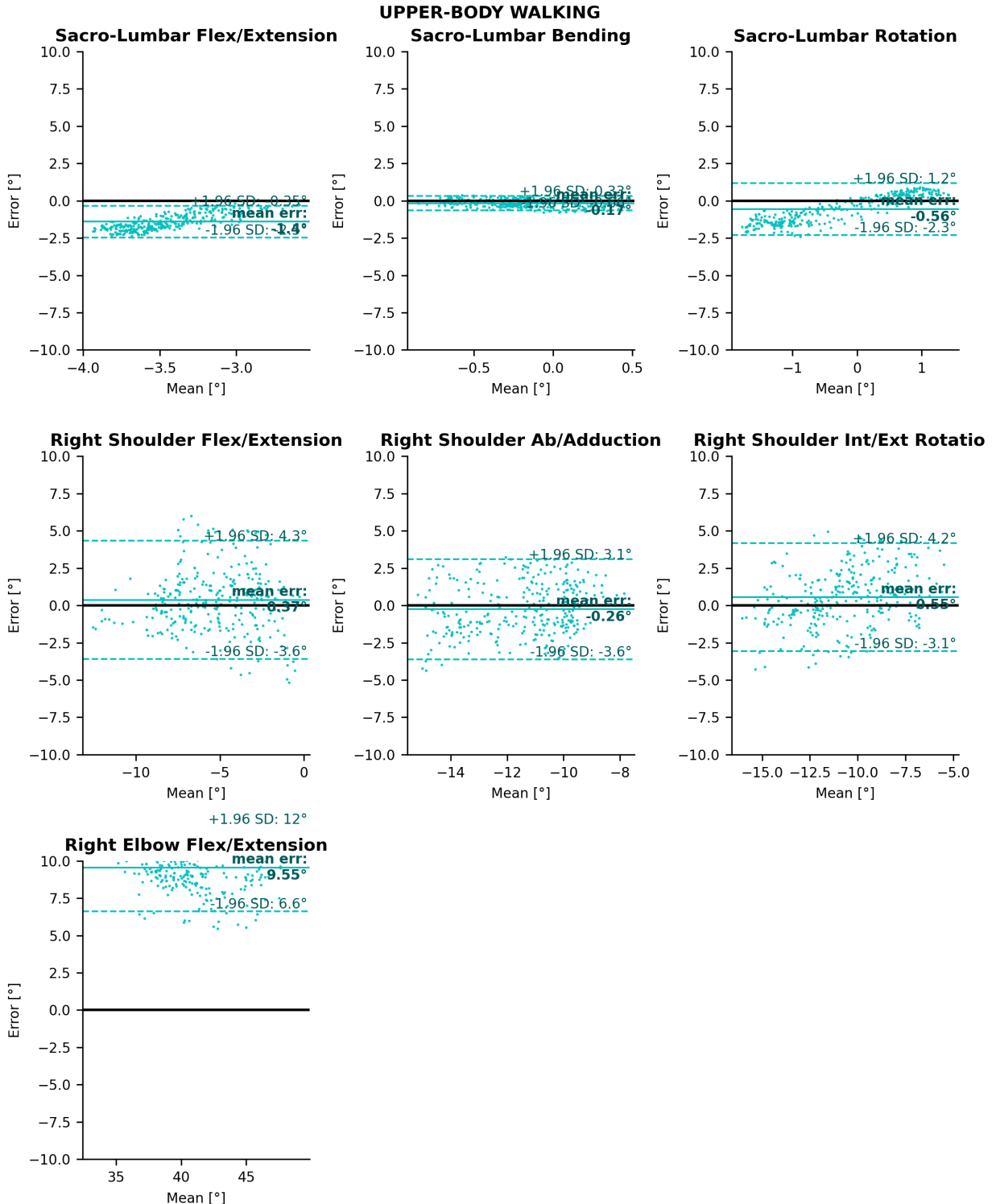


Figure B.6: Bland–Altman analysis of sacro-lumbar and upper-body joint angle errors for the walking task. Mean bias is represented as a horizontal solid, bold line, and 95% limits of agreement are represented as dotted lines.

B.2.2 Accuracy: Upper-body results for the running task

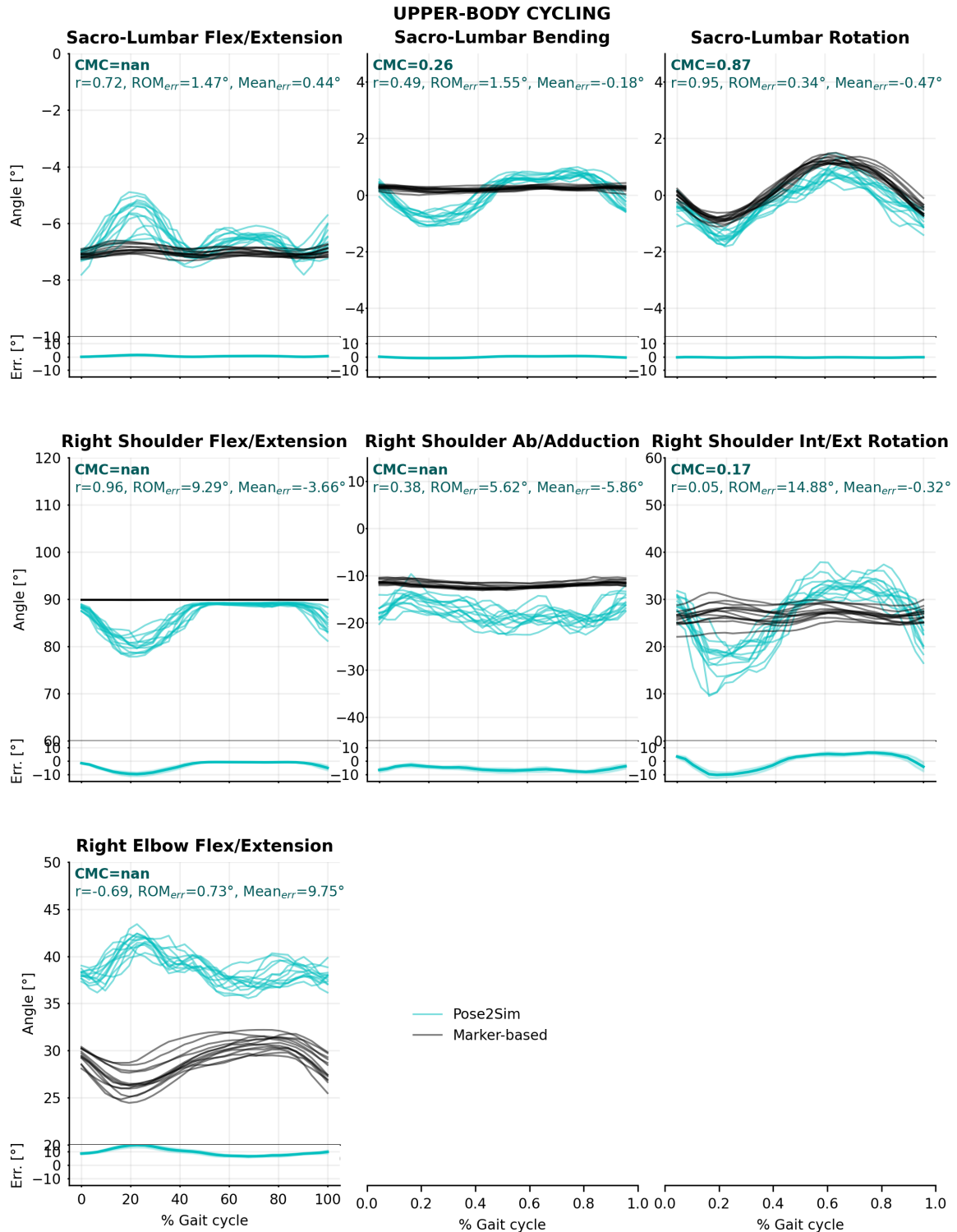


Figure B.7: Pose2Sim (cyan) and marker-based (black) sacro-lumbar and upper-body joint angles for the running task. Coefficient of multiple correlation (CMC) is indicated, and broken down into, respectively, Pearson's coefficient (r) for correlation assessment, range of motion errors (ROM_{err}) for gain, and overall mean error ($Mean_{err}$) for offset. Mean error and standard deviations are also represented at the bottom of the graphics.

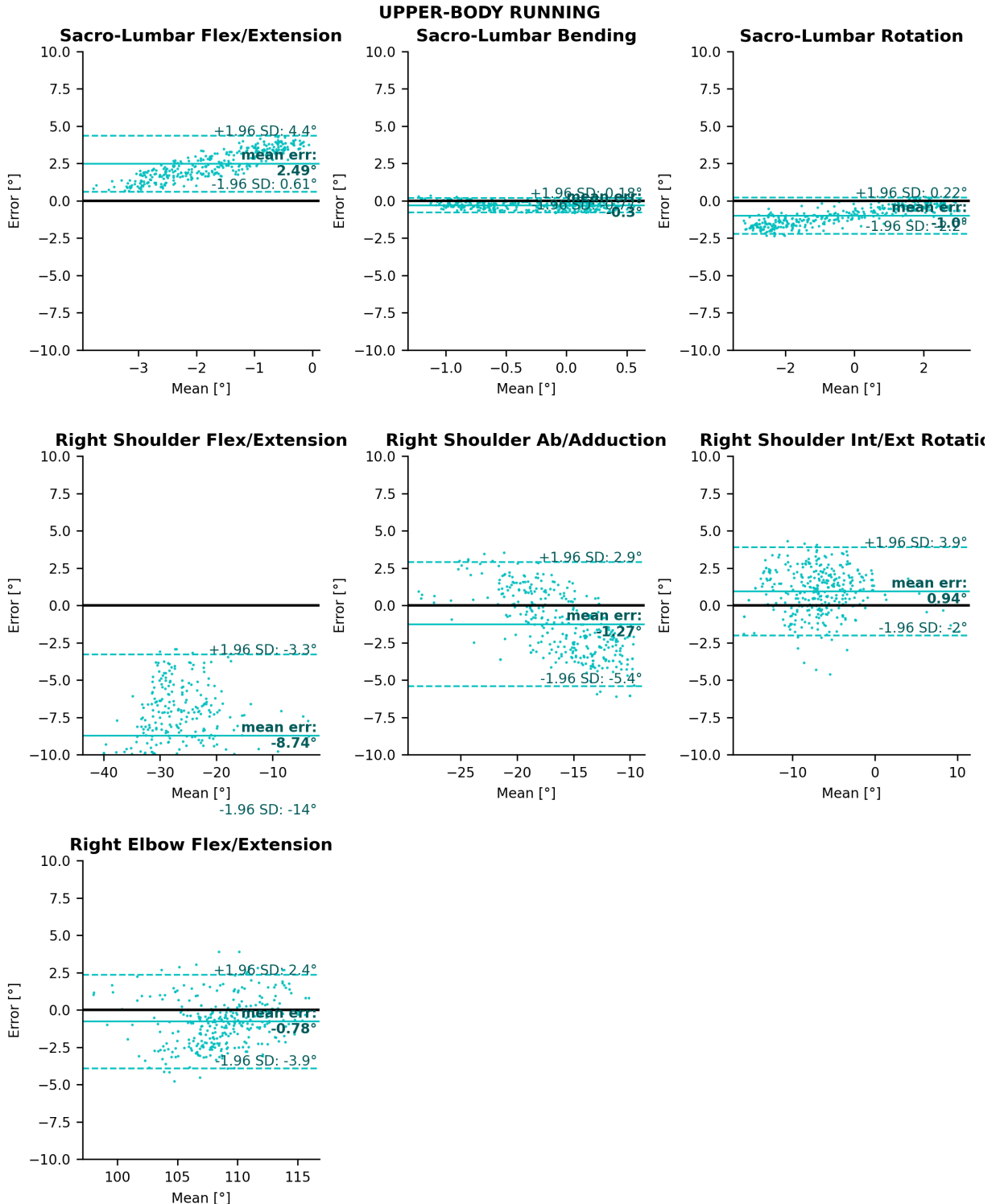


Figure B.8: Bland–Altman analysis of sacro-lumbar and upper-body joint angle errors for the running task. Mean bias is represented as a horizontal solid, bold line, and 95% limits of agreement are represented as dotted lines.

B.2.3 Accuracy: Upper-body results for the cycling task

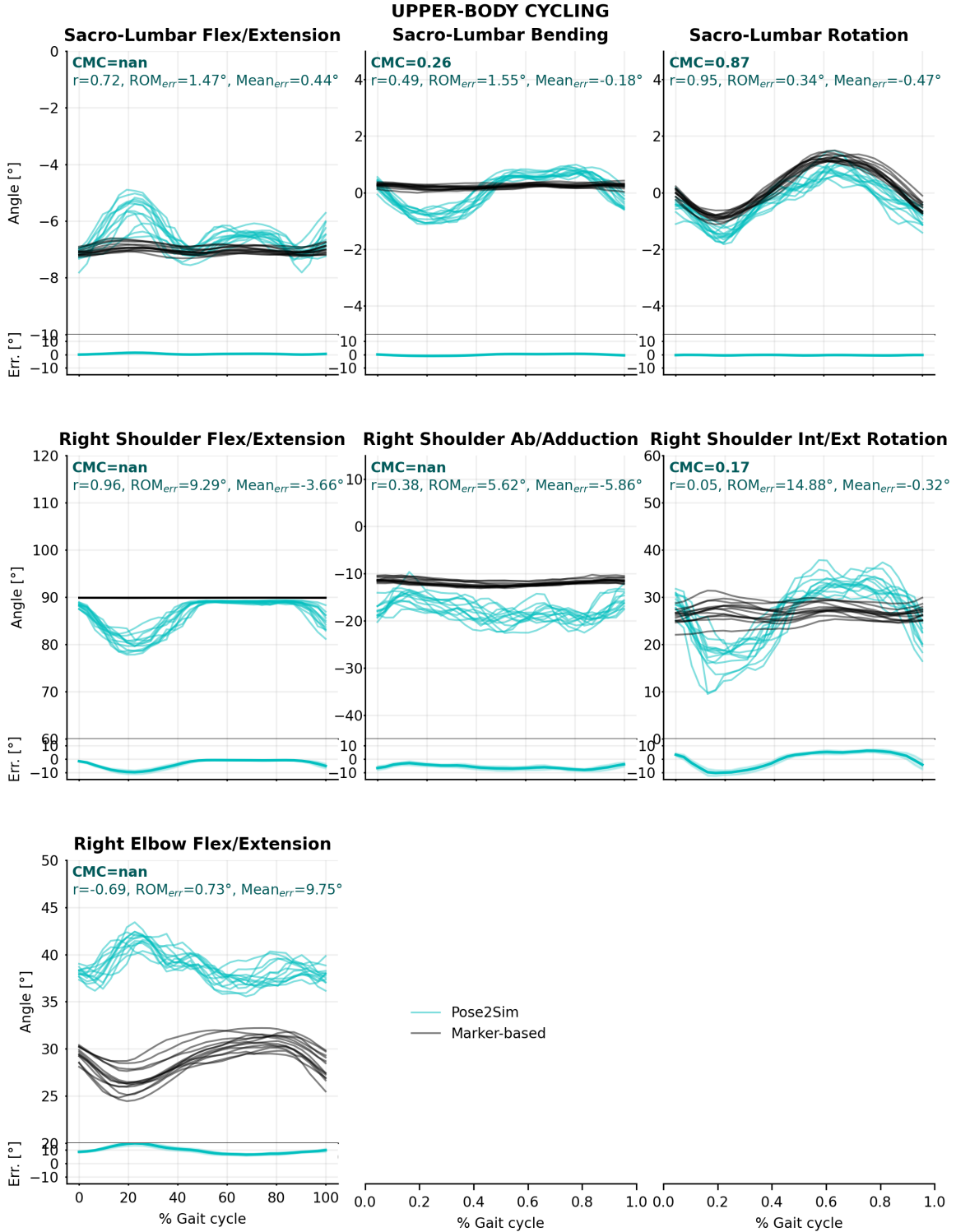


Figure B.9: Pose2Sim (cyan) and marker-based (black) sacro-lumbar and upper-body joint angles for the cycling task. Coefficient of multiple correlation (CMC) is indicated, and broken down into, respectively, Pearson's coefficient (r) for correlation assessment, range of motion errors (ROM_{err}) for gain, and overall mean errors ($Mean_{err}$) for offset. Mean error and standard deviations are also represented at the bottom of the graphics.

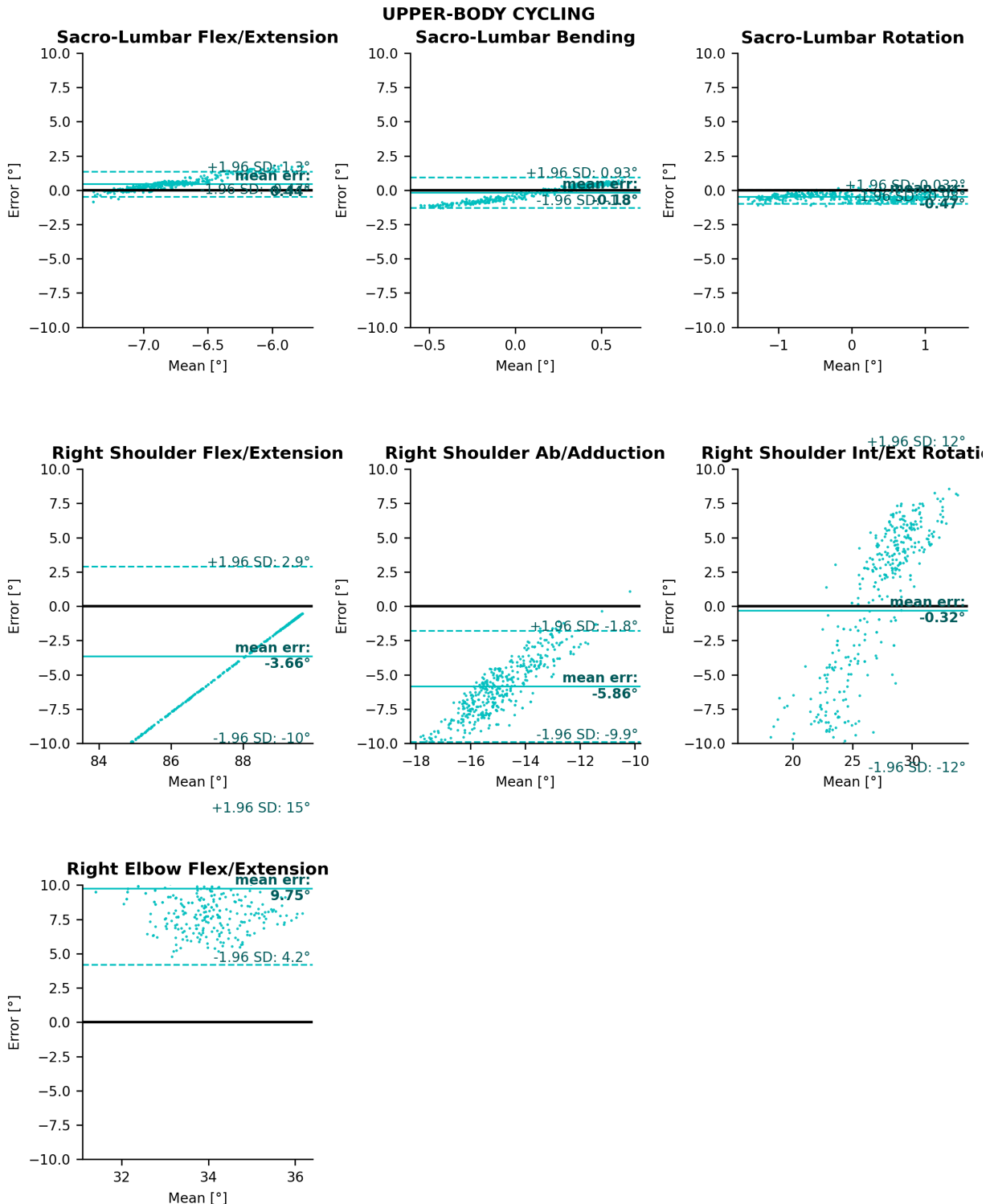


Figure B.10: Bland–Altman analysis of sacro-lumbar and upper-body joint angle errors for the cycling task. Mean bias is represented as a horizontal solid, bold line, and 95% limits of agreement are represented as dotted lines.

C

Appendix C : Protocole

Summary here on protocole.

Contents

C.1	Section 1	XLIII
C.1.1	Sous section 1	XLIII
C.1.2	Sous section 2	XLIII

Protocole

C.1 Section 1

C.1.1 Sous section 1

Hello, here is some text without a meaning. This text should show what a printed text will look like at this place. If you read this text, you will get no information. Really? Is there no information? Is there a difference between this text and some nonsense like “Huardest gefburn”? Kjift – not at all! A blind text like this gives you information about the selected font, how the letters are written and an impression of the look. This text should contain all letters of the alphabet and it should be written in of the original language. There is no need for special content, but the length of words should match the language.

C.1.2 Sous section 2

Hello, here is some text without a meaning. This text should show what a printed text will look like at this place. If you read this text, you will get no information. Really? Is there no information? Is there a difference between this text and some nonsense like “Huardest gefburn”? Kjift – not at all! A blind text like this gives you information about the selected font, how the letters are written and an impression of the look. This text should contain all letters of the alphabet and it should be written in of the original language. There is no need for special content, but the length of words should match the language.

"Design, evaluation, and application of a workflow for biomechanically consistent markerless kinematics in sports"

"Conception, évaluation, et application d'une méthode biomécaniquement cohérente de cinématique sans marqueurs en sport"

Résumé

Ici ... résumé en français.

Mots-clés : Mots clés

Abstract

Ici ... résumé en anglais.

Keywords : markerless motion capture; sports performance analysis; kinematics; computer vision; openpose; opensim; python package

